POLITECNICO DI TORINO

MASTER's Degree in AEROSPACE ENGINEERING

Experimental characterization of unsteady phenomena in over-expanded rocket nozzle

Supervisors

Prof. Emmanuele MARTELLI

Dr.ir. Ferdinand F.J. SCHRIJER

Dr. Woutijn J. BAARS

Candidate

Matteo GANCI

DECEMBER 2025

"As long as I don't give up on trying, I'll eventually be able to do it."

— Tanaka Ryuunosuke, *Haikyuu!!*

Sommario

Rocket nozzle performance is strongly influenced by shock-induced flow separation when operating in overexpanded conditions. This study presented an experimental and quantitative investigation of the unsteady flow phenomena developing in a thrust-optimized contour (Thrust Optimized Parabolic (TOP)) rocket nozzle. Building on previous research on the characterization of Free Shock Separation (FSS), Restricted Shock Separation (RSS), and the End-Effect Regime (EER), this work introduced and validated the use of Background Oriented Schlieren (BOS) as a quantitative flow visualization tool for high-speed nozzle flows, in combination with Proper Orthogonal Decomposition (POD), a data-driven modal decomposition technique.

A dedicated experimental campaign was conducted at the ASCENT cold-flow facility of Delft University of Technology. Following an initial assessment of the BOS reconstruction accuracy and spatial resolution, the method was applied to characterize the flow topology across a range of Nozzle Pressure Ratios (NPR). The simultaneous reconstruction of horizontal (dx) and vertical (dy) displacement fields allowed to resolve the main flow structures known from literature, such as the alternating compression/expansion regions within the jet core and the upper and lower shear layers that define the jet boundaries.

The time-resolved sequences were further analyzed using Proper Orthogonal Decomposition (POD), which extracted distinct spatial modes representing the most energetic coherent structures of the flow. The analysis confirmed that the main unsteadiness can be accurately described through a low-rank approximation. The frequency spectra of the temporal coefficients revealed a dominant peak at approximately 480 Hz and its harmonics, a signature shared across both FSS and RSS regimes, suggesting the presence of a common underlying instability mechanism.

The combined use of quantitative BOS and modal decomposition provided new physical insight into the dynamics of shock–separation interaction in overexpanded nozzles. This work demonstrates the potential of BOS as a reliable, flexible, and cost-effective alternative to conventional Schlieren systems, while offering a robust framework for the modal and spectral analysis of high-speed nozzle flows. The results contribute to a deeper understanding of the mechanisms driving flow separation and unsteadiness in thrust-optimized nozzles, supporting the development of more stable and efficient propulsion systems.

Ringraziamenti

Desidero innanzitutto ringraziare il Prof. E. Martelli, che ha reso possibile questo percorso e mi ha spinto a superare i miei confini. Grazie per la fiducia e per aver trasmesso la passione e la curiosità che hanno accompagnato ogni fase di questo cammino.

Un ringraziamento va anche ai professori che mi hanno accolto all'estero: Dr. ir. F.F.J. Schrijer e Dr. ir. W.J. Baars. La loro disponibilità, pazienza e fiducia nel mio lavoro hanno reso quest'esperienza ancora più significativa.

Un grazie profondo va ai miei genitori. Se sono *dove* sono, lo devo anche a loro. So di non essere sempre stato presente, ma ci tengo a ricordare che nel bene e nel mane, nei momenti felici come in quelli più complessi, la loro presenza è stata fondamentale e a loro devo semplicemente tutto. Vi voglio bene.

A Samuele, mio fratello. È difficile trovare le parole giuste per descriverlo perché lui è tante cose insieme: un punto di riferimento, un amico, un compagno di giochi e di avventure, una spalla su cui piangere e a cui raccontare tutto; in poche parole una presenza costante nella mia vita. Se sono *come* sono è anche merito suo. Credo che nella vita ci sia un momento inaspettato in cui il legame tra fratelli cambia. Un giorno ti accorgi che quella persona che è sempre stata lì è diventata qualcosa di insostituibile. Non credo che da quel momento sia passato un solo giorno senza che ci fossimo sentiti, anche solo con un messaggio. Ci chiamiamo, giochiamo, ci raccontiamo le giornate, condividiamo piccole cose che, messe insieme, sono tutto. La mia vita sarebbe indubbiamente più vuota senza di lui. E so che in fondo, per quanto io provi a scriverlo, nessuna parola riuscirà davvero a spiegare quanto lui significhi per me.

A Simone, il mio migliore amico. Sei stato la prima persona che ho incontrato il primo giorno di scuola. Ricordo benissimo quel giorno di settembre, quando timidamente ci siamo fatti avanti — entrambi in largo anticipo rispetto a tutti gli altri — e devo davvero ringraziare chiunque ci abbia messo lo zampino, perché è proprio grazie a quel momento che oggi mi trovo a scrivere queste parole. Abbiamo scoperto di appartenere alla stessa classe e, da allora, è nata un'amicizia che non avrei mai immaginato potesse diventare così importante. Da quel giorno abbiamo condiviso tutto, crescendo insieme e diventando, a tutti gli effetti, ciò che si definisce "migliori amici" — anche se il nostro rapporto va ben oltre un'etichetta. Siamo diversi sotto molti aspetti, e ogni volta che parliamo di politica rischiamo di litigare, ma forse è proprio questo il segreto. Siamo complementari; in un certo senso, uno il polmone dell'altro: ci bilanciamo e ci teniamo in vita a modo nostro. La mia vita non sarebbe la stessa senza di te, perché perderti sarebbe davvero come perdere una parte di me. Ti voglio bene, e grazie per avermi sopportato e supportato lungo tutto il mio percorso — nonostante la distanza e il vivere lontano. E quando andremo in pensione, ti prometto che la compriamo davvero quella villetta, così finalmente potremo tornare a vivere più vicini che si può.

Vorrei ringraziare Enrico e Davide, che da compagni delle superiori sono diventati i miei coinquilini a Torino. Mi hanno accompagnato lungo tutto il percorso universitario, dalla triennale alla magistrale, condividendo con me momenti di studio, leggerezza e confronto.

Enrico, grazie per essermi sempre stato vicino. Quel giorno in cui, quasi per caso, ci siamo seduti sullo stesso banco, non potevo immaginare quanto avrebbe inciso nella mia vita. Da allora abbiamo sempre camminato insieme, sostenendoci a vicenda tra risate, discussioni e piccoli drammi quotidiani — dalle bestemmie contro la Colamasi e la Micciché fino ai problemi al di fuori della scuola. Dalle superiori fino all'università, dove il nostro rapporto si è consolidato ancora di più. Entravamo l'uno nella stanza dell'altro, con naturalezza, per parlare di tutto: dai problemi più seri alle stupidaggini più assurde. Ci siamo fatti compagnia, ci siamo sopportati, ci siamo spronati. Siamo stati, a turno, conforto e realtà cruda, capaci di dirci le cose come stavano, ma sempre con sincerità e affetto. Con te ho un legame profondo: ci somigliamo in molti modi, e anche quando ci siamo scontrati, non ci siamo mai davvero persi. Sei uno degli amici più cari che ho.

Davide, con te il rapporto è sempre stato un equilibrio tra sintonia e differenze. Se devo essere sincero, quasi un legame di amore e odio — nel senso più umano del termine: perché ti rispetto, ti ammiro e, a volte, mi sono sentito in difficoltà di fronte a quanto sembri sempre un passo avanti. Non è un segreto che ti abbia sempre considerato una guida, ma negli ultimi tempi ho avuto la sensazione che le nostre strade si stessero un po' allontanando — colpa anche mia, e di come stavo affogando nei miei stessi pensieri. Ti ho sempre messo su un piedistallo, e questo, pur senza volerlo, mi ha portato spesso a paragonarmi a te, fino a dubitare di me stesso. Ci tengo però a dirti che il nostro legame per me resta importante, e che non voglio perderlo. Sei stato una fonte di ispirazione continua, un punto di riferimento costante sia nello studio che nella vita di tutti i giorni: tra palestra, alimentazione e modo di affrontare le cose con determinazione. Ho una grande stima di te, e ti ringrazio per avermi fatto da mentore e da spalla. Spero che, anche se la vita ci porterà su percorsi diversi, continueremo a trovarci — come è successo adesso, condividendo per una seconda volta questo momento così importante.

Un ringraziamento speciale va anche a Pietro, il mio coinquilino in Olanda. Con te mi sono trovato sorprendentemente bene: in poco tempo ci siamo resi conto di quanto simili eravamo e di come avessimo le stesse passioni. Il destino ha voluto farci trovare e credo che, in qualche modo, abbiamo imparato tutti e due qualcosa l'uno dall'altro, anche se, da saccente come sei, non lo ammetterai mai. Ti ringrazio per tutte le serate passate a giocare insieme, a ridere, a parlare di tutto e di niente: sono stati momenti semplici, ma meravogliosi. E anche se sei abituato a sentirti dire il contrario, oggi ti voglio dire che è Roberta quella fortunata ad averti.
E perché no, grazie anche a Tommaso che ha permesso la nascita di questa amicizia.

Vorrei ringraziare Francesco e Alberto, due amici di infanzia che vivono accanto a me da quando avevo sei anni.
Ciccio, grazie perché nonostante il gap di età, mi hai sempre fatto da fratello maggiore, introducendomi a giochi e attività che oggi mi sono ancora così cari. Anche con la distanza e con la vita che va avanti, ogni volta ci ritroviamo: una sera, quell'oretta, ogni tanto, a giocare insieme. Quei momenti sono stati per me una valvola di sfogo preziosa.
Alberto, con te è stato speciale in modo diverso: siamo coetanei, eppure sei stato come un secondo fratello per me. Siamo cresciuti quasi in simbiosi, sostenendoci a vicenda, condividendo gioie, disprezzi e piccole difficoltà. Ti ringrazio perché sei sempre stato accanto a me, senza mai far pesare i miei difetti, e senza mai smettere di credere in me. Anche nei momenti in cui tendevo a scomparire o a isolarmi, tu eri sempre lì, pronto ad accogliermi e a capirmi. Sono stato davvero fortunato ad averti nella mia vita, e spero che questa vicinanza non venga mai meno.

A miei amici della palestra. Abituarsi ad un allenamento senza la vostra compagnia non è stato facile. Grazie per aver mantenuto la mia motivazione alta, dentro e fuori la sala pesi. Tra di loro una parentesi speciale va fatta a Gabriele. È difficile spiegare il come o il perché, ma la verità è che ci siamo trovati subito: in pochissimo tempo abbiamo scoperto di essere incredibilmente affini, simili nei pensieri e nel modo di vivere le cose. Con lui è nato un legame profondo, di quelli che non hanno bisogno di tempo per crescere. Mi sono aperto con lui come raramente mi capita: gli ho raccontato cose che di solito tengo per me, e non mi sono mai sentito giudicato ma anzi, visto e ascoltato. Mi dispiace che, proprio quando la nostra amicizia stava diventando ancora più forte, io sia dovuto partire per l'Olanda. Anche se la distanza ha reso più difficile sentirci con la stessa frequenza, so che il legame resta, e spero davvero che la vita ci riporti prima o poi sullo stesso cammino.

A Michela. Ci siamo conosciuti da poco e il nostro rapporto non è stato sempre semplice, eppure sei riuscita a essere per me bussola e compasso morale. Hai saputo credere in me quando io stesso avevo dubbi, mi sei stata vicino, più profondamente di chiunque altro, riuscendo a farmi da sostegno e a farmi trovare la giusta direzione nei momenti più complessi. Hai reso questa esperienza in Olanda ancora più speciale. Una parte del mio cuore sarà per sempre tua anche se non ci si dovesse sentire più.

A Gaia. È buffo pensare che tutto sia iniziato in modo quasi ingenuo, ai tempi delle superiori, quando sei stata la mia prima cotta. Col tempo, quella infatuazione si è trasformata in una delle amicizie più sincere e importanti che io abbia. Hai sempre avuto la capacità di capire le persone, e una sola conversazione con te mi ha fatto sentire compreso e ascoltato più di mille discorsi con chiunque altro. Ti ringrazio perché ti sei sempre mostrata disponibile, trovando il modo di vederci anche quando non era semplice. Credo fermamente che sia grazie anche a te se sono riuscito ad arrivare fin qui. E, soprattutto, grazie a questa tesi siamo finalmente riusciti a vederci più di due volte l'anno, traguardo più unico che raro.

A Monica, che conoscevo già dall'università ma che ho ritrovato qui per caso. Ti ringrazio per avermi accolto e introdotto al gruppo, rendendo questa esperienza molto più ricca e piacevole di quanto immaginassi.
Ad Alessandro, che ho avuto il piacere di conoscere bene negli ultimi mesi. Grazie perché apprezzo molto il tempo che mi hai dedicato e tutti i consigli che mi hai dato. Nonostante tutto penso davvero che tu sia un signore e un grande amico.
A Michele, per il supporto durante tutti gli esami dati insieme lungo la magistrale.
A Martino, per tutte le risate fatte parlando di musica e vedendo i video di QDSS.
A Vittorio, per i bei discorsi sulla politica e sulla vita, e ai i consigli preziosi nel come usare il cluster della facoltà.
E a tutti i tesisti, dottorandi e amici che ho incontrato durante questi otto mesi in Olanda e durante i tre anni della magistrale.

In conclusione, questa sezione non vuole solo essere un elenco di nomi, ma anche un piccolo spazio di riflessione. C'è un testo di una canzone che ha risonato con me, e come mi sono sentito in questo percorso, più di qualunque altro discorso. Ci tengo a includerlo in questi ringraziamenti, come promemoria di ciò ho provato. Mia mamma lo chiamerebbe "chi la sa la canti", ma per me Ernia scrivendo Per te ha creato molto più di una canzone. Ha creato un piccolo specchio nel quale sono riuscito a vedere come mi sono rapportato con me stesso. È un promemoria di quanto sia difficile accettarsi, perdonarsi, e continuare a camminare anche quando si ha la sensazione di essere rimasti indietro. L'ho scelta perché, in un certo senso, questa tesi è anche un modo per dirlo a me stesso:

"Tu dammi la mano, siamo diventati grandi
Ci siamo odiati tanto, ma siamo ancora io e te
Non ti sei mai premiato un giorno per i tuoi traguardi
E forse ne avresti bisogno, lo sai, più di me
Passan le ore e poi riguardavo noi
Questa fiamma sai che brucerà
Ancora che ti annoi, compra quel che vuoi
Tanto poi, lo sai, non basterà [...]
Te lo rimproveri, ma non sei mai stato davvero un egoista
Nemmeno una volta
Ma senti qualcosa che si muove dentro, chiama un esorcista
Se hai l'anima sorda, ahi
Mi hai promesso di cambiare, ma tu non rispetti i patti
Vedi buio pesto, non vedi il progresso
Ti fasci la testa prima che la sbatti, ti odio anche per questo
Sono già trent'anni, non sai rassegnarti
La malinconia non passerà
È tanto che ti affanni, non riesci ad amarti
Goccia dopo goccia scalfirà
Tu ti senti solo
E a volte un po' lo sei
Ma quando prendi il volo
Diventi come vorrei [...]
Non darmi la mano allora se non vuoi pensarci
Ma vorrei che almeno una volta partisse da te
Giochiamo per la stessa squadra, sai, conviene a entrambi
So che prima o poi riuscirò a farti fidar di me
Che ci sia o pioggia o neve
Che tu lo voglia o no

E in fondo, lo sai
Se mi cercherai, ti starò di fianco
Da me ti distrai, non ti fidi mai
Non parliamo tanto
Na-na-na-na-na, na-na-na-na-na
Fallo per te
Na-na-na-na-na, na-na-na-na-na
Fallo per te”

— Ernia, *Per te*

Indice

Elenco delle figure

Elenco delle tabelle

Acronyms

BOS	Background Oriented Schlieren.
CC	Cross-Correlation.
CoC	Circle of Confusion.
DMD	Dynamic Mode Decomposition.
EER	End-Effect Regime.
FFT	Fast Fourier Transform.
FOV	Field Of View.
FSS	Free Shock Separation.
HRBOS	High Resolution Background Oriented Schlieren.
IW	Interrogation Window.
MOC	Method Of Characteristics.
MOR	Model Order Reduction.
NPR	Nozzle Pressure Ratios.
PIV	Particle Image Velocimetry.
POD	Proper Orthogonal Decomposition.
PSD	Power Spectral Density.
ROI	Region of Interest.
ROM	Reduced-Order Model.
RSS	Restricted Shock Separation.

SNR	Signal-to-Noise Rateo.
SPOD	Spectral Proper Orthogonal Decomposition.
SVD	Singular Value Decomposition.
SWBLI	Shock Wave - Boundary Layer Interaction.
TIC	Truncated Ideal Contour.
TOC	Thrust Optimized Contour.
TOP	Thrust Optimized Parabolic.

Capitolo 1

Introduction

Launch vehicles represent one of the most complex engineering achievements in human history. In order to overcome Earth's gravitational pull and atmospheric drag, and thereby transport payloads into orbit, these vehicles rely on powerful propulsion systems capable of generating extremely high thrust levels. This thrust is primarily produced by chemical rocket propulsion systems. These systems remain the foundation of space access due to their high energy density and controllable thrust characteristics. In such engines, the chemical energy of stored high-pressure propellants is converted through combustion into thermal energy. The resulting high-enthalpy gases are then expanded through an exhaust nozzle, which converts thermal and pressure energy into kinetic energy. The nozzle is therefore a key component governing the overall efficiency of the propulsion system.

The performance of a rocket nozzle depends strongly on both its geometry and the pressure ratio between the combustion chamber and the surrounding environment. Ideally, the expansion process within the nozzle should be such that the static pressure of the exhaust flow at the exit plane equals the ambient pressure, thereby achieving perfect expansion and maximizing the thrust coefficient. However, this condition can only occur at a specific altitude, since the ambient pressure decreases continuously as the vehicle ascends. As a consequence, any fixed-geometry nozzle must operate under non-ideal expansion for most of the trajectory: it is under-expanded at high altitudes and over-expanded near sea level. In the later regime, the exit pressure of the flow becomes lower than the ambient pressure, producing an adverse pressure gradient that can lead to internal shock formation and subsequent flow separation along the nozzle wall. This separation alters the effective thrust vector and can induce strong unsteady forces on the structure. The problem becomes particularly pronounced in modern high-area-ratio nozzles, such as Thrust Optimized Parabolic (TOP) nozzles.

Flow separation can occur in different configurations, such as Free Shock Separation

(FSS) and Restricted Shock Separation (RSS) [1] [2] [3]. These regimes are characterized by strong pressure oscillations and asymmetric separation patterns that may generate intense side loads and low-frequency structural vibrations [4] [5] [6]. Such unsteady lateral forces can compromise engine integrity. Historical evidence of these phenomena has been reported in several propulsion systems. The J-2S engine, developed during the Apollo program, experienced violent side loads that led to the detachment of the nozzle extension from its gimbal mount. The Space Shuttle Main Engine (SSME) suffered from similar issues, where severe flow separation and asymmetric shocks caused fatigue cracks and coolant-line ruptures in the nozzle wall during ground tests. Likewise, the Vulcain engine on the Ariane launch vehicle and Japan's LE-7A engine exhibited comparable side-load-induced structural stresses. These recurring phenomena across different programs underline that shock-induced flow separation remains one of the most critical design challenges in rocket propulsion. Understanding and predicting the unsteady flow behavior inside over-expanded nozzles is therefore essential to ensure structural safety, optimize performance, and reduce the need for costly full-scale testing.

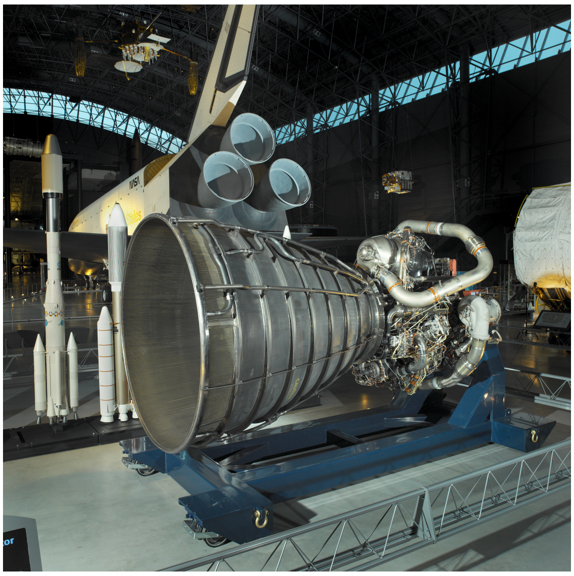

Figura 1.1: Space Shuttle Main Engine (SSME) (Credit: Smithsonian National Air and Space Museum, Accession No. A20040205000).

In recent years, extensive experimental and numerical studies have explored the dynamics of over-expanded supersonic nozzles and underexpanded jets. These studies revealed that Shock Wave - Boundary Layer Interaction (SWBLI) interactions and shock oscillations dominate the transient flow behavior downstream of the nozzle exit [1] [7]. Modern research efforts increasingly rely on data-driven analysis techniques, such as Proper Orthogonal Decomposition (POD) and Spectral Proper Orthogonal Decomposition (SPOD), to extract coherent structures and quantify dominant instability mechanisms from high-resolution flow data [8] [9] [10]. These modal analysis tools enable reduced-order representations of complex unsteady phenomena, providing insight into the spatial and spectral organization of the flow.

Nevertheless, several challenges remain. First, experimental visualization techniques capable of capturing transient flow structures, especially under varying Nozzle Pressure Ratios (NPR), often face limitations in spatial or temporal resolution. Second, due to the limited optical accessibility of the internal nozzle region, most diagnostics can only observe the external jet, providing an indirect representation of the internal shock and separation dynamics. This indirect observation introduces an inherent level of uncertainty, as the measured exhaust flow structures are the downstream manifestation of complex internal interactions. Third, establishing a clear correlation between these unsteady flow features and the resulting aerodynamic loads acting on the nozzle structure remains an open issue.

In view of the above, Background Oriented Schlieren (BOS) was chosen as the experimental approach to study such flows. BOS is a non-intrusive optical technique that measure density gradients by tracking apparent displacements of a background pattern. While it has been successfully applied to compressible and shock-dominated environments, its application to rocket nozzle exhausts plume is particularly novel [11] [12].

This report is organized into seven chapters, including the present one. Following the introduction, Chapter 2 presents a comprehensive review of relevant literature, establishing the current state of knowledge. Chapters 3 and 4 provide comprehensive descriptions of the experimental methodology and setup. The data processing technique is thoroughly discussed in Chapter 5 while in Chapters 6 and 7 the key results and final conclusions are, respectively, presented.

Research Objective and Questions

In this context, the present work contributes to the ongoing effort of characterizing and understanding of flow unsteadiness inside rocket nozzle. The study focuses on two main aspects:

1. **Technique validation** – The performance of the Background Oriented Schlieren (BOS) method is assessed in the context of supersonic nozzle flow visualization. The method's capability to reconstruct displacement fields and density gradients is evaluated based on known flow features and comparison with other well-known techniques, with particular attention to its sensitivity, accuracy, and limitations in capturing shock dynamics.
2. **Modal analysis** – Using the validated BOS data, the study investigates the dominant instability structures associated with FSS and RSS regimes through data-driven

techniques. The analysis aims to identify the spectral content, spatial topology, and temporal evolution of coherent flow structures.

The objective of the research is defined as follows:

"*The objective of this research is to experimentally investigate the unsteady flow separation phenomena occurring in an over-expanded Thrust Optimized Parabolic nozzle. Through high-speed Background Oriented Schlieren imaging and data-driven analysis techniques, this study aims to deepen the understanding of nozzle flow unsteadiness, identifying coherent structures and dominant flow instabilities across Free Shock Separation and Restricted Shock Separation regimes*"

The research is driven by the following main questions:

- **RQ1**: How well is Background Oriented Schlieren (BOS) able to capture the relevant flow features of the nozzle?
    - What are the main strengths and limitations of BOS?
    - To what extent do the reconstructed displacement fields (dx, dy) and density maps describe the nozzle flow topology?
    - How does the simultaneous acquisition of dx and dy allow detecting wave orientation and flow structures?
- **RQ2**: What are the dominant instability structures and mechanisms associated with FSS and RSS configurations?
    - What spectral features distinguish FSS and RSS regimes?
    - Is it possible to describe the main unsteadiness with reduced-order reconstructions (low-rank approximation)?
    - To what extent can modal decomposition techniques connect the spectral content of the flow to its spatial topology?

Capitolo 2

Literature Review

This chapter presents a comprehensive literature overview on nozzle flow dynamics, covering the fundamental principles of nozzle operation, boundary layer development, flow separation, and Shock Wave - Boundary Layer Interaction. The focus is on the mechanisms leading to unsteady separation in overexpanded nozzles, which are key to the experimental investigation.

2.1 Nozzle fundamentals

Building upon the general principles introduced in the previous chapter, the attention is now focused on the nozzle [13]. Key component of rocket propulsion systems, a **rocket nozzle** is a conduit with a variable cross-sectional area, specifically used to control fluid flow. The main function of a nozzle is to transform the potential energy available in the combustion chamber as high pressure and temperature into kinetic energy at the nozzle exit in order to provide thrust. Supersonic nozzles, also known as De Laval nozzles, consist of a converging section, a throat section, and a diverging section. First, the area decreases until the minimum, also called the throat area, is reached. Here, the gas velocity corresponds to a Mach number of one. Then the nozzle supersonically accelerates the flow in a region where the area increases.

2.1.1 Ideal nozzle

An ideal nozzle is defined as one that achieves maximum thrust by having the exhaust pressure at the nozzle exit perfectly matched with the ambient pressure. In this configuration, the flow expands isentropically from the throat, resulting in a uniform, parallel exit stream at a specific Mach number. This type of nozzle is designed with the **Method Of Characteristics (MOC)**. In such nozzles, any off-design operation induces performance losses.

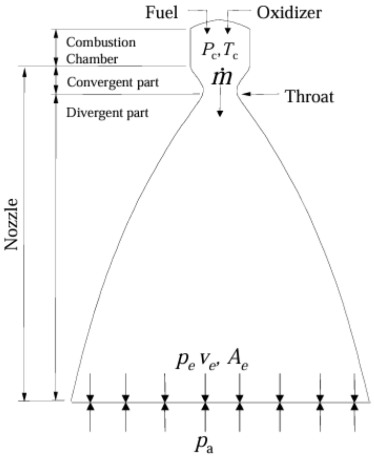

Figura 2.1: Rocket thrust chamber (Taken from [4][Fig. 1])

2.1.2 Nozzle contour design

Different types of conventional convergent-divergent rocket nozzles exist. Currently, mainly two types of nozzle contouring methods are applied in space propulsion: The **Truncated Ideal Contour (TIC) nozzle** and the **Thrust Optimized Parabolic (TOP) nozzle**.

Truncated Ideal Contour

In inviscid flow conditions, it is possible to design so-called ideal contour nozzles that achieve a uniform exit flow profile, characterized by constant pressure, temperature, and velocity across the entire exit plane. The ideal nozzle is extremely long and consequently is not practically feasible for rocket applications. However, the thrust contribution of the last part of the contour is negligible due to the small wall slopes. A practical solution is to truncate the ideal contour, resulting in what is referred to as a TIC nozzle. The only free design parameter is the design Mach number. The higher the design Mach number, the higher is the maximum divergence angle and the larger is the nozzle. An ideal contour produces a shock-free flow.

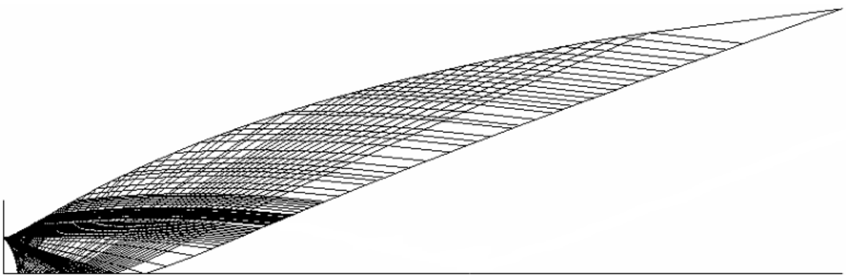

Figura 2.2: Example of left and right running characteristic lines in a TIC nozzle (Taken from [4][Fig. 10])

Thrust Optimized Parabola

In 1957 Rao in America and Shmyglevsky in Russia found a way to produce an optimum nozzle that would cause the least thrust losses. This nozzle is known as the Thrust Optimized Contour (TOC) nozzle. Since the design of the Rao-Shmyglevsky nozzle is rather complicated, Rao proposed a parabolic-geometry approximation [14]: He noticed that the bell portion of his nozzles could be closely approximated by a skewed parabola, leading to a rapid sketch of the nozzle shape with minimal loss in thrust performance. These types of nozzles are referred as Thrust Optimized Parabolic (TOP) nozzles. In contrast to the shock-free flow through a TIC, a TOP produces an internal shock originating from the throat region. This characteristic has been shown to be useful for sea level conditions where a margin against flow separation is important.

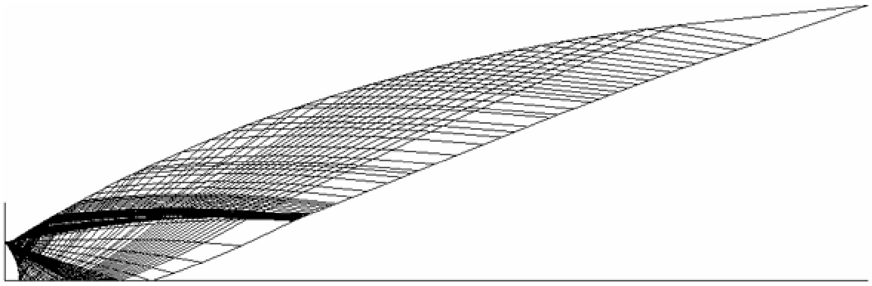

Figura 2.3: Example of left and right running characteristic lines in a TOP nozzle (Taken from [4][Fig. 12])

2.1.3 Exhaust plume pattern

High-performance rocket engine nozzles, typically used for first or main stage propulsion, must operate across a wide range of ambient pressures, from sea-level conditions up to near-vacuum during ascent. As a consequence, the internal flow can experience different expansion regimes throughout the flight. When the pressure at the nozzle exit is lower than the ambient pressure, the flow is said to be in an **overexpanded** condition. In this regime, shock waves are required to adjust the exit pressure to match the external environment. Overexpansion typically occurs when the rocket is on the launch pad or during the initial stages of flight, where the high ambient pressure forces the exhaust flow to compress internally. If the pressure difference becomes too large, the internal shock system may interact with the wall boundary layer, potentially causing **flow separation** and inducing strong lateral loads on the nozzle structure [4]. As the vehicle ascends and the ambient pressure decreases, the initially overexpanded flow gradually transitions toward a state of pressure adaptation, eventually becoming **underexpanded** at higher altitudes. In the overexpanded regime, the exhaust adjusts to the surrounding pressure through a complex

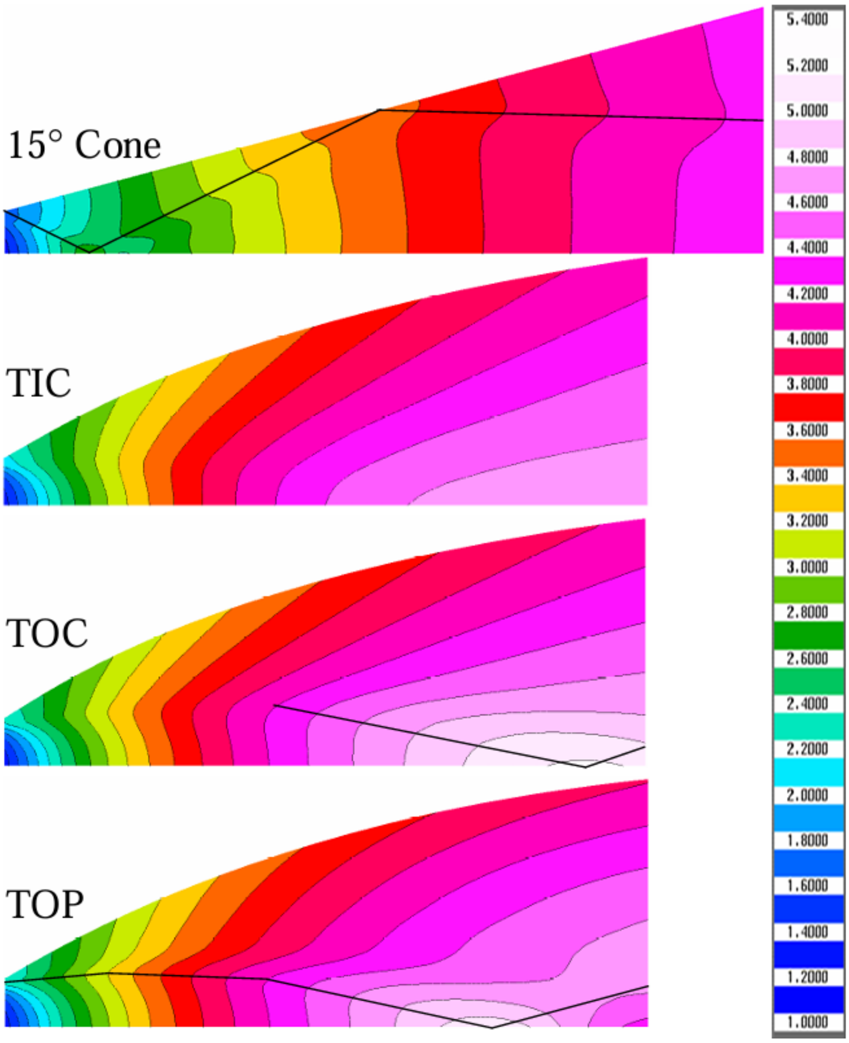

Figura 2.4: Example of mach number distribution in a 15° conical, TIC, TOC and TOP nozzle (Taken from [4][Fig. 3])

system of oblique shocks and expansion fans, producing the characteristic **barrel-shaped plume** often observed in launch footage. Various shock patterns have been reported in the plumes of overexpanded rocket nozzles. In a TIC nozzle, the transition from a Mach disc to an apparent regular shock reflection occurs as the degree of overexpansion decreases [15]. In contrast, nozzles featuring an internal shock structure, such as TOC and TOP configurations, typically exhibit a **cap-shock pattern** [16]. As the combustion chamber pressure increases, the flow becomes progressively less overexpanded, and the internal shock eventually intersects the nozzle centerline, forming a Mach disc pattern.

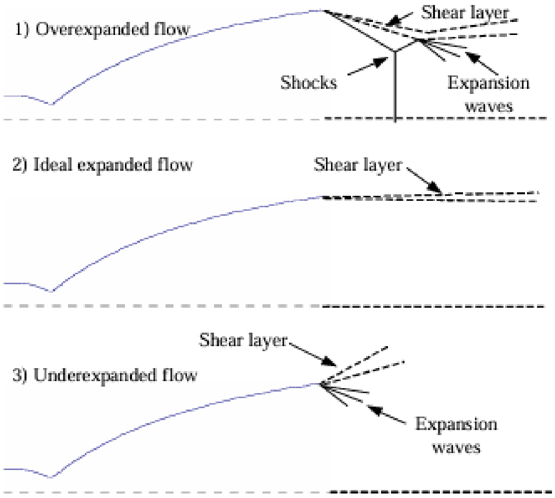

Figura 2.5: Overexpanded, Ideal, Underexpanded flow conditions (Taken from [4][Fig. 2])

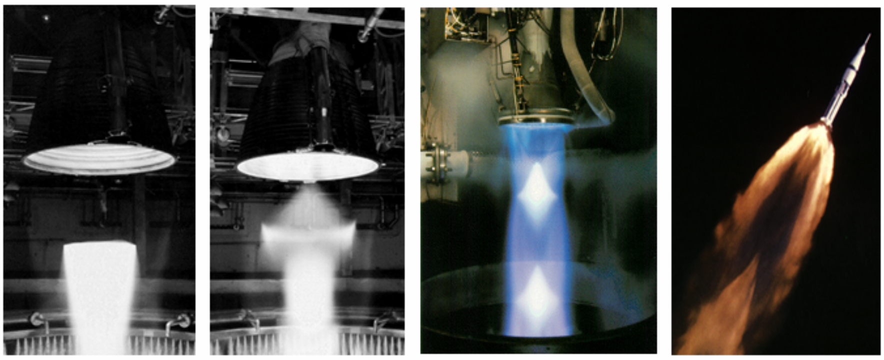

Figura 2.6: Exhaust plume pattern: (a) Vulcain, overexpanded flow with Mach disk, (b) Vulcain, overexpanded flow with cap-shock pattern, (c) RL10-A5, overexpanded flow with apparent regular reflection, (d) underexpanded flow, photographed during launch of Saturn 1-B (Credit: SNECMA, CNES, NASA).

2.2 Fundamentals of flow separation

2.2.1 Boundary layer

[17] In 1904, German fluid dynamicist Ludwig Prandtl showed that flows with low friction in the vicinity of bodies can be subdivided into two regions: a thin layer close to the body, the so-called boundary layer, and the remaining flow. For the vast region of the flow field away from the body, the velocity gradients are relatively small, and friction plays virtually no role. For the thin region of the flow adjacent to the surface, however, the velocity gradients are large, and friction plays a defining role. Within the boundary layer, the fluid particles near the surface experience viscous forces, which cause the velocity to decrease toward the wall, ultimately reaching zero at the surface due to a phenomenon known as the no-slip condition: the infinitesimally thin layer of air molecules in immediate contact

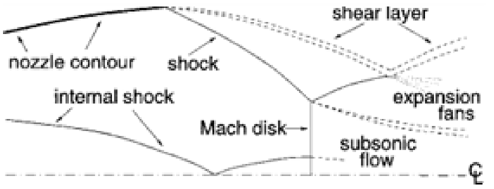

a) Mach disk

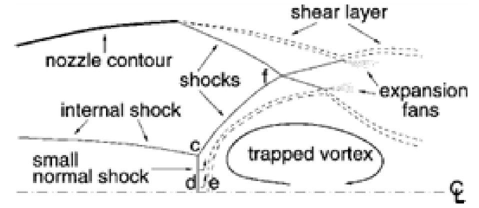

b) Cap-shock pattern with trapped vortex

Figura 2.7: Shock patterns in the exhaust plume of a thrust optimized nozzle (Taken from [2][Fig. 7])

with the surface adheres to it, resulting in zero velocity relative to the surface.
Moving away from the wall in the y-direction, the velocity of the flow increases until it's equal to the freestream velocity. This will occur at a certain distance from the wall which is defined as the velocity boundary layer thickness. The consequence of the velocity gradient at the wall is the generation of shear stress:

$$\tau_w = \mu \left(\frac{\partial u}{\partial y} \right)_w \tag{2.1}$$

A similar argument can also be made for the temperature. On the contrary the static pressure remains nearly constant, being dictated by the conditions in the external flow just outside the boundary layer.

It is worth noting that this division of the flow into a viscous near-wall region and an inviscid outer region becomes especially valid in high Reynolds number flows. In such conditions, the no-slip condition at the wall leads to a very thin boundary layer, where both velocity and temperature adjust rapidly to match the free-stream values. Beyond this thin layer, viscous effects become negligible, and the flow can be reasonably approximated as inviscid.

2.2.2 Flow separation

Flow separation is a fundamental phenomenon in fluid dynamics that occurs when the boundary layer detaches from the surface of a body. When the freestream pressure increases in the direction of flow, it is known as an adverse pressure gradient. The fluid particles within the boundary layer, especially those near the wall with lower momentum, may not possess sufficient kinetic energy to overcome this gradient. As a result, the flow can decelerate to the point of reversal, leading to a detachment of the boundary layer from the surface. This process is known as separation.

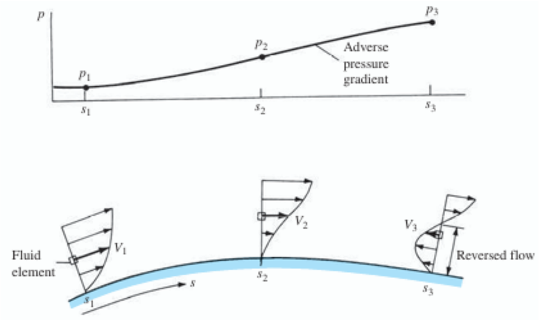

Figura 2.8: Separated flow induced by an adverse pressure gradient (Taken from [17][Fig. 15.3])

In a favorable pressure gradient, when pressure decreases along the flow direction, the boundary layer remains energized, and the fluid particles continue to follow the surface. However, in the presence of an adverse pressure gradient the low-momentum fluid particles close to the wall begin to decelerate. The onset of flow separation is most directly related to the behavior of wall shear stress. As the adverse pressure gradient increases, the velocity gradient in the wall decreases and the wall shear stress decreases correspondingly. Flow separation occurs when the wall shear stress reaches zero and then becomes negative, indicating a local flow reversal near the wall.

$$\tau_w = \mu \left(\frac{\partial u}{\partial y} \right)_w = 0 \qquad \left(\frac{\partial p_w}{\partial x} \right)_{x,separation} > 0 \tag{2.2}$$

Flow separation requires the existence of both friction and an adverse wall pressure gradient in a flow along a body. If one of these two conditions is suppressed, flow separation can be prevented. Another important aspect is whether the boundary layer is laminar or turbulent. A laminar boundary layer, characterized by smooth and orderly flow, generally exhibits lower skin friction but is much more susceptible to flow separation under adverse pressure gradients. A turbulent boundary layer, in contrast, features enhanced momentum mixing that allows it to better resist separation, at the cost of higher wall friction.

In high-speed applications such as supersonic nozzles, this distinction becomes even more critical. The interaction between shock waves and the boundary layer introduces strong adverse pressure gradients, making the separation process highly sensitive to the instantaneous state of the boundary layer. This coupling represents one of the dominant mechanisms governing nozzle unsteadiness and pressure fluctuations that can generates powerful lateral forces, commonly referred to as side loads as we will see in 2.2.3.

Role of the Boundary Layer State

As anticipated, the state of the boundary layer plays a critical role in determining the characteristics of SWBLI and the resulting flow separation within rocket nozzles. Particularly in cold-flow or sub-scale nozzle tests, the boundary layer state often dominates the overall separation dynamics and the amplitude of pressure fluctuations. A laminar boundary layer is highly sensitive to the adverse pressure gradient imposed by the incident shock, which can induce early and extended separation regions. These separation bubbles are typically large, unstable, and prone to low-frequency oscillations of the separation shock. Conversely, a turbulent boundary layer, due to its enhanced momentum exchange between near-wall and outer-layer fluid, resists separation more effectively. The separation point is displaced downstream, and the separation bubble is shorter but often associated with higher-frequency content in the pressure spectra. Between these two limits lies the transitional regime, in which the boundary layer is neither fully laminar nor fully turbulent. Such conditions have been shown to produce highly sensitive and intermittent separation behavior, with localized turbulent patches affecting the stability of the separation bubble [18].

2.2.3 Shock wave - boundary layer interaction

Shock Wave - Boundary Layer Interaction (SWBLI) represent a critical and complex phenomenon in high-speed aerodynamics. It can generally be stated that when a shock wave interacts with the boundary layer, the flow within the boundary layer slows down as a result of the interaction itself. The large pressure rise across the shock wave acts as a severe adverse pressure gradient imposed on the boundary layer, causing the boundary layer to locally separate from the surface. The separated boundary layer deflects the external supersonic flow into itself, thus inducing a second shock wave, identified in Figure 2.9 as the *induced separation shock wave*. The separated boundary layer subsequently turns back toward the plate, reattaching to the surface at some downstream location. Here again, the supersonic flow is deflected into itself, causing a third shock wave called the *reattachment shock*. Between the separation and reattachment shocks, where the boundary layer is turning back toward the surface, the supersonic flow is turned away from itself, generating expansion waves.

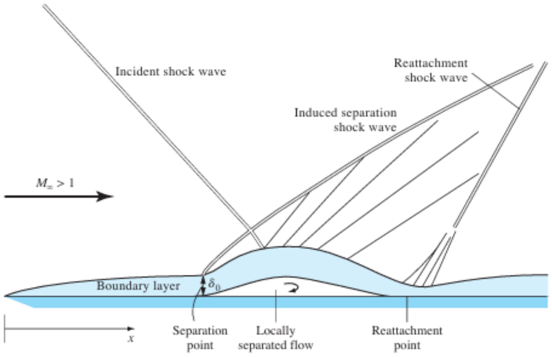

Figura 2.9: Schematic of the shock-wave/boundary-layer interaction (Taken from [17][Fig. 9.40])

2.2.4 Flow separation in rocket nozzle

The main engines of a rocket usually operate from take-off at sea-level up to high altitudes with very low ambient pressures. In order to obtain an optimum performance throughout the flight trajectory, the nozzles are designed for an intermediate ambient pressure. This design ambient pressure is chosen high enough to prevent flow separation inside the nozzle during steady-state operation at sea level. As a result, during ground testing or at low altitudes, these nozzles operate in an over-expanded regime. In this condition, the adverse pressure gradient in the divergent section can cause the boundary layer to separate from the wall. The interaction between the separated boundary layer and internal shock structures often results in unsteady and asymmetric flow patterns, known to induce side loads and potentially harmful structural oscillations. Two types of separation patterns are commonly observed: the **Free Shock Separation (FSS)**, where the flow detaches and does not reattach, and the **Restricted Shock Separation (RSS)**, where the flow reattaches after a separation bubble [2].

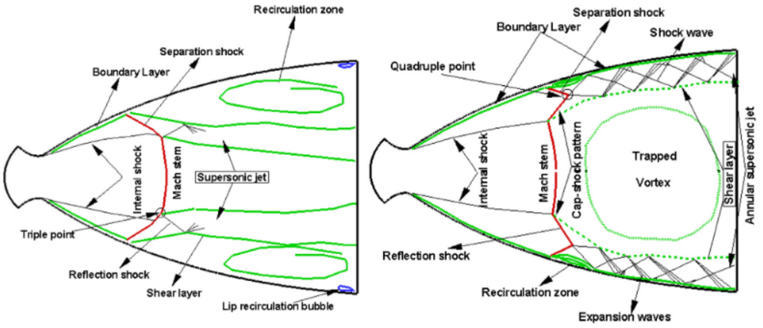

Figura 2.11: Sketches of the flow structure in the FSS (left) and the RSS (right) regimes. (Taken from [19][Fig. 1])

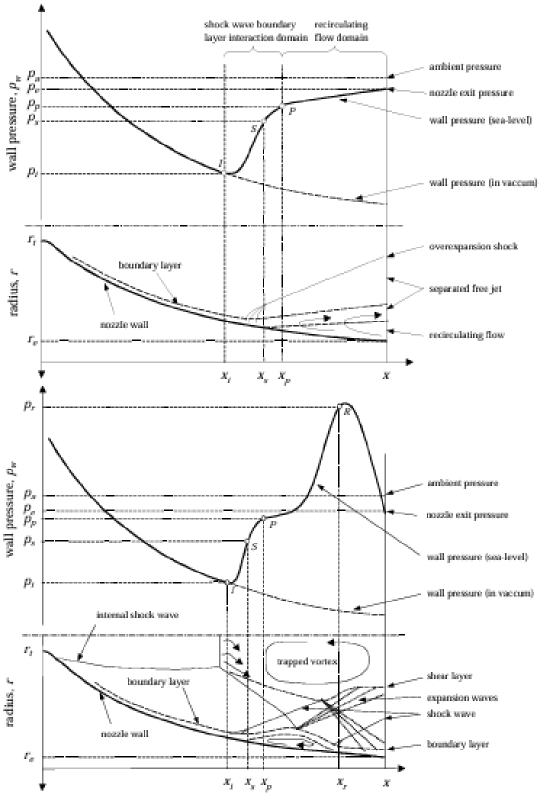

Figura 2.10: Phenomenological sketch of free shock separation (top), and restricted shock separation (bottom) (Taken from [4][Fig. 37])

Free Shock Separation

In the Free Shock Separation case, figure 2.10 (top), the overexpanded nozzle flow fully separates from the wall once a certain wall-to-ambient pressure ratio is reached. The evolution of the wall pressure along the streamwise direction is primarily governed by the shock wave–boundary layer interactions occurring in any supersonic flow separation. The initial deviation of wall pressure from the ideal vacuum profile is commonly referred to as the incipient separation pressure p_i. From this point on, the wall pressure rapidly increases to a nearly constant value known as plateau pressure p_p, which typically remains slightly below ambient pressure p_a. It has been observed that the boundary layer effectively separates from the nozzle wall shortly before the plateau pressure is reached. In the recirculation zone downstream of the separation point, the wall pressure then gradually increases from p_p to the exit pressure, p_e. This gradual rise is due to the inflow and upstream acceleration of ambient gas into the recirculation region.

Restricted Shock Separation

In the Restricted Shock Separation case, figure 2.10 (bottom), the pressure downstream of the separation point showed an irregular behaviour, reaching values above the ambient pressure. This is attributed to a reattachment of the separated flow to the nozzle wall, which generates a pattern of alternating shocks and expansion waves along the wall. This transition from FSS occurs at a well-defined pressure ratio and is also characterized by a sudden downstream shift of the separation point. Beyond the reattachment point in RSS, supersonic flow resumes along the nozzle wall, generating shocks that lead to the previously mentioned wall pressure peaks exceeding ambient pressure. Between the separation and the reattachment points, a closed recirculation zone forms, characterized by static pressures significantly below ambient levels. As the thrust chamber pressure ratio increases further, the closed recirculation zone is gradually pushed toward the nozzle exit until the reattachment point reaches it, causing the recirculation zone to open to the ambient flow. This results in a pressure increase within the recirculation region behind the separation shock, pushing the separation point upstream once again. The recirculation zone then closes, causing a drop in static pressure and another downstream movement of the separation point. This cycle produces a pulsating behavior, marked by the repeated opening and closing of the separation zone. The re-transition from RSS back to FSS is commonly referred to in the literature as the End-Effect Regime (EER). The same phenomena can also be observed during engine shutdown, even though the transition now from RSS to FSS occurs in general at a different lower pressure ratio than the corresponding transition FSS-RSS during start-up. According to the literature [20], the key factor for the transition from FSS to RSS and vice versa is the specific cap-shock pattern. Thus, a transition from FSS to RSS can only occur in nozzles with an internal shock as the cap-shock pattern results from the interference of the separation shock with the inverse Mach reflection of the weak internal shock at the centreline.

Three-Dimensional Effects, Asymmetry and Side-Loads

Real nozzle flows are inherently three-dimensional. This means that the regimes previously described only provide a useful framework. The unsteady separation pattern often develops significant azimuthal asymmetry, leading to side loads on the nozzle structure. These asymmetries are linked to the excitation of azimuthal modes, particularly the $m = 1$ sloshing mode, which corresponds to a lateral oscillation of the internal shock and separation line. In contrast, the $m = 0$ flapping mode represents purely axial shock motion without net lateral force [5, 6]. Nguyen et al. and Deck and Nguyen demonstrated that side-load peaks are closely correlated with transitions between FSS, RSS, and EER. Baars et al. [21] further showed that within the EER, the energy content of the $m = 0$ mode reaches a maximum, but its nonlinear interaction with the $m = 1$ component amplifies lateral loads.

Another important aspect of nozzle unsteadiness is the presence of hysteresis. The transition between flow states during start-up and shutdown does not occur at the same pressure ratio. This hysteresis is not only associated with the position of the separation shock but also with a fundamental change in the side-load generation mechanism. During shutdown, as the flow passes through the EER, asymmetric separation patterns and unsteady reattachment can cause large transient lateral forces.

Additionally, the separated flow region in a rocket nozzle is not a simple planar bubble but a curved three-dimensional volume. The curvature of the wall and streamline patterns can trigger streamwise counter-rotating vortices, known as Görtler-like vortices, arising from centrifugal instabilities near the reattachment or separation zones. Verma and Haidn [22, 23] demonstrated that, during the RSS phase, the separated shear layer periodically reattaches to the wall, forming a closed recirculation bubble whose size and location strongly depend on the local pressure ratio. High-speed schlieren and oil film visualizations revealed that the reattachment process is inherently three-dimensional, with the appearance of streamwise vortical structures generated by wall curvature effects in the reattachment zone. These vortices induce local distortions of the separation line and promote asymmetric pressure distributions, providing a physical basis for the unsteady side-loads observed in this regime. Furthermore, Verma and Haidn noted that the transition during the shutdown sequence coincides with the amplification of these three-dimensional instabilities, confirming their crucial role in nozzle hysteresis and unsteady separation dynamics.

2.3 Frequency Analysis

As mentioned, flow separation in overexpanded nozzles is inherently an unsteady phenomenon. To quantify these unsteady effects, frequency analysis techniques are employed on time-resolved signals and can help in characterizing the internal Shock Wave - Boundary Layer Interaction. During FSS, the separation shock exhibits a low-frequency, large-scale oscillatory motion [1]. In contrast, the RSS regime is generally characterized by a more stable separation line. However, the Shock Wave - Boundary Layer Interaction (SWBLI) in the reattachment region generates high-amplitude pressure peaks and higher-frequency fluctuations. To quantify these unsteady effects, frequency analysis techniques are employed. Experimentally, this involves the post processing of time-resolved signals. The Fast Fourier Transform (FFT) is then applied to these signals to decompose them from the time domain into the frequency domain, revealing the dominant spectral components. To allow for meaningful comparison between experiments performed on different scales and under various operating conditions, the observed frequencies are often rendered dimensionless using the Strouhal number

$$St = \frac{fL}{U} \tag{2.3}$$

where f is the characteristic frequency (Hz), L is a characteristic length (e.g., the nozzle diameter at the separation point or the length of the separation region), and U is a characteristic velocity (e.g., the freestream velocity just outside the boundary layer). Experimental studies have shown that the low-frequency shock oscillation often associated to a relatively narrow range of the Strouhal number, suggesting that the flow mechanisms are independent of the size of the nozzle. For separation in overexpanded nozzles, characteristic Strouhal numbers based on the length of the separation region are often reported to be in the range of $St \approx 0.02 - 0.2$ [24, 25, 26, 27].

Capitolo 3

Flow Visualization and Measurement Techniques

In order to investigate the flow phenomena under study, an appropriate combination of flow visualization methods and measurement techniques was employed. This chapter provides a detailed description of the working principal of the methods used, as well as the design parameters used to model the setup.

3.1 Background Oriented Schlieren (BOS)

Optical methods to determinate the density field of a fluid typically rely on visualizing variations in the refractive index within the flow. These techniques can be grouped into three main categories: schlieren, shadowgraphy, and interferometry. Each of these methods takes advantage of how light waves bend, or “refract”, over changes in the refractive index field, leading to noticeable shifts in the intensities captured by an imaging system. The **Background Oriented Schlieren (BOS)** is a a non-intrusive schlieren-based technique that tracks the distortion of a structured, random background pattern seen through the fluid.

3.1.1 Principles of Schlieren techniques

[28]The speed of light in a transparent medium, c, is related to the speed of light in a vacuum, $c_0 \approx 3 \cdot 10^8 \quad m/s$, through the refractive index:

$$n = \frac{c_0}{c} \tag{3.1}$$

In general, the refractive index depends on the wavelength of light, λ, and the thermochemical state of the medium, including its density, temperature, pressure, and composition. Every Schlieren techniques is based on the relation between the refractive index of a fluid and it's density, given by the Lorentz–Lorenz equation, which can be simplified to the Gladstone–Dale equation for gaseous media.

$$n = 1 + G\rho \tag{3.2}$$

where G is the Gladstone–Dale coefficient which for dry air and visible light is $G = 2.26 \cdot 10^{-4} \quad m^3/kg$. The principle of refraction is usually explained by the example of a discrete interface, such as a light beam passing from a medium with refraction index n_1 to another with refraction index n_2. As the beam transitions between these media, its speed changes, resulting in a shift in the light beam's trajectory at the interface. This change is governed by Snell's Law:

$$n_1 sin(\epsilon_1) = n_2 sin(\epsilon_2) \tag{3.3}$$

where $\epsilon_1$and ϵ_2 are the angles of incidence and refraction. The amount of bending the light ray has is dictated by the difference in the two indices of refraction. When light passes into a denser medium, the ray is bent toward the normal. When coming obliquely from a denser medium is bent away from the normal. In the special case where the incident beam is perpendicular to the boundary, it will experience a change in phase velocity but will continue traveling in the same direction. This principle can be generalized to media with continuously varying refractive indices. It can easily be shown, that the deflection of a single beam contains information about the spatial gradient of the refractive index integrated along the optical path. Assuming paraxial recording and small deflection angles a formula for an image displacement Δy can be derived:

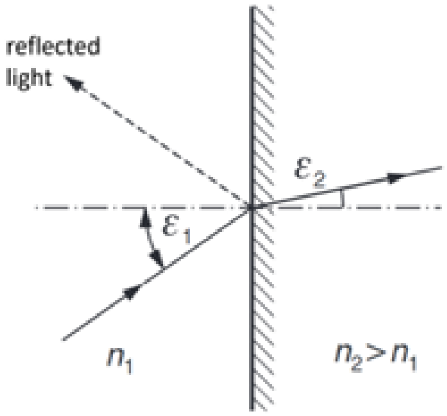

Figura 3.1: Snell's law type refraction and reflection at interface (Taken from [28][Fig. 1])

$$\epsilon_y = \frac{1}{n_o} \int \frac{\delta n}{\delta y} dz \tag{3.4}$$

A similar formula yields an analogous expression for ϵ_x. This deflections can be interpreted as density gradients – integrated along the optical path - by using the Gladstone-

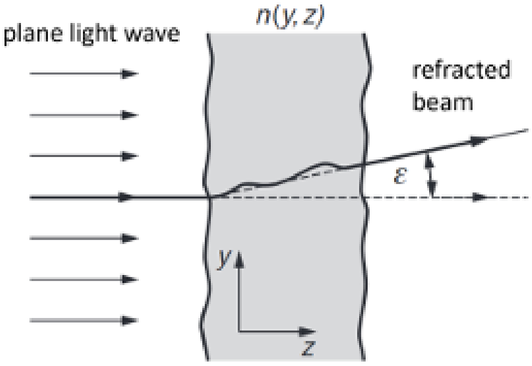

Figura 3.2: Light refraction through a variable-index medium. (Taken from [4][Fig. 1])

Dale equation.

3.1.2 BOS measurements

In the BOS configuration, a camera is focused through the working fluid onto a background plane with a visible random pattern. Two sets of images are typically captured: the first set is taken when the flow is quiescent, allowing light to pass through the domain without refraction, thereby producing a clean "reference" image of the background. The second set is captured once the flow is activated, at which point the density gradients introduce phase disturbances that refract the light, resulting in "deflected" (or distorted) images of the pattern. Once the reflected and deflected images have been acquired, the two-dimensional deflection field can be calculated using one of several types of algorithms.

Design parameters

Key distances in the setup include the total background-to-lens distance Z_B, i.e. the sum of the background-to-phase object distance Z_D and the phase object-to-lens distance Z_A, and the distance from the lens to the sensor Z_i. A basic single-camera BOS setup is shown in Fig.3.3. The magnitude of displacements observed depends on both the experimental setup and the fluid and flow properties. Assuming paraxial recording and small deflection angles, a formula for the image displacement Δy can be derived:

$$\Delta y = Z_D M \epsilon_y \tag{3.5}$$

with $M = Z_i/Z_B$ the magnification factor of the background, defined also as the ratio between sensor size and object size. The image displacement can thus be rewritten as:

$$\Delta y = f \frac{Z_D}{Z_B - f} \epsilon_y \tag{3.6}$$

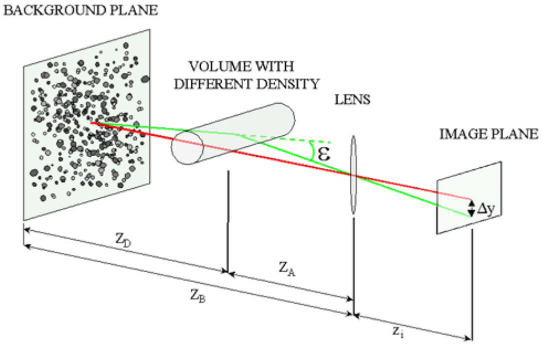

Figura 3.3: Sketch of BOS imaging setup (Taken from [4][Fig. 3])

with f the focal length of the lens. Since the imaging system has to be focused onto the background, the following formula applies:

$$\frac{1}{f} = \frac{1}{Z_i} + \frac{1}{Z_B} \tag{3.7}$$

It is possible to summarize all the parameters related to the experimental setup in a single specific sensitivity factor:

$$S = f \frac{Z_D}{Z_D + Z_A - f} \tag{3.8}$$

Equation 3.8 shows that a high image displacement can be obtained with a large Z_D and a small Z_A. For $Z_D \to \infty$ $\Delta y \to f\epsilon_y$. However, practical constraints limit the decrease of Z_A. The necessity of maintaining the object in reasonable focus while keeping the plane of best focus on the background pattern generally imposes limitations on the extent to which the object can be brought closer to the camera. When planning an experiment, the size of the Field Of View (FOV) is often the main boundary condition: for a fixed FOV size and a given setup length $Z_B = Z_A + Z_D$, a variation of Z_A leads to a maximum sensitivity S at $Z_A/Z_B = 0.5$. Sensitivity can also be modulated by adjusting camera parameters: When the setup length Z_B is increased at a constant ratio of Z_A/Z_B, lenses with a higher focal length are required, which results in a higher sensitivity factor.

With regard to the spatial resolution, the two main limiting factors are the geometric blur of the schlieren object and the choice, as well as the settings, of the processing algorithm. A more detailed discussion of the role of latter is provided in Section3.1.3. Therefore, this section will focus on the former. The geometric blur of the captured Schlieren object is an inherent feature of the BOS technique and a key factor in the achievable resolution. In traditional photography, image blur is indicated by the Circle of Confusion (CoC), that is the point of blur created in the image plane of the camera.

$$CoC = \frac{f^2 Z_D}{f_{\#} Z_A (Z_B - f)} \tag{3.9}$$

The size of the CoC and the sensitivity of the setup are found to be linearly related; An increase in sensitivity leads to a proportional increase in geometric blur when the $f_{\#}$, FOV, and sensor size are held constant. Therefore, for a given S, the aperture of the camera becomes the most significant parameter, enabling a change in the minimum size of the resolvable feature. Higher $f_{\#}$ (smaller aperture) produces also a larger depth of field which can allow for increased sensitivity while maintaining focus. However, this can also impact illumination, which becomes a limiting factor.

Solving the Poisson Equation

Assuming **parallel light rays** and a **weakly refracting flow**, the **Poisson equation** can be used to recover the density field:

$$\frac{\partial^2}{\partial x^2}\rho^*(x,y) + \frac{\partial^2}{\partial y^2}\rho^*(x,y) = S(x,y) \tag{3.10}$$

In this equation:

- $\rho^*(x,y)$ represents the **line-of-sight integrated density field**.
- $S(x,y)$ is the **source term**, which is proportional to the divergence of the displacement field ($\nabla \cdot \mathbf{\Delta x}$).

The source term S incorporates the optical and gas dynamic scaling factors, including the **Gladstone-Dale constant (**G**)**, the ambient refractive index (n_0), and the geometric terms (Z_B, Z_D, f):

$$S = \frac{Z_B}{Z_D f}\frac{n_0}{G}\left(\frac{\partial \Delta x}{\partial x} + \frac{\partial \Delta y}{\partial y}\right) \tag{3.11}$$

The goal of the final processing step is to transform the quantitative displacement field $\mathbf{\Delta x}$ into the physical parameter of interest: the line-of-sight integrated density field $\rho^*(x,y)$. This is achieved by solving the Poisson equation:

$$\nabla^2 \rho^*(x,y) = S(x,y) \tag{3.12}$$

3.1.3 Deflection sensing algorithm

Unlike traditional Schlieren imaging, the BOS procedure requires the implementation of an image processing routine of some kind. A simple but fast approach that gives a rough indication of the types of features that will be visible is simply to subtract the deflected image from the reference image. However, to obtain a proper schlieren image, more sophisticated algorithms are required. The most common algorithm to be applied to process BOS images is **Cross-Correlation (CC)**, which is usually used for Particle Image Velocimetry (PIV) processing. It is typically achieved by dividing the images into sub-regions of a certain size called Interrogation Window (IW). The intensity distribution in each window is then correlated across the reference and deflected images, leading to a correlation map where the peak corresponds to the most likely average displacement of the background pattern in the IW between the flow-off and flow-on images. This operation is performed for all IW's producing a map where the displacement in x and y is given at each IW's center location. This operation is performed in the Fourier domain, which makes it highly computationally efficient. Since the averaging is done for all the pixels in the IW, the resolution of the resulting images is reduced. This can be partially mitigated by using an overlap factor, at the cost of an increased computational time.

Capitolo 4

Nozzle Configuration and Experimental Arrangement

In order to fulfill the research objective, a number of test cases have been conducted on an axysimmetric TOP contoured nozzle. In this Chapter we briefly summarize the iterative process that led to the final design of the test nozzle and we provide an overview of the experimental setup.

4.1 Nozzle Description

The nozzle used in this study, that was created by Nallo [29], is a modified version of the PAR3 contour, a specific profile used on TOP shaped nozzle, that was originally created and tested in earlier experiments at TuDelft. To meet the limitations of the test facility and to encourage the researched phenomena to occur at lower Nozzle Pressure Ratios (NPR), the original profile was intentionally truncated. This adjustment gave a more compact nozzle shape, making it easier to integrate into the wind tunnel while still being able to produce key flow separation patterns, in particular Free Shock Separation (FSS), Restricted Shock Separation (RSS) and the End-Effect Regime (EER). The main geometric characteristics and ideal operating conditions of the nozzle are summarized in Table 4.1. In order to meet the practical constraints of manufacturing and testing, the nozzle was produced using fused deposition modeling (FDM) 3D printing with polylactic acid (PLA) filament. This method was chosen for its rapid prototyping capability and cost-effectiveness, allowing quick replacement or redesign if required. In order to enhance the structural rigidity of the object and minimize its susceptibility to vibrations or cracking during testing, a high infill percentage and thickened walls were used. Post-processing included careful sanding of the inner surface to reduce surface roughness, a phenomenon that is more pronounced in plastic-printed components than in machined metal ones. Furthermore, 0.3 mm holes were drilled to connect internal pressure sensor ports to the flow path. The small diameter of

Property	**Symbol**	**Value**	**Unit**
Throat radius	R_t	8.175	mm
Exit radius	R_e	41.135	mm
Expansion ratio	$\epsilon = A_e/A_t$	25.33	-
Axial length	L	78	mm
Mass flow rate	$\dot{m}$	2	kg/s
Thrust	T	712.7	N
Exit pressure	p_e	30.36	kPa
Exit velocity	v_e	718.95	m/s
Exit Reynolds number	Re_e	3.61×10^6	-
Chamber pressure	p_c	40	bar
Atmospheric pressure	p_a	101.325	kPa
Chamber temperature	T_c	288	K

Tabella 4.1: Nozzle data and ideal operating conditions

these holes is needed to minimize disturbances to the internal flow field, thereby ensuring accurate measurements of wall pressure. A total of 16 pressure ports were integrated into the nozzle wall along the axial direction, arranged in three rows spaced 120° apart.

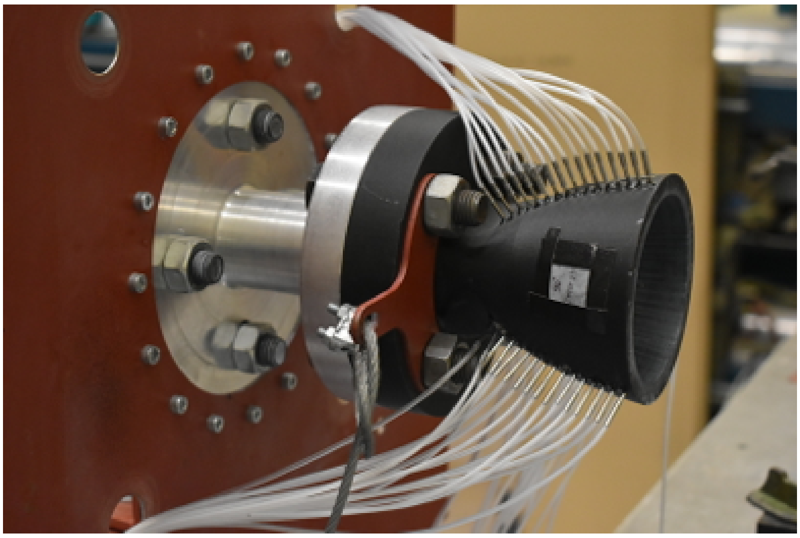

Figura 4.1: 3D printed Test nozzle

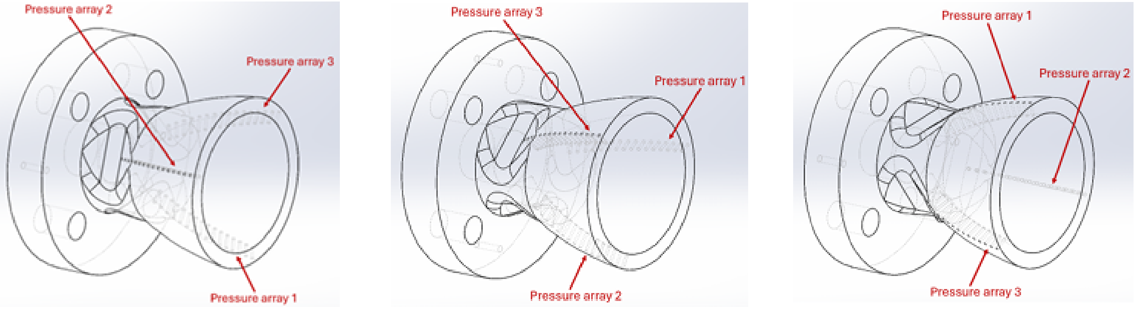

(a) 0° test configuration **(b)** 90° test configuration **(c)** 180° test configuration

Figura 4.2: Nozzle rotation: pressure sensors configurations

4.2 ASCENT Facility

The experimental campaign was conducted using the ASCENT nozzle test facility [30]. The rig consists of a horizontal test bench securely mounted on four structural legs and connected to a pressurized air supply system upstream. Downstream, a large diffuser directs the flow out of the laboratory and reduce back pressure effects.

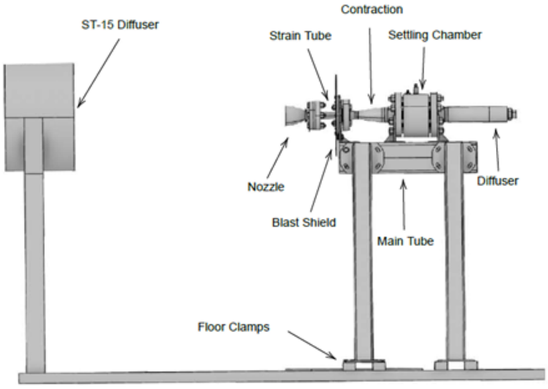

Figura 4.3: ASCENT rig

The test rig is supplied with dry, unheated air at room temperature $T_0 = 288K$, stored in a large $300m^3$ high-pressure reservoir. This tank allows for stagnation pressures of up to $40bar$, enabling a maximum NPR of approximately 32. As mentioned before this was a constraint that directly influenced the design of the nozzle, which was truncated to ensure the appearance of specific separation regimes within this pressure range. The ASCENT rig provides rotational capability, at 0°, 90°, and 180°, allowing also for azimuthal variation in pressure measurements.

4.3 Experimental setup

Based on the considerations given in this and in Chapter 3, an experimental setup was created in the ST Room of the High Speed Laboratory at TU Delft's Faculty of Aerospace Engineering. The experimental setup consists of two main components: the ASCENT test rig and the camera-background array. The first one has been discussed in section 4.2. The camera-background array was made using a series of X95 structural beams.

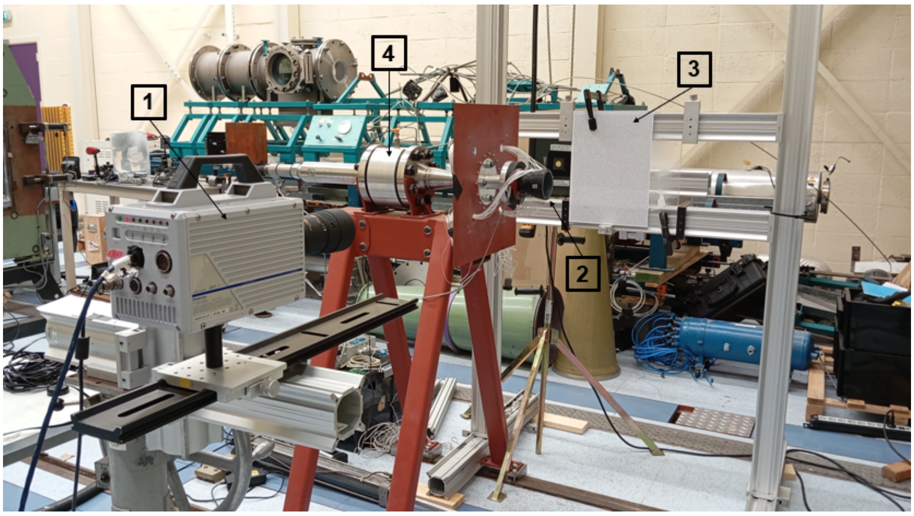

Figura 4.4: BOS setup. 1: High speed camera 2: Nozzle 3: Background 4: ASCENT rig

Two main supporting structures were made: one designed to hold the camera, allowing adjustments in position, height and pitch, and another to support the background pattern, which was firmly clamped to prevent any movement during the recordings. The camera-background pair was aligned in a plane orthogonal to the nozzle symmetry axis, with the background positioned directly opposite to the camera. To provide sufficient illumination, a number of LED lights were placed behind the speckle pattern. To better visualize the setup, a right hand coordinate system is used. The x-axis is aligned with the primary axis of the nozzle, the y-axis points up, and the z-axis is horizontal. Note that with reference to this coordinate system, the camera and background are aligned along the z-direction.

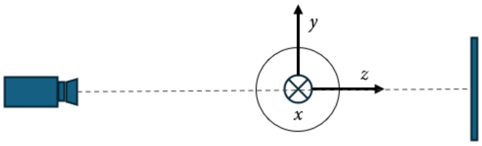

Figura 4.5: Schematic of experimental setup

Background

Based on the nozzle geometry and on the parameters of the experimental setup, the speckle-pattern background was designed. Given that the CC algorithm used for BOS in this study was initially developed for PIV, they are often paired with a background pattern consisting of random dots to emulate tracer particle images encountered in PIV. Our random dots scheme was generated such that the size of the dots corresponded to 3-5 pixels in the camera's image plane. Starting from the camera parameters, the desired dimension of the dots in $[mm]$ was found. The corresponding size in pixels was then obtained by applying a conversion factor $[mm/px]$, which was derived from the known physical dimensions of the $A3$ paper used to print the background. This final dot size, together with a minimum spacing between the dots and the overall pattern density, was used to generate the random background pattern. To ensure enough stiffness and to keep the background as fixed as possible during testing, which is essential for accurate measurements, the pattern was then mounted on rigid Plexiglas panel and clamped to the dedicated structure.

4.4 Test procedures and Data acquisition

To investigate the flow behavior, different measurements were performed at selected NPR during the start-up stage. Previous studies at TuDelft [29] have shown that the transition to the RSS regime occurs around $NPR \approx 22$, while the end-effect regime is reached at $NPR \approx 26$. On this basis, several NPR values were selected in order to capture the flow during the desired configurations of interest. In addition, particular attention was also given to the occurrence of flow asymmetries during the FSS regime. Based on this knowledge, the BOS experimental campaign was divided into two main parts. In the first, a standard BOS setup was employed to capture the entire nozzle and exhaust plume. This configuration enabled the identification of the dominant flow structures, mechanisms, and instabilities over the full field of view. In the second part, a High Resolution Background Oriented Schlieren (HRBOS) setup was adopted, focusing on the bottom half of the nozzle exit. While this reduced the spatial coverage, it allowed for a significant increase in temporal resolution, thereby enabling frequency-domain analyses. In this configurations, spectral investigations of the flow were carried out at each selected NPR, providing further insight into the characteristic unsteady behavior of the jet. A summary of the optical parameters and equipment used is given in table 4.2. A test Matrix is also presented in Table 4.3.

Parameters	**STBOS**	**HRBOS**
FOV (plane of the nozzle)	$100mm$	$60mm$
Acquisition frequency	$5400Hz$	$3000Hz$
Magnification factor	0.2	0.35
Camera model	Photron FASTCAM SA1.1	
Pixel size	20 μm	
Exposure time	1 / Frame Rate	
Test run duration	10 s	

Tabella 4.2: Optical parameters and equipment used

CAMPAIGN	**NPR**	**Pixel Resolution**	Z_D [cm]	**Focal length** [mm]	**Aperture**	**Mode**
1	20	1024×1024	70	200	1/8	STANDARD
1	24	1024×1024	70	200	1/8	STANDARD
1	20	1024×1024	50	1.8×200	1/8	HRBOS
1	24	1024×1024	50	1.8×200	1/8	HRBOS
2	16	1024×1024	25	180	1/16	STANDARD
2	18	1024×1024	25	180	1/16	STANDARD
2	20	1024×1024	25	180	1/16	STANDARD
2	24	1024×1024	25	180	1/16	STANDARD
2	16	512×512	25	180	1/22	HRBOS
2	18	512×512	25	180	1/22	HRBOS
2	20	512×512	25	180	1/22	HRBOS
2	24	512×512	25	180	1/22	HRBOS

Tabella 4.3: Text Matrix

An iterative design approach was used to meet theoretical considerations and limitations of the technique, such as linking camera specifications, optical parameters, and key distances to the final result. This closed-loop optimization process was applied moving from the first to the second experimental campaign and is detailed in Figure 4.6. In our setup, the sensitivity does not play a crucial role due to the high-density gradient inherent in the flow. Therefore, our optimization efforts focused instead on reducing the geometric blur by repositioning the structure holding the background.

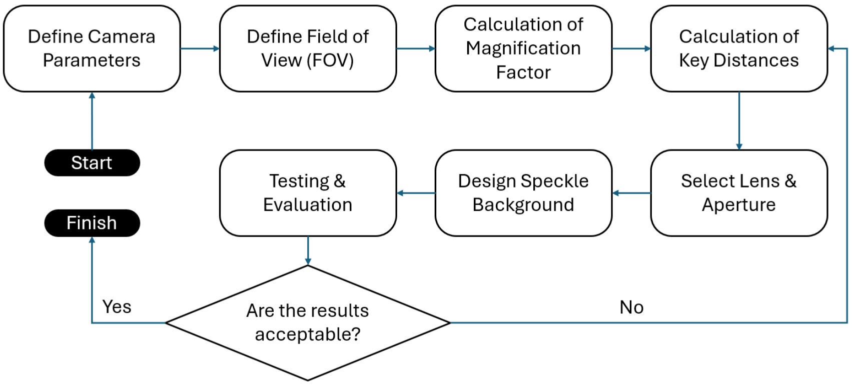

Figura 4.6: Workflow of the experimental campaigns

The pressurization process is controlled via a hand-operated control valve and a pneumatically actuated main valve. In each test, the desired NPR value was reached by opening the pneumatic one and by manually adjusting the hand-operated controlled one. The entire ASCENTS facility is also supported by an electronic control box that houses the power supply, terminal blocks and relay switch. To record the measurements, a computer was connected to a high-speed camera via an Ethernet cable. During each test, the camera was operated using a dedicated app, which provided an interface with the camera and allowed the various data acquisition parameters to be changed. Furthermore, during each test, another computer also collected NPR data at $20Hz$. A custom LabVIEW interface was previously developed to manage the control and monitoring of the experiments. The interface serves as the main control panel for the operator and allows to open and close the main valve as well as to monitor the NPR in real time, which is calculated by dividing the total pressure measured by an upstream sensor (via a NI DAQ module) by the input atmospheric pressure. It features a user-friendly dashboard that shows current pressure readings and the status of each valve. A dedicated trigger button is also included, which opens the pneumatically actuated main valve. When clicking the 'Start Measurement' button, the data acquisition process begins and the system records measurements for the specified duration of the 'measurement time' in milliseconds, at the defined 'sampling rate'. The 'Stop Test' command button is also present: it ends all active loops and can be used to stop measurements at any time. Additionally, an external emergency Panic button is built into the interface: When activated, it instantly closes the main valve and vents the system to avoid overpressure or any unexpected incidents. A detailed schematic of the setup hardware connections is shown in figure 4.7

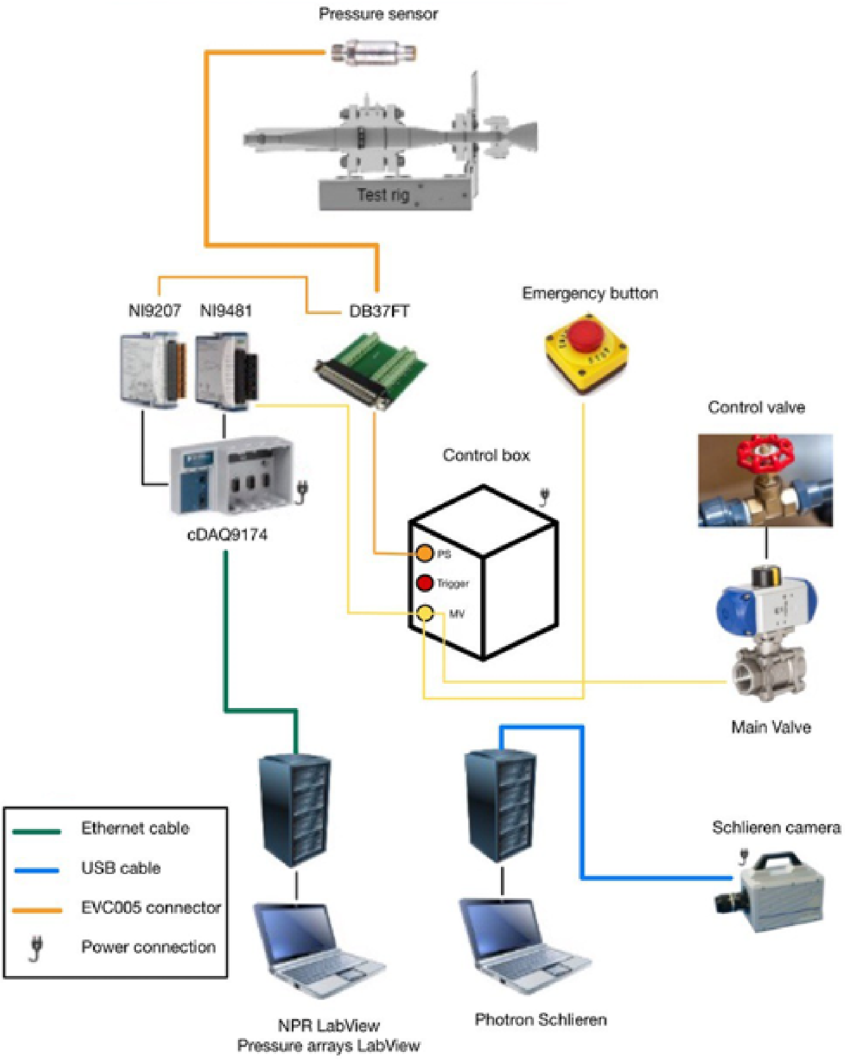

Figura 4.7: Acquisition system functional scheme

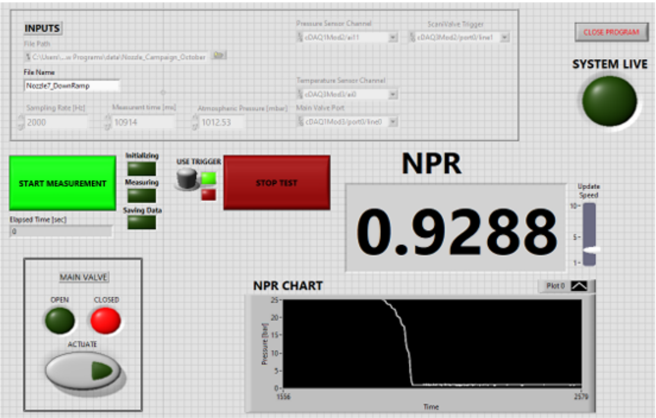

File Path: C:\Users\...w Programs\data\Nozzle_Campaign_October
File Name: Nozzle7_DownRamp
Sampling Rate [Hz]: 2000
Measurent time [ms]: 10914
Atmospheric Pressure [mbar]: 1012.53
Pressure Sensor Channel: cDAQ1Mod2/ai11
ScaniValve Trigger: cDAQ3Mod2/port0/line1
Temperature Sensor Channel: cDAQ3Mod3/ai0
Main Valve Port: cDAQ1Mod3/port0/line0
Elapsed Time [sec]: 0
NPR: 0.9288

Figura 4.8: LaibView control interface

Capitolo 5

Data Processing

This chapter aims to explain the data processing procedure applied to analyze the different experimental results. It presents the BOS code used for processing the images of the flow, the code used for the spectral analysis, and the reduced model reconstruction used to describe the flow.

5.1 Post-processing code for BOS data

The post-processing of the BOS measurements was performed using a dedicated code originally developed within the faculty for PIV applications. *Dr.ir. F.F.J. (Ferdinand) Schrijer* adapted the code to meet the requirements of BOS image processing, implementing the necessary modifications to handle displacement fields rather than velocity fields. The code was further modified to manage the dataset of the present study.

5.1.1 Input file

The post-processing algorithm works based on a *.dat* control file. This file is divided into three main parts:

- ***INPUT/OUTPUT SETTINGS***: In this section, you can define the path for the program itself, as well as for the reference and raw images. You can also specify the format of the images and select the sequence of frames to be processed. Finally, the user can also choose the path and name of the output files.
- ***PROCESSING SETTINGS***: In this section, you can define the parameters that control the cross-correlation procedure and the interrogation strategy applied to the image pairs. The user can determine the size of the image to be analyzed, the initial and final Interrogation Window sizes, and the degree of overlap between adjacent windows, which directly affects the spatial resolution of the resulting displacement field.

- ***ADVANCED AND POST PROCESSING SETTINGS***: In this section, you can refine the displacement fields obtained during processing as well as select the application of smoothing routines to stabilize convergence. Furthermore, this section also provide tools for statistical evaluation of the processed fields. The user can choose to produce a statistic file in which the mean of all processed images is computed.

Once the input *.dat* file has been properly configured, the post-processing routine can be executed directly from the MATLAB command window by calling the main function and providing the path to the control file as an argument. While the program is running, it continuously prints status messages to the command window, enabling the user to monitor the computation's progress. In case of inconsistencies, the code outputs error messages that specify the nature and location of the issue.

5.1.2 Output file

At the end of every iteration, the code automatically generates an output file in the designated directory. For each processed image, a dedicated Techplot-compatible file is created, containing the averaged displacement field obtained through the iterative refinement procedure of the single image defined in the input control file. The structure of these files is as follows:

```
VARIABLES = "x", "y", "dx", "dy", "sigx", "sigy", "SN", "INFO"
```

Here, (x, y) represent the coordinates of the interrogation window centers, (dx, dy) are the measured displacements, (σ_x, σ_y) indicate the width of the CC peak, SN refers to the Signal-to-Noise Rateo (SNR), and $INFO$ contains additional indicators related to the cross-correlation process.

In addition to the individual image files, the algorithm can also produce a statistical output file, if requested in the input settings. This file contains the mean displacement field computed across all processed images and is structured as follows:

```
VARIABLES = "x", "y", "dx", "dy", "dxdx", "dydy", "dxdy", "counter"
```

All output files can be directly visualized using Techplot, which provides powerful tools for contour mapping, vector field representation, and interactive data inspection. Alternatively, the ASCII-formatted files can be imported into MATLAB for further post-processing and quantitative analysis. Dedicated functions were created to read and process the images for this purpose. However, since these ASCII-formatted output files do not represent standard image matrices, they cannot be read directly as images using MATLAB's *imread* function. Depending on the structure of the imported data, the visualization was performed using either *scatter*, for unstructured vector data, or *imagesc*, after reshaping the vectors into a matrix format suitable for display.

In addiction, masks can be applied to cover specific regions of the data or to select areas for more detailed visualization. Manual adjustments are also possible, such as scaling the values for improved contrast or clarity. This approach was also useful for filtering out low-frequency signals, vibrations, or background noise present in the recordings, enabling a cleaner and more accurate analysis of the displacement fields.

5.2 Time-resolved analysis of BOS data

In this section, the frequency analysis of the high-speed BOS images is described. The Power Spectral Density Power Spectral Density (PSD) of the relevant time signals was evaluated using **Welch's method**, a well-established technique that improves the reliability of spectral estimation derived from experimental or numerical data.

The Welch's method improves the classic periodogram approach by introducing three key steps:

1. **Segmentation:** The signal is divided into partially overlapping segments, commonly with 50% overlap. This reduces the variance of the PSD estimate by effectively increasing the number of independent samples.
2. **Windowing:** Each segment is multiplied by a window function, typically Hamming, to reduce spectral leakage caused by sharp discontinuities at the edges of the segments.
3. **Averaging:** The periodogram is computed for each windowed segment using the FFT/DFT. These individual periodograms are then averaged to obtain the final PSD estimate. This averaging process further reduces the variance of the spectral estimate, providing a smoother and more accurate representation of the signal's frequency content.

The frequency resolution is given by:

$$df = \frac{f_s}{N} \tag{5.1}$$

where fs is the sampling frequency and N is the length of the data window. The resulting plot represents the power spectrum, with frequency on the x-axis and magnitude on the y-axis. The lowest resolvable frequency corresponds to a sine wave that completes one full cycle over the length of the data block, while the highest frequency corresponds to a sine wave that completes half a cycle between the first and third data points, i.e., the Nyquist frequency. In practice, the spectrum goes from the lowest frequency determined by the window length to the highest frequency set by the sampling frequency. Increasing the block size improves the frequency resolution; however, using longer segments reduces the number of averaged segments, which can increase the noise in the estimated spectrum. Therefore, a compromise must be made between resolution and spectral smoothness.

The Welch's method was initially applied to the post processed high-speed images. Two approaches were considered for the analysis. In the first approach, only the data corresponding to a single point (specifically, the center of an individual interrogation window from the cross-correlation) was used. In the second approach, the data were averaged over an $n \times n$ nearby windows around a selected point, with n being a variable parameter. This second approach was preferred and ultimately used in the analysis because it improves the results by reducing the influence of local noise and small-scale fluctuations. Averaging over a neighborhood effectively smooths the signal while preserving the main frequency content, yielding a more reliable and representative power spectral density estimate for the region of interest. This provided a first, though limited, indication of the dominant frequency content in the raw measurements. Subsequently, the same spectral analysis framework was applied to the temporal coefficients extracted from the Model Order Reduction technique used in the study.

5.3 Model Order Reduction

When we talk about **Model Order Reduction (MOR)**, we are referring to a family of techniques that aim to reduce the computational complexity of mathematical and physical models while preserving the essential dynamical features of the system. These methods are particularly valuable in fluid dynamics, structural mechanics, and control systems, where full-order models can involve millions of degrees of freedom, leading to prohibitive computational costs for simulations, optimization, or real-time control. MOR techniques provide a way to represent complex systems in a lower-dimensional space while maintaining their physical interpretation.

Generally speaking, MOR approaches can be classified into two main categories: *projection-based* and *data-driven* techniques:

> Projection-based methods rely on the linearization of governing equations and project the high-dimensional system onto a reduced subspace spanned by a limited set of basis functions. Although these methods are mathematically rigorous and effective for linear or weakly nonlinear systems, their extension to highly nonlinear or transient flows can become challenging.

Data-driven methods, on the other hand, exploit experimental or numerical data to extract the dominant coherent structures that govern the system's behavior. These techniques are independent of the explicit governing equations and can therefore be applied even when the underlying physical model is unknown or too complex to handle. Among these, the **Proper Orthogonal Decomposition (POD)** has emerged as one of the most robust and widely used methods in fluid mechanics and aeroacoustics.

5.3.1 Proper Orthogonal Decomposition (POD)

Proper Orthogonal Decomposition is a data-driven model reduction technique that identifies the most energetic spatial modes within a flow field. It decomposes a flow variable, such as velocity or density, into a mean component and a fluctuating part that can be expressed as a linear combination of orthogonal basis functions (modes). Formally, the desired variable field can be expressed as:

$$u(x,t) = \overline{u}(x) + u'(x,t) = \overline{u}(x) + \sum_{j=1}^{M} a_j(t)\, \phi_j(x) \tag{5.2}$$

where $\overline{u}(x)$ is the temporal mean, $\phi_j(x)$ are the spatial modes, and $a_j(t)$ are their corresponding temporal coefficients.

POD is typically implemented through the Singular Value Decomposition (SVD) of a snapshot matrix U, which contains flow field data collected at different time instants:

$$U = \Phi\, \Sigma\, A^T \tag{5.3}$$

The physical interpretation of the POD modes depends critically on how the data matrix U is organized prior to the SVD. To ensure that the extracted modes have a clear spatial and temporal meaning, the matrix is constructed as follows:

- Each **column** of U represents a **snapshot** of the flow field at a given time instant t_k, flattened into a column vector.
- Each **row** of U corresponds to the temporal evolution of a specific spatial location (or measurement point).

If the flow variable $u(x,t)$ is sampled over N_x spatial points and N_t time instants, the resulting data matrix has dimensions:

$$U \in \mathbb{R}^{N_x \times N_t} \tag{5.4}$$

Before performing the decomposition, it is customary to remove the temporal mean from each spatial point so that only the fluctuating component $u'(x,t)$ remains. This centering operation ensures that the first POD mode represents the most energetic coherent structure rather than the mean field itself.

With this convention, the columns of Φ contain the spatial modes $\phi_j(x)$, while the columns of A contain the corresponding temporal coefficients $a_j(t)$. Σ is a diagonal matrix of singular values and represents the relative energy (or variance) of each mode. The singular values in Σ are ranked in descending order, ensuring that the first few modes capture the majority of the system's energy or variance. This formulation ensures that:

- The spatial modes $\phi_j(x)$ describe coherent spatial patterns in the flow field;
- The temporal coefficients $a_j(t)$ describe how the amplitude of each mode evolves over time;
- The singular values σ_j quantify the energy contribution of each mode.

Optimality and Application Context

POD is particularly suitable for analyzing turbulent and unsteady flows, such as the shock-induced separation in a rocket nozzle. Compared to other modal decomposition techniques, POD provides an *optimal low-rank approximation* of the dataset in the least-squares sense [9]. This property is key for noise reduction, as it allows the reconstruction of the scalar field using only a subset of the most dominant modes, effectively filtering out small-scale noise and high-frequency fluctuations (often associated with the higher-order modes).

In the context of supersonic nozzle flows, even tho still novel, POD has been used to reduce both computational and storage time, as well as show that the unsteady jet is dominated by 1. displacement of the shock system caused by back-pressure variations, 2. its oscillation and 3. turbulent mixing within the shear layer [8]. The ability to extract these dominant structures from the quantitative Δx and Δy fields provides a powerful link between flow visualization and the underlying fluid dynamics that generate instability.

Transition to Spectral Analysis

While classical POD is optimal for capturing the spatial energy distribution, the resulting temporal coefficients $a_j(t)$ are not necessarily ordered by frequency, nor do they perfectly isolate single-frequency phenomena. For flows characterized by distinct frequencies and complex instability mechanisms methods that incorporate frequency filtering directly into the decomposition are often employed.

The Spectral Proper Orthogonal Decomposition (SPOD) [10] or techniques like Dynamic Mode Decomposition (DMD) are rigorous tools used in the literature to decompose the flow into modes that are orthogonal in both space and frequency. For instance, studies on unsteady nozzle flows have successfully used these spectral methods to isolate the energy associated with the global shock oscillation (low frequency) from that of the Kelvin-Helmholtz instability (higher frequency) in the shear layer [8].

Capitolo 6

Results

In this Chapter, the outcome of the current research is presented. A general reconstruction of the flow instantaneous field is performed and showed in Figure 6.1 to evaluate the spatial detail captured by the BOS technique and to assess its ability to resolve the main flow structures of the over-expanded jet. This comparison serves as a basis for the subsequent sections. The results are organized as follows: First, the performance of the reconstruction method is evaluated. Second, the main flow features of the nozzle exhaust plume at different NPRs are presented through the analysis of the mean and instantaneous BOS images. Then, the coherent structures in the nozzle jet flow are discussed through POD analysis of the displacement fields. Lastly, a discussion about the nozzle asymmetries is given.

6.1 Spatial resolution analysis

As known from previous publications [31], Toepler's system, which uses collimated light and a knife-edge cutoff, is able to produce real time images that are highly sensitive to refractive index gradients and have high SNR. However, the system requires precise alignment and an equipment that can become expensive both in terms of cost and required space. Background Oriented Schlieren (BOS) has been proven to be a more flexible and accessible alternative [11, 28]. It can achieve larger Field Of View and is based only on two sets of images and a known background pattern. In contrast, the processing method can introduce loss of spatial resolution or artifacts, depending on the chosen parameters and background characteristics. Additional errors may also arise from background motion or air fluctuations in the test environment. Despite these challenges, the BOS technique offers significant advantages in terms of simplicity, cost efficiency, and scalability.

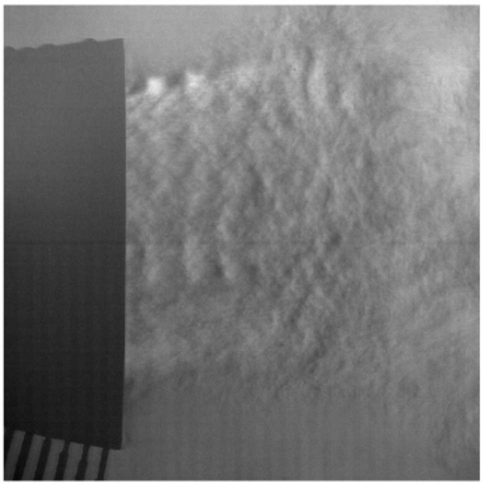

(a) Conventional Shlieren field

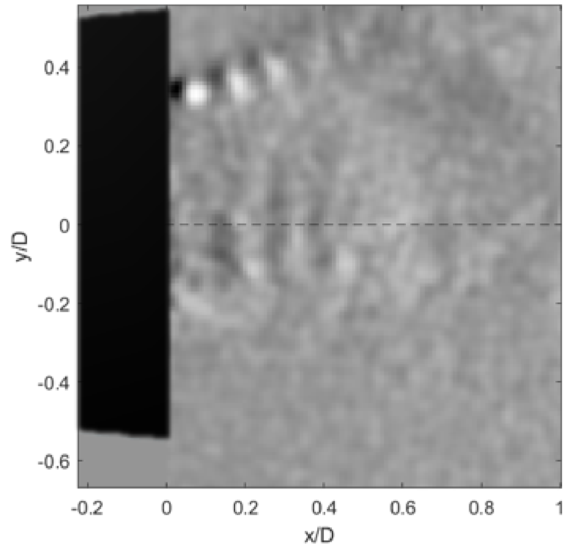

(b) Background Oriented Schlieren field

Figura 6.1: Comparison of instantaneous flow field between conventional schlieren (horizontal knife edge) and corresponding density gradient field from BOS.

Looking at Figure 6.1, an observation can be made that is consistent with other studies in the literature [32]: one can see that the reconstructed BOS fields appear slightly blurred when compared with the corresponding classic Schlieren images. This reduction in spatial resolution is inherent to the technique, as the camera must be focused on the background rather than on the flow region.

As seen in Chapter 3, the two main parameters that affects the spatial resolution of the BOS reconstructed fields are:

- The **geometric blur**, determined by the optical configuration and quantified by the Circle of Confusion (CoC)

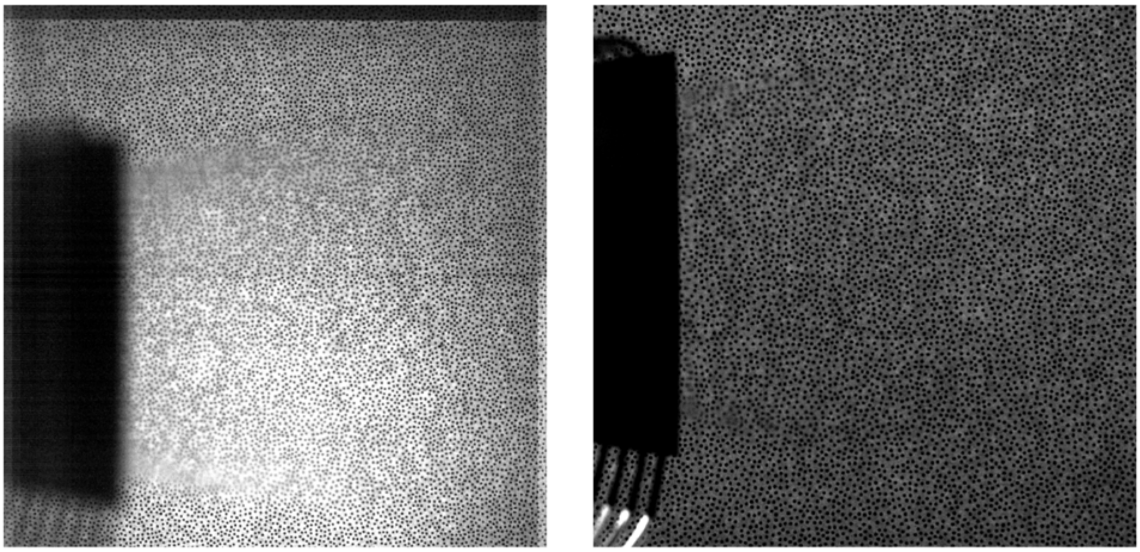

(a) First reference image

(b) Improved reference images

Figura 6.2: Reference flow-on images before and after the improved setup.

- The **processing algorithm**, particularly the **size of the Interrogation Window (IW)** used in the cross-correlation.

According to equation 3.9, the CoC depends on the aperture diameter, the focal length, and the distance between the object plane and the focal plane. Since only a limited set of lenses was available, different combinations of $f_{\#}$ and Z_D were tested. As discussed in Chapter 4, the density gradients generated in our experiments were sufficiently strong that sensitivity played only a minor role compared to image blur. Although the literature indicates that the sensitivity of the BOS technique increases with the distance between the object and the background [33], and therefore the object is typically positioned approximately midway between the camera and the background pattern, from the first to the second and final experimental campaign the background was placed as close as possible to the test section, and the aperture was reduced as much as possible given the available light. Z_D was reduced from $70cm$ to $25cm$ and the aperture was reduced from $f/8$ to $f/16$. This configuration significantly decreased the geometric blur, leading to sharper dot images and more detailed displacement fields. A comparison of the two raw images is shown in Figure 6.2. A close-up of the background pattern is also reported in Figure 6.3. Regarding the second factor influencing spatial resolution, one can observe that larger Interrogation Window sizes yield smoother displacement fields with higher Signal-to-Noise Rateo, as the correlation peak becomes stronger and more stable. At the same time, reducing the Interrogation Window size allows smaller flow structures to be resolved, but increases noise, reduces the number of valid vectors, and increases computational time.

A parametric analysis was therefore carried out using the **BOSproc Tool** to identi-

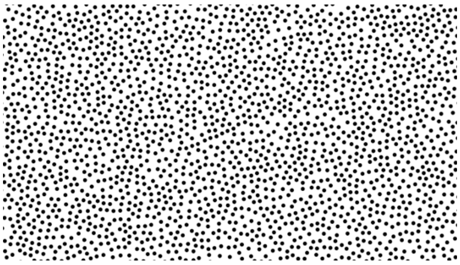

Figura 6.3: Close-up of the speckle background pattern

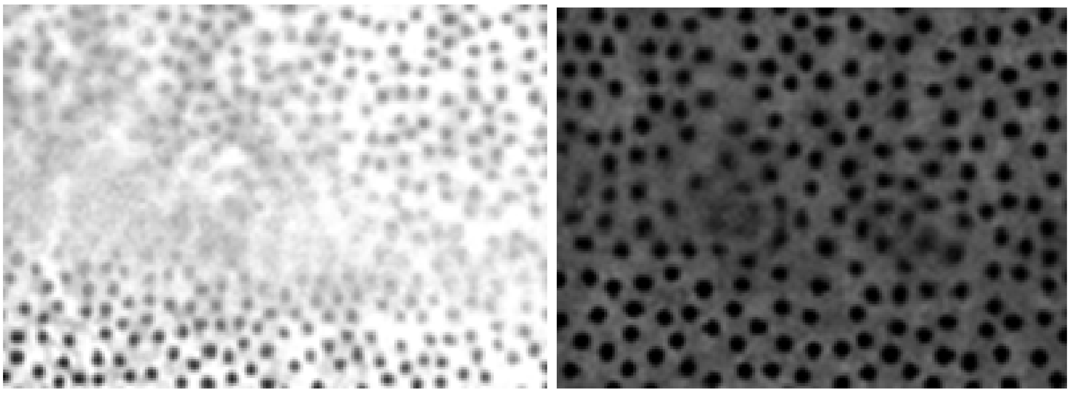

(a) First reference image **(b)** Improved reference images

Figura 6.4: Close up flow-on images before and after the improved setup.

fy the optimal IW size. The code allows the user to load a pair of raw and reference images and directly compare them in real time. For any selected point within the overlapping region, the corresponding three-dimensional cross-correlation surface can be visualized, showing how the shape and sharpness of the correlation peak evolve as window size and position are changed. Figure 6.5 shows the evolution of the correlation peak as a function of IW size. Using larger windows yield smoother displacement fields with higher SNR, as the correlation peak becomes stronger and more stable, leading to greater robustness and accuracy in the final displacement vector, while reducing the IW size allows smaller flow structures to be resolved, but increases noise, which compromises the accuracy of the displacement measurement, reduces the number of valid vectors, and increases computational time. An Interrogation Window of 31×31 pixels was selected as the best compromise, providing a clear and well-defined correlation peak while maintaining an acceptable SNR. To further assess the influence of the IW size on the reconstructed flow field, the vertical displacement profiles dy were extracted along the vertical centerline of the measurement domain for each configuration. The comparison, shown in Figure 6.6, illustrates that larger windows produce smoother profiles but fail to capture smaller features of the flow, whereas smaller windows shows high noise and non-physical displacement. Despite these variations, within the $[21 - 41]$ range, the main displacement trends remain consistent across all cases, confirming that the underlying flow structures are correctly identified.

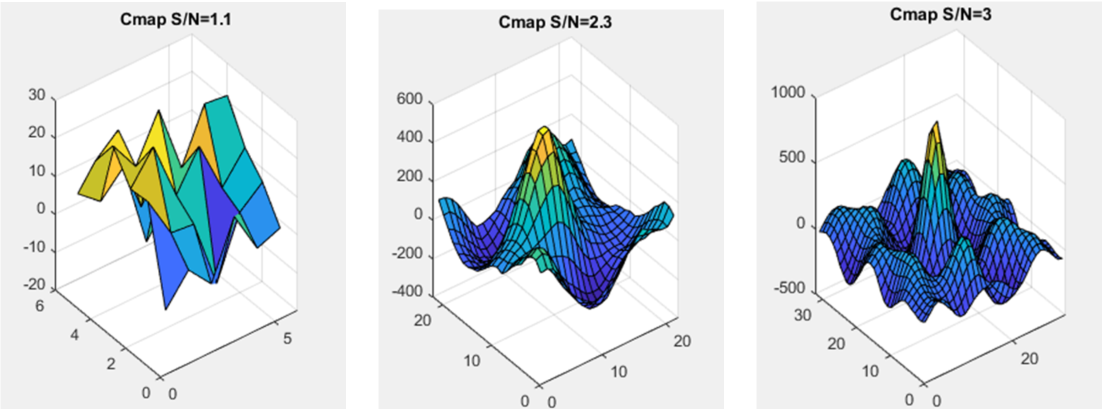

(a) IW size of 5 × 5 pixel **(b)** IW size of 21 × 21 pixel **(c)** IW size of 31 × 31 pixel

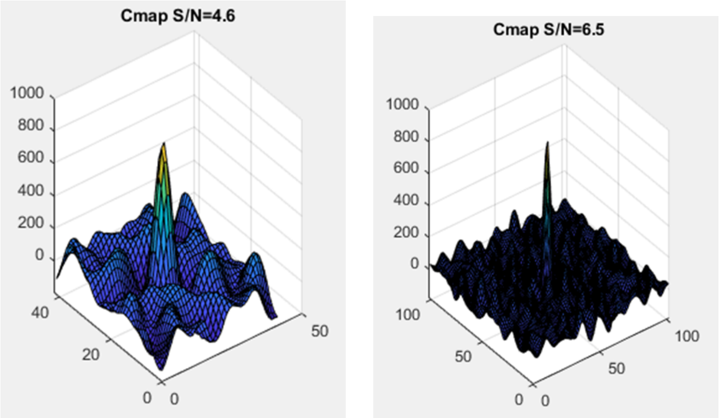

(d) IW size of 41 × 41 pixel **(e)** IW size of 101 × 101 pixel

Figura 6.5: Different cross-correlation peaks for different window sizes

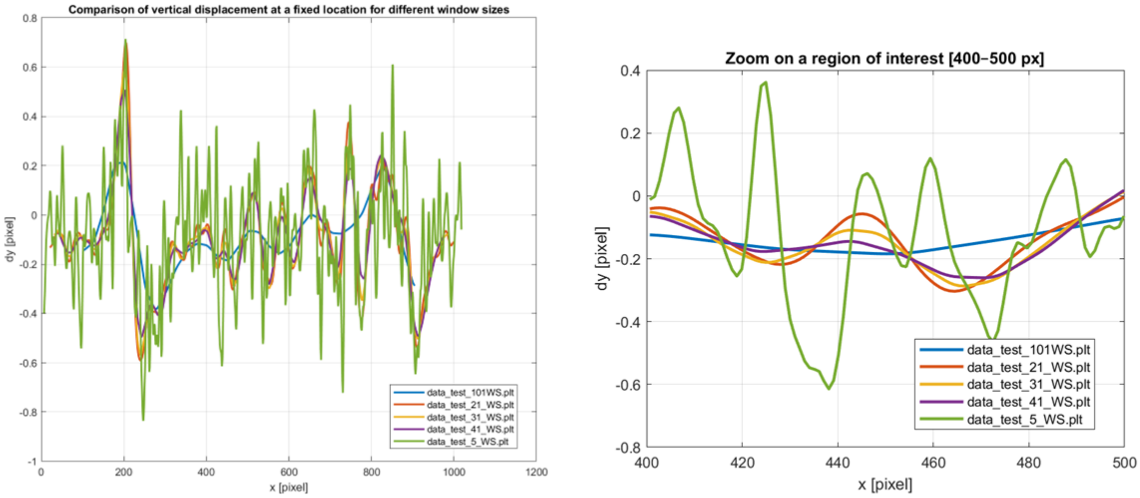

Figura 6.6: Vertical displacement at a fixed location for different window sizes

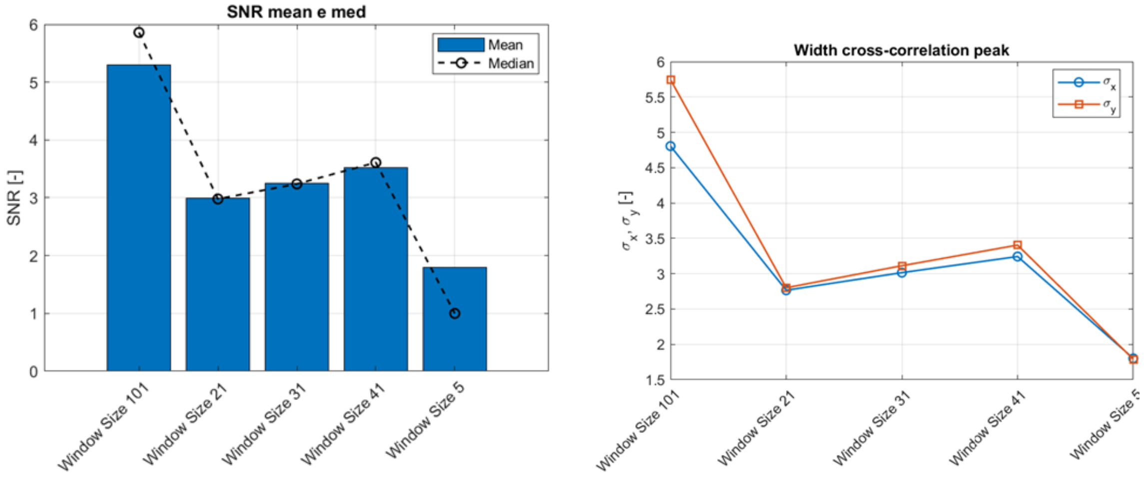

Figura 6.7: Mean and Median SNR and CC peaks for different IW sizes

6.2 BOS displacement visualizations

In the classical Toepler's Schlieren technique, light rays passing through regions of varying density are refracted toward or away from the knife edge. The orientation of the knife determines which component of the refractive index gradient is visualized: for example, a vertically oriented knife blocks light deflected in the vertical direction, making the system sensitive to horizontal density gradients $\delta n/\delta x$. As a consequence, the Schlieren images represent only the component of the density gradient field perpendicular to the knife orientation. Furthermore, the interpretation of bright and dark regions depends on the direction in which the knife is inserted.

In contrast, BOS does not rely on a knife edge and therefore does not suffer from such directional ambiguity. The technique measures the apparent displacement of a background pattern induced by refractive index gradients, providing both horizontal and vertical components of the displacement field simultaneously. Depending on the chosen colormap, positive and negative displacements correspond to rays deflected in opposite directions. The transition zones between bright and dark regions in these maps identify areas of strong density gradients.

These observations form the basis for the following analysis of the Free Shock Separation and Restricted Shock Separation regimes. In the present work, both displacement components are analyzed to identify regions of compression and expansion in the flow field.

Free Shock Separation

In the FSS regime the flow inside the over-expanded nozzle separates from the wall remains detached all the way to the exit, forming a free jet beyond the separation location. This state is characterized by a large and global separation region [27]. The 16 NPR case was selected as a reference case for this regime.

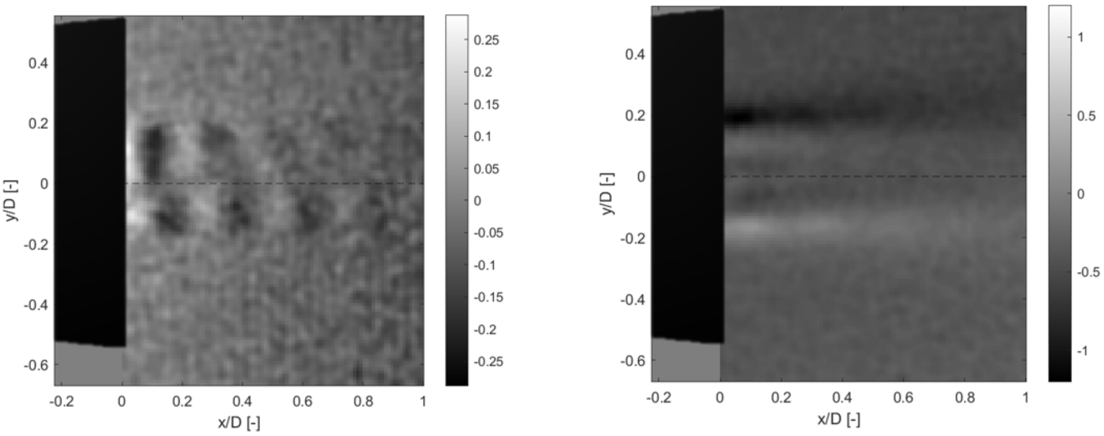

(a) Horizontal displacement field (*dx*) **(b)** Vertical displacement field (*dy*)

Figura 6.8: Reconstructed horizontal and vertical displacement for FSS at 16 NPR.

Figure 6.8a shows the reconstructed horizontal displacement field. One can clearly see that alternating light and dark areas appear downstream of the internal shock. These correspond to consecutive regions of positive and negative displacement, indicating areas where the refracted light rays are bent in opposite directions. The alternation becomes progressively less distinct as the distance from the nozzle exit increases, suggesting that the refractive index gradients weaken and the flow gradually transitions to a more uniform jet. This pattern corresponds physically to a sequence of compression and expansion waves within the separated jet. Immediately after the shock, the sudden increase in pressure produces a strong local density gradient followed by a gradual expansion of the flow. The decreasing intensity of these bands further downstream is consistent with the weakening of these wave interactions and the mixing of the free jet with the ambient. The overall pattern is slightly tilted with respect to the horizontal direction, revealing an asymmetry in the separation process. In particular, the lower part of the displacement field appears slightly ahead of the upper part, suggesting that the separation point on the lower side of the nozzle occurs further downstream than the upper side.

Figure 6.8b represents the reconstructed vertical displacement field. Two clearly defined regions of opposite sign can be identified: a bright (positive) band near the lower part and a dark (negative) band near the upper part of the jet. Between these two bands, there is a relatively uniform region, with no distinct internal structures visible. This smooth distribution suggests that the light rays are deflected from both sides toward the center region of the jet. The two opposite-sign bands are most likely associated with the upper and lower shear layers that develop at the boundaries of the separated jet. These layers define the interface between the high-speed jet core and the recirculating outer flow. The lack of distinct internal structures within the core implies that the strongest vertical refractive-index gradients are concentrated at the shear-layer interfaces. However, faint streaks can be observed that mirror the orientation of the main upper and lower bands. These features are not believed to correspond to distinct flow structures but rather result from the line-of-sight integration technique [12], see Appendix A.2.2. The three-dimensional nature of the separated flow causes the light rays to travel regions with varying density gradients at different depths, producing weak secondary displacements that mirror the primary shear layers behavior in the reconstructed displacement field.

The measured displacement fields, representing the line-of-sight projection of the refractive index gradient are used to reconstruct the flow's line of sight density structure. Figure 6.9 presents the reconstructed density field, the magnitude of the density gradient, and the Laplacian for the FSS reference case.

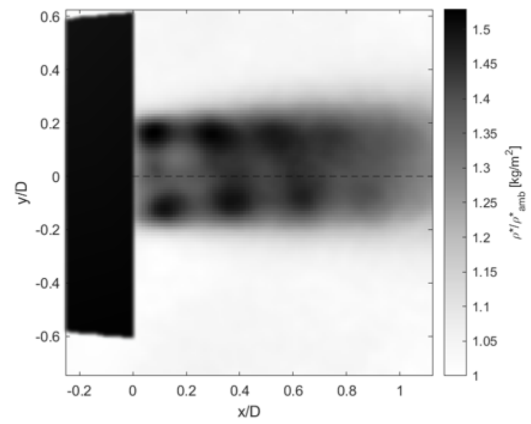

(a) Reconstructed projected density field

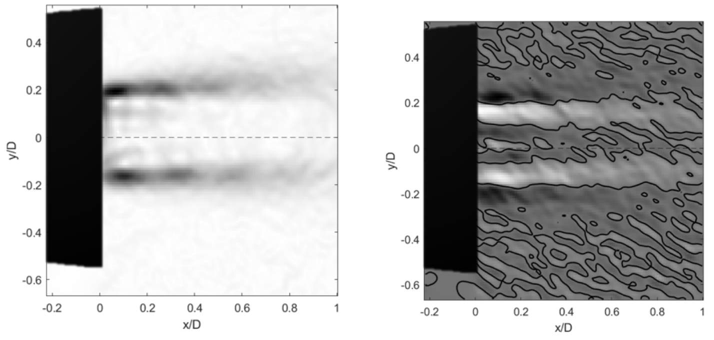

(b) Magnitude of the density gradient

(c) Laplacian of the density gradient

Figura 6.9: Reconstructed flow density structures for the FSS reference case

Immediately downstream of the nozzle exit, the field in Figure 6.9a exhibits a sharp local density increase. This feature is consistent with the sudden pressure jump associated with the internal shock. Inside this core, the field clearly reveals the wave structure as a sequence of high-density (compression) and low-density (expansion) cells, fully coherent with the alternating bands identified in the *dx* field. Following the initial compression, the field shows progressively diffused darker and brighter areas, mirroring the sequence of expansion and re-compression waves typical of an over-expanded jet adapting to the ambient air. The reconstructed field maintains the slight forward tilt observed in horizontal displacement. The magnitude of the density gradient, Figure 6.9b provides a visualization of the interfaces where the refractive index changes most rapidly. This field is dominated by two distinct high-intensity bands that originate at the nozzle exit. These bands represent the upper and lower shear layers that separate the high-speed jet core from the low-speed recirculating outer flow. Inside these two bands the field shows structures coherent with the sequence seen in the density field. The intensity of all these features gradually decreases downstream. The Laplacian of the projected density field in Figure 6.9c serves as a second-order spatial visualization, used to visualize compression/expansion areas and vortical structures.

Restricted Shock Separation

In the RSS regime, the flow inside the over-expanded nozzle reattaches before reaching the nozzle exit, forming a separation bubble. This recirculation zone is bounded by the separated shear layer and the nozzle wall, with the flow reattaching downstream and continuing toward the exit as an attached boundary layer. The reattachment process generates a complex shock structure that interacts with the external jet [1, 22]. The 24 NPR case was selected as a reference case for this regime.

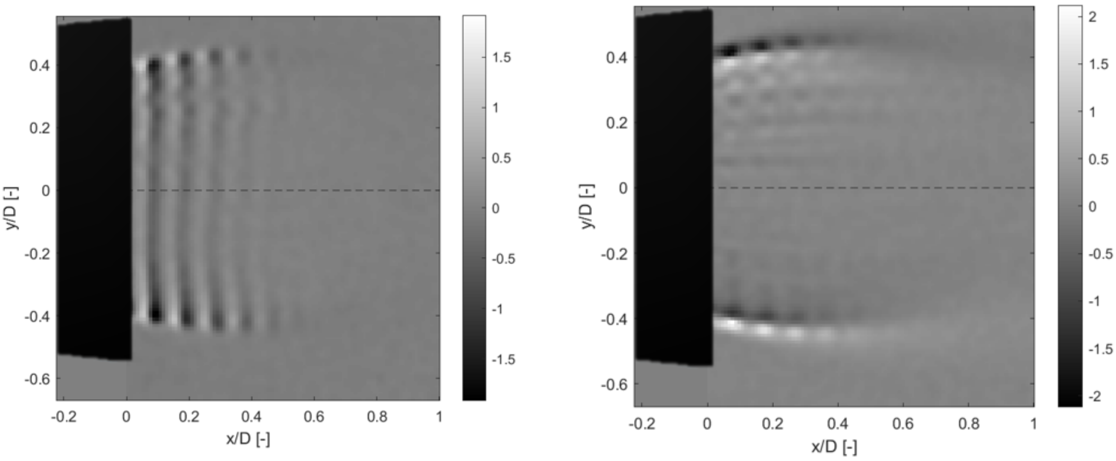

(a) Horizontal displacement field (dx) **(b)** Vertical displacement field (dy)

Figura 6.10: Reconstructed horizontal and vertical displacement for RSS at 24 NPR.

Figure 6.10a shows a series of alternating dark and light vertical bands. These bands appear relatively well-defined and evenly spaced near the nozzle exit, maintaining their vertical orientation and extending into the jet. These bands are most clear in the first half of the visible domain and become progressively less distinct further downstream. Along the jet boundary, one can also observe the presence of a fine internal cellular structure. Physically, since the alternating vertical bands correspond to regions of positive and negative horizontal displacement, one can clearly see that the light rays are deflected in opposite horizontal directions. This pattern is consistent with a series of compression and expansion areas. The vertical orientation of the bands suggests that these waves propagate primarily in the streamwise direction with relatively sharp gradients. As the jet evolves and mixes with the ambient, the wave system gradually dissipates, and this is represented by the weakening of the pattern as we move downstream.

In Figure 6.10b two distinct regions of opposite sign can be seen. These regions originate near the nozzle wall with a relatively narrow vertical extent and expand progressively as they extend downstream. Within each of these bands, the presence of positive and negative displacement can be observed. Similarly to the horizontal displacement field, one can also see an internal cell-like structure within the single black and white bands. These cellular patterns are most evident in the near-nozzle region and become progressively less distinct downstream. Between these two opposite-sign regions, there is a central zone with relatively neutral gray tones, suggesting minimal vertical displacement. Physically, the two wedge-shaped bands correspond to the upper and lower shear layers that bound the jet. These shear layers create interfaces where the density changes rapidly in the vertical direction, causing the observed light deflection. The central region with minimal vertical displacement corresponds to the jet core, where vertical density gradients are weak and the flow is more uniform.

The reconstructed flow density structures are shown in Figure 6.11.

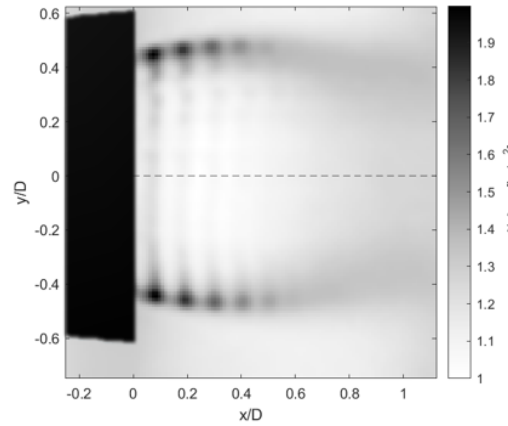

(a) Reconstructed projected density field

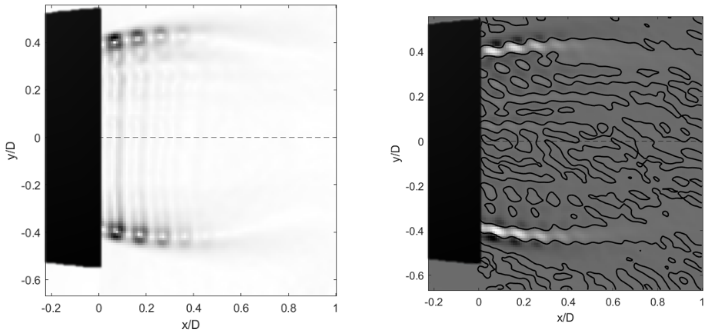

(b) Magnitude of the density gradient

(c) Laplacian of the density gradient

Figura 6.11: Reconstructed flow density structures for the RSS reference case

The field in Figure 6.11a is characterized by a well-organized sequence of alternating high-density (compression, dark regions) and low-density (expansion, light regions) cells. This highly regular pattern maintains its vertical orientation throughout the whole domain. This structure is spatially contained within the boundaries defined by the intense upper and lower bands of the *dy* field. The cell-like internal pattern within these bands arise from the interaction between the reattached flow and the nozzle wall downstream of the separation bubble. This interaction generates a series of compression and expansion waves that propagate through the flow. Once again the pattern gradually weakens and diffuses downstream, consistent with energy dissipation as the jet mixes with the ambient air. The field representing the magnitude of the density gradient, Figure 6.11b, as in the previous regime, is bounded by two distinct bands corresponding to the upper and lower shear layers. These bands are visually thicker and more diffuse in their downstream development compared to the FSS. This feature is also more constrained and intense near the wall.

6.3 POD modal analysis

This section presents an in-depth analysis of the Proper Orthogonal Decomposition modes derived from displacement fields. The technique allows the decomposition of complex flow phenomena into a set of orthogonal modes, each representing a distinct spatial and temporal characteristic of the flow [9]. The modes are ranked by the amount of kinetic energy they capture; in this analysis, the first six modes are chosen as a reference case of study. The first 200 modes collectively reach 80% of the total energy, confirming the ability of the lower-order modal reconstruction to capture the main features of the flow. The visual representation of the modes is done by using a divergent colormap to clearly distinguish between positive (red) and negative (blue) displacement values, with a neutral color (white) representing the zero-displacement.

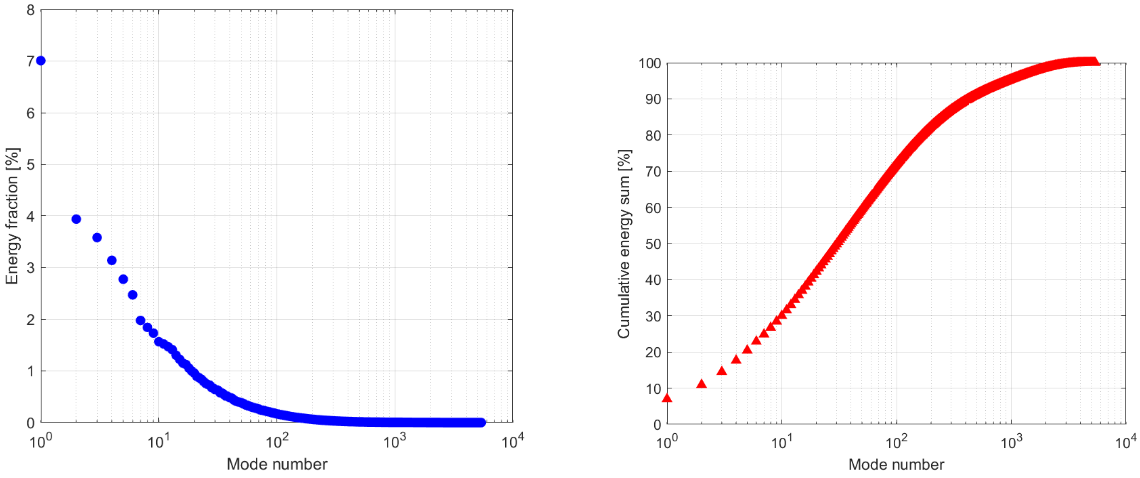

(a) Modal energy distribution **(b)** Cumulative energy content

Figura 6.12: Energy distribution of the POD modes for the FSS regime at 16 NPR.

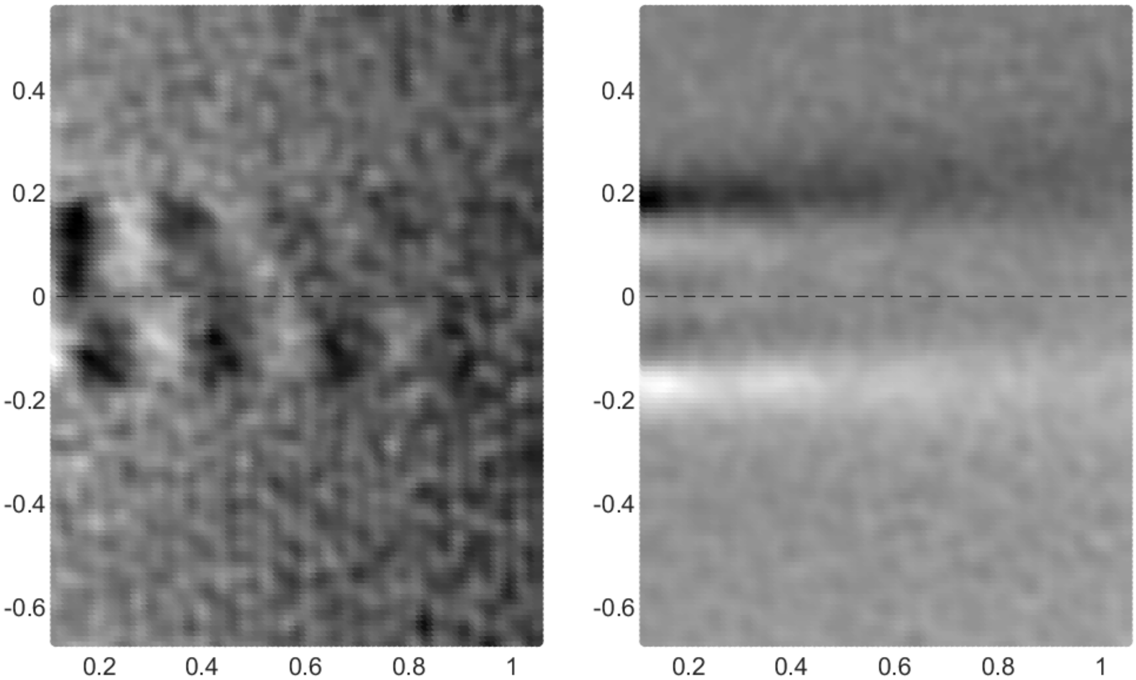

(a) Horizontal displacement field (dx) **(b)** Vertical displacement field (dy)

Figura 6.13: Reconstructed horizontal and vertical displacement fields for the FSS regime at 16 NPR, obtained using the first 200 POD modes.

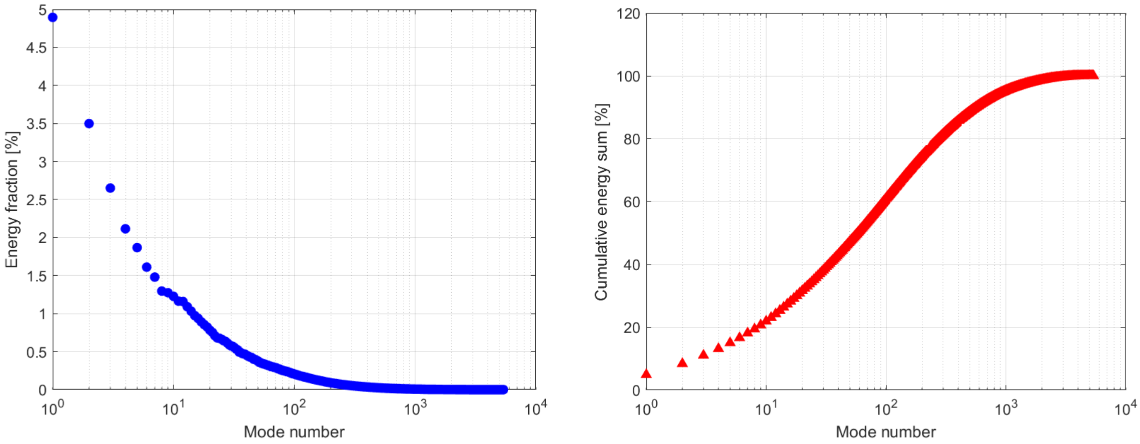

(a) Modal energy distribution **(b)** Cumulative energy content

Figura 6.14: Energy distribution of the POD modes for the RSS regime at 24 NPR.

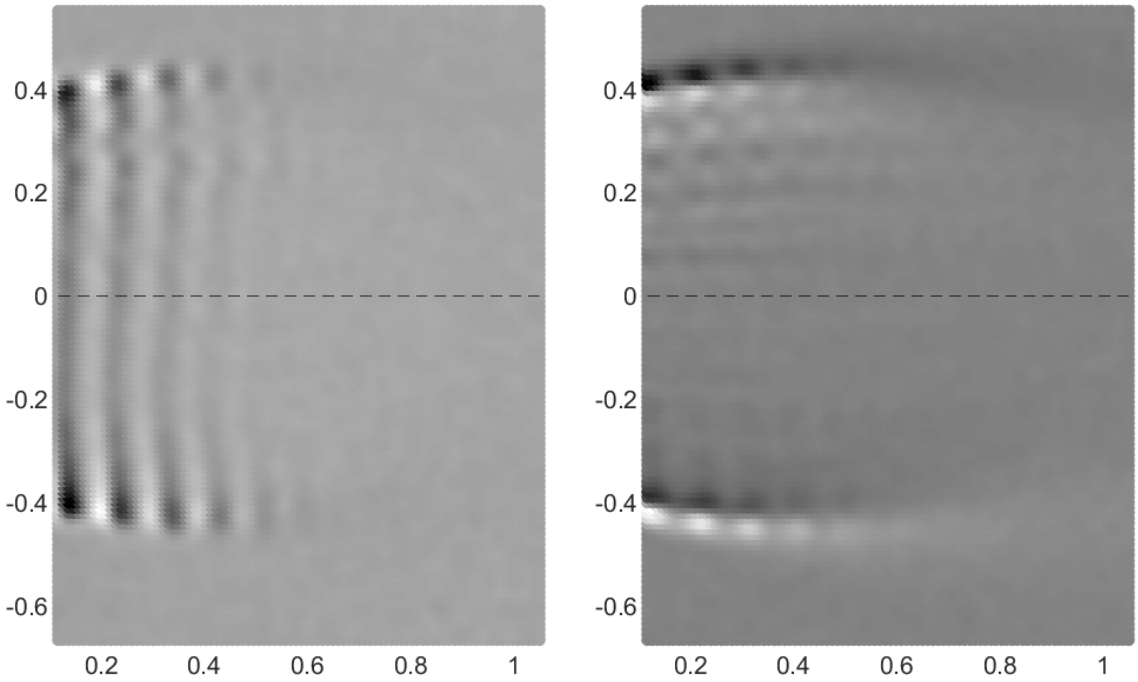

(a) Horizontal displacement field (dx) **(b)** Vertical displacement field (dy)

Figura 6.15: Reconstructed horizontal and vertical displacement fields for the RSS regime at 24 NPR, obtained using the first 200 POD modes.

Free Shock Separation

Figure 6.16 shows the first six modes for the vertical displacement. Observing Mode 1, one can clearly see that the structure above and below the horizontal axis exhibits symmetry in shape. If a line is drawn along the axis, the upper and lower parts mirror each other, suggesting they respond in the same manner relative to this axis. However, the intensity (magnitude of displacement) appears to be different between the upper and lower regions. This symmetric nature of the mode suggests a coherent, large-scale oscillation of the entire exhaust plume. When this mode is added to the mean flow, the entire structure moves collectively up and down, creating the characteristic flapping motion of the jet. The lower intensity in the bottom part could hint at an inherent asymmetry in the separation process, consistent with the observation from the vertical displacement field. This dominant flapping motion is a well-documented characteristic of overexpanded and separated jets [1]. Mode 2 presents a structural pattern similar to Mode 1, but the structures in the upper and lower parts are now opposite in sign. This opposition suggests a contrasting behavior between the two regions. When this mode is added to the mean field, it no longer resembles a coherent "flapping" but rather a "pulsating motion" of the flow. This implies that the upper and lower sections move out of phase, leading to an expansion and contraction-like behavior of the jet [34]. As we progress to higher modes, their significance diminishes. They exhibit progressively smaller amplitudes and higher-order structures, resembling combinations or finer details of the more dominant initial modes. They are generally considered to contribute less significantly to the overall flow dynamics.

Figure 6.17 shows the first six modes for the horizontal displacement. These modes exhibit distinct alternating patterns of positive and negative regions along the streamwise direction. These structures are most likely associated with the consecutive regions of compression and expansion that arise from the interaction between the internal shock and the separated jet boundaries. A key observation is that the magnitude of these horizontal modes is lower compared to the dy displacement modes, which suggests that the most intense and energetic flow activity is focused on the vertical plane. As we move downstream in the flow and into higher-order modes the intensity of these patterns decrease.

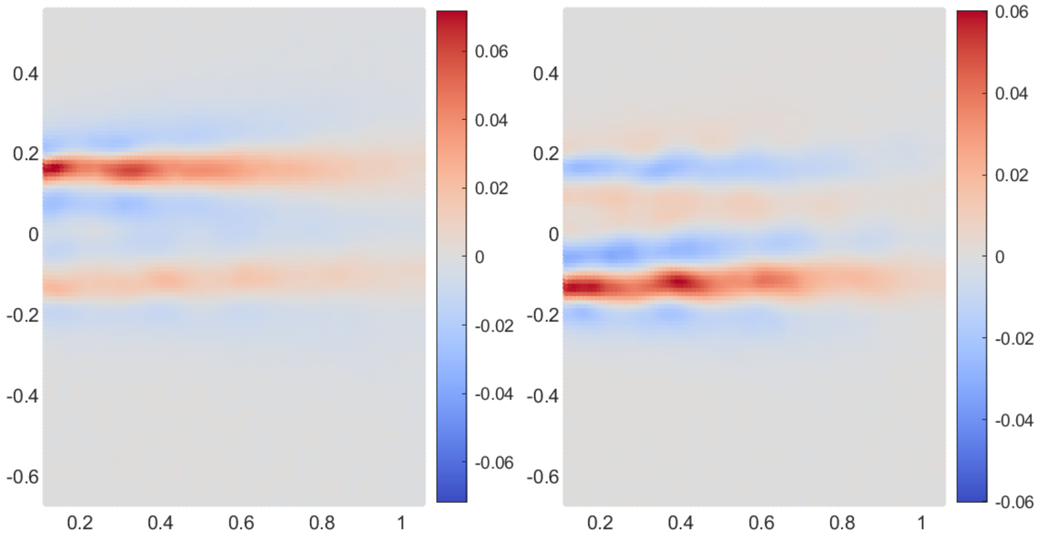

(a) Mode 1 **(b)** Mode 2

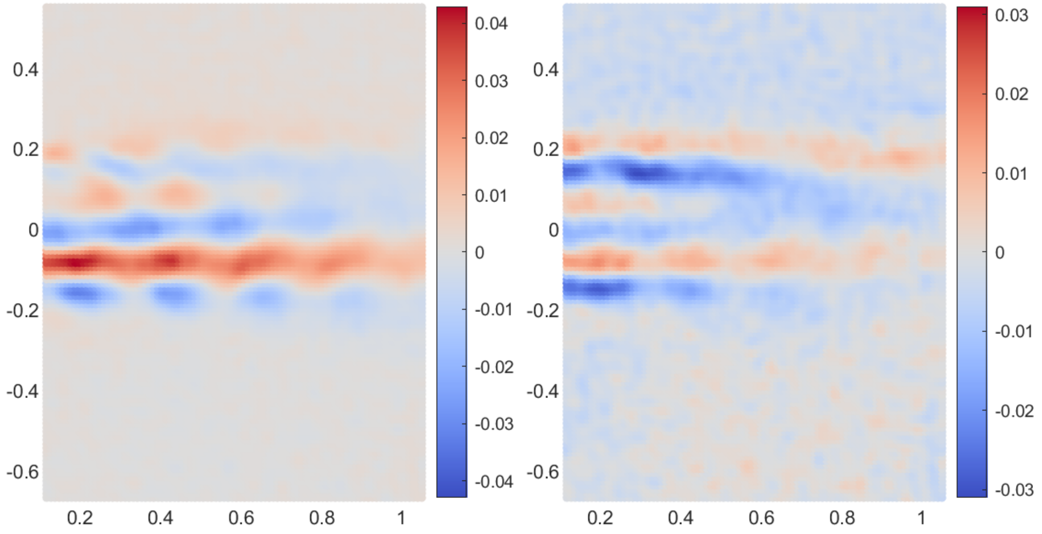

(c) Mode 3 **(d)** Mode 4

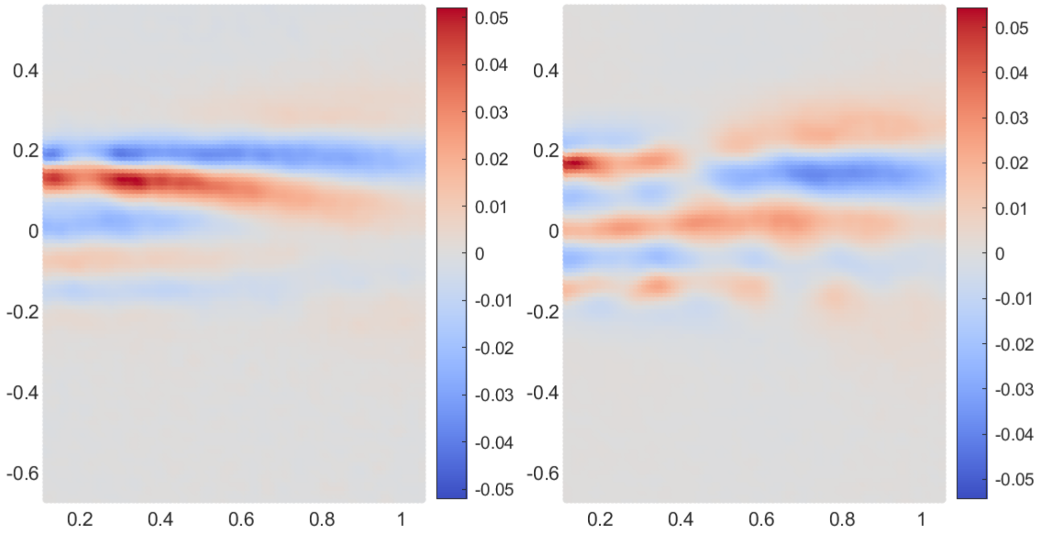

(e) Mode 5 **(f)** Mode 6

Figura 6.16: First six POD modes from the vertical displacement field for the FSS reference case

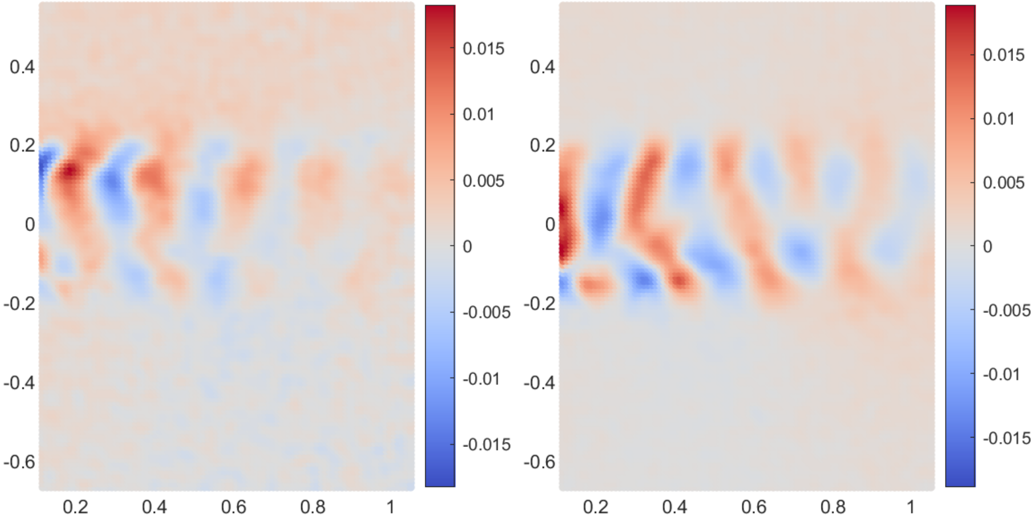

(a) Mode 1 **(b)** Mode 2

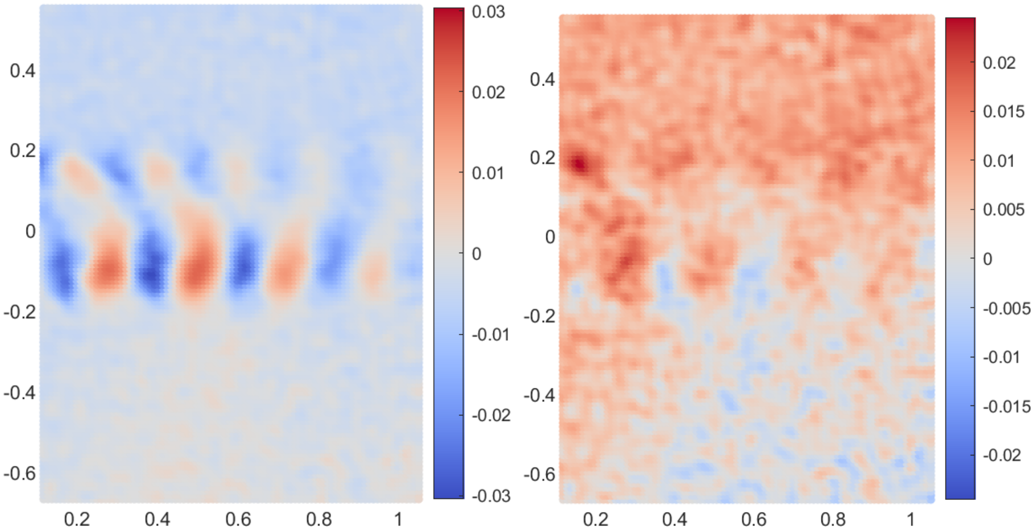

(c) Mode 3 **(d)** Mode 4

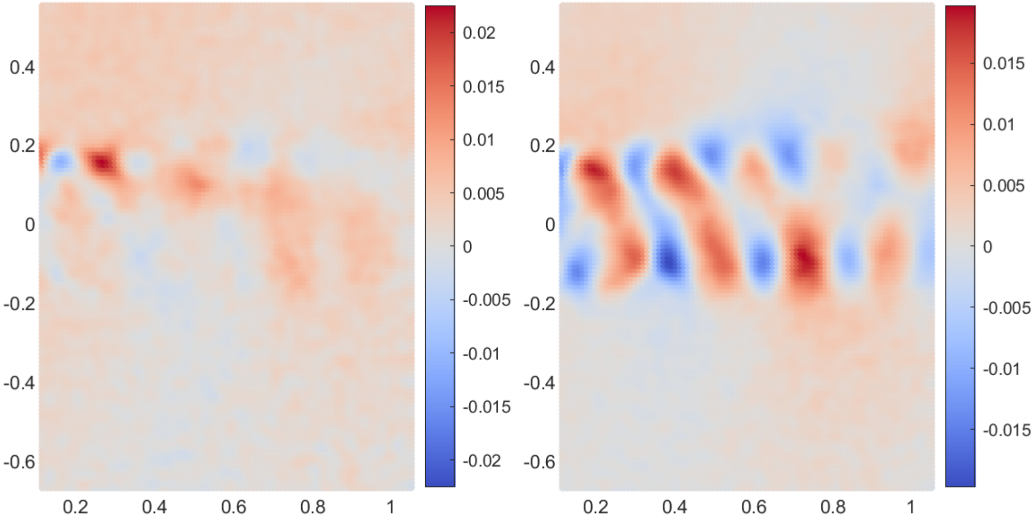

(e) Mode 5 **(f)** Mode 6

Figura 6.17: First six POD modes from the horizontal displacement field for the FSS reference case

Restricted Shock Separation

In RSS, the major activity is focused on the horizontal displacement fields, suggesting that the unsteadiness is now driven by the axial movement of the flow rather than the vertical flapping/breathing motion. The instability is now reflecting the presence of the small, confined recirculation bubble close to the wall. This confinement means the energy is not released into large, coherent structures that dominate the entire jet cross-section, unlike during FSS, but rather a high-energy localized structure along the nozzle walls.

The dx modes capture the axial movement of the separation mechanism, which refers to the highly unsteady interaction between the shock foot and the boundary layer. Mode 1 shows intense activity along the lower wall, while Mode 2 figures a mirrored in structure but opposite in sign behavior. This energetic oscillation corresponds to the *Streamwise Oscillation* or *Axial Sloshing* of the confined recirculation bubble and its associated shock foot [1].

The dy modes capture the radial movement of the separation mechanism, which affects the confined bubble. Mode 1 and 2 are mirrored in structure along the jet axis. Their patterns appears to be coherent, suggesting that both sides of the shear layer are responding simultaneously and symmetrically. This symmetric oscillation may corresponds to the *Radial Pulsation* or *Thickness Modulation* of the recirculation bubble.

As we go into higher-order modes for both vertical and horizontal displacements, the spatial patterns no longer represent the confined recirculation bubble. Instead, they exhibit structures that cover the entire section of the jet. The presence of these full-field modes indicates that even under RSS conditions, the localized primary instability eventually seeds the development of global, higher-frequency turbulent structures

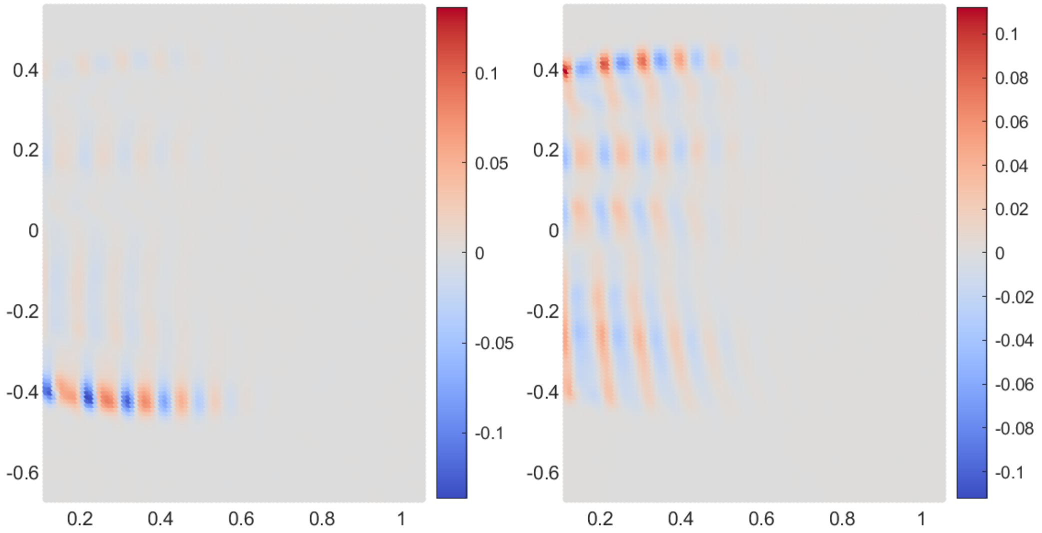

(a) Mode 1 **(b)** Mode 2

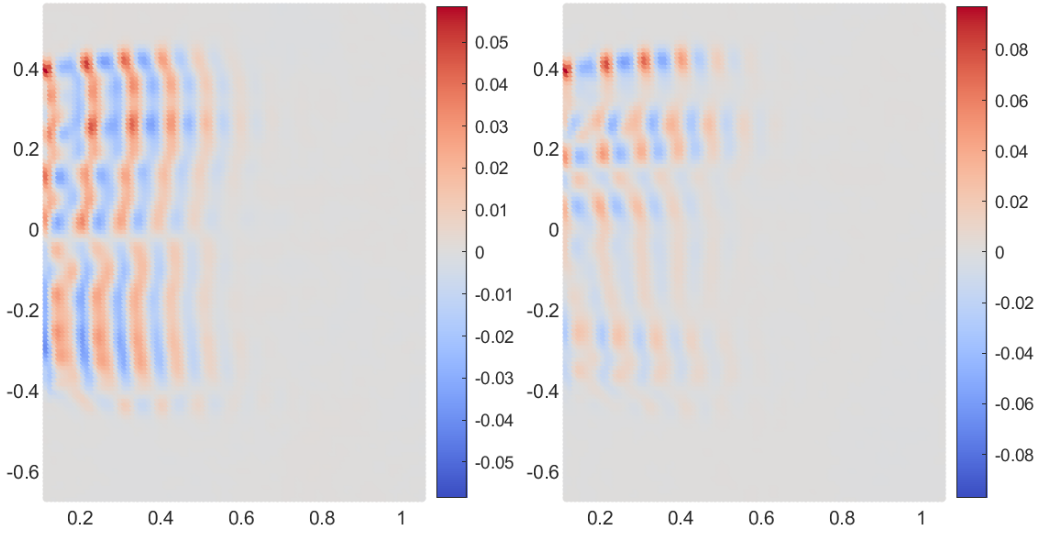

(c) Mode 3 **(d)** Mode 4

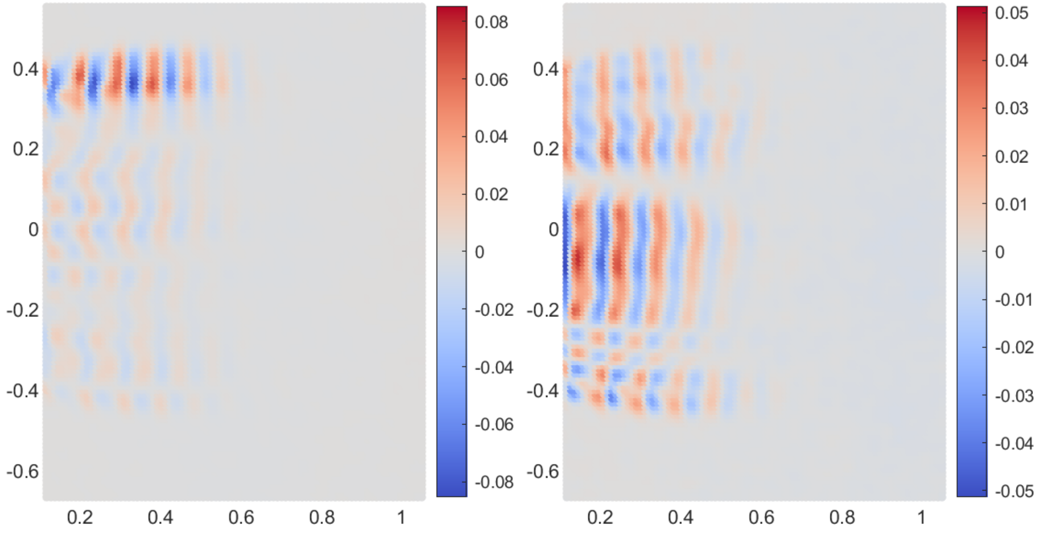

(e) Mode 5 **(f)** Mode 6

Figura 6.18: First six POD modes from the horizontal displacement field for the RSS reference case

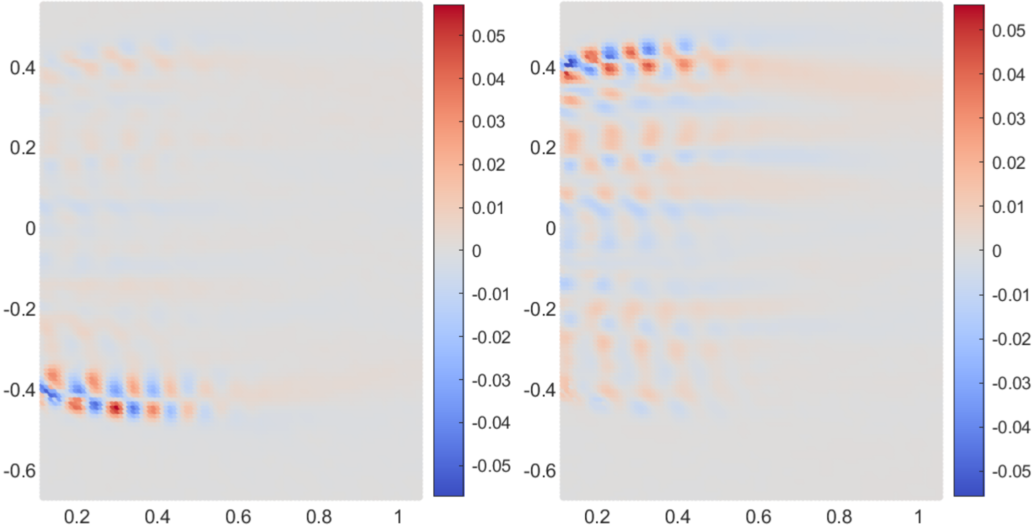

(a) Mode 1 **(b)** Mode 2

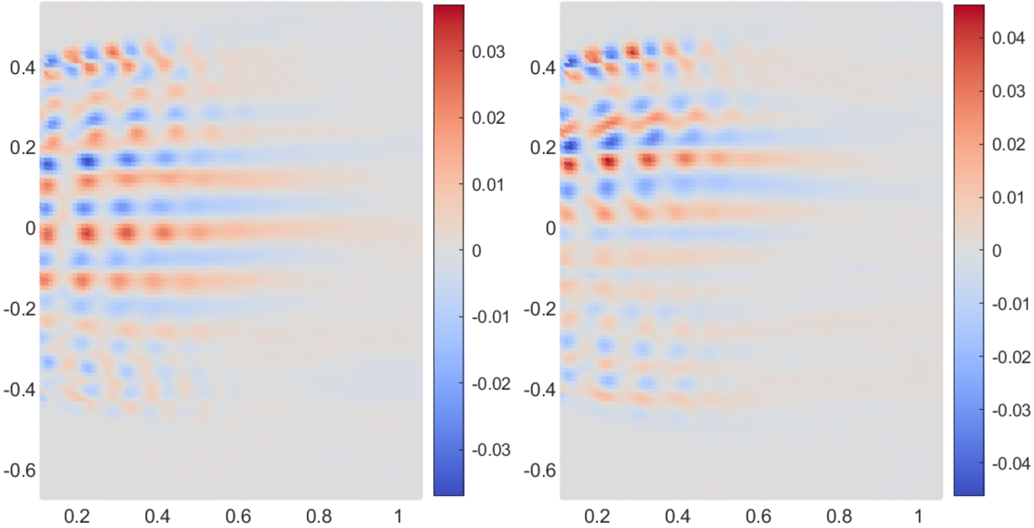

(c) Mode 3 **(d)** Mode 4

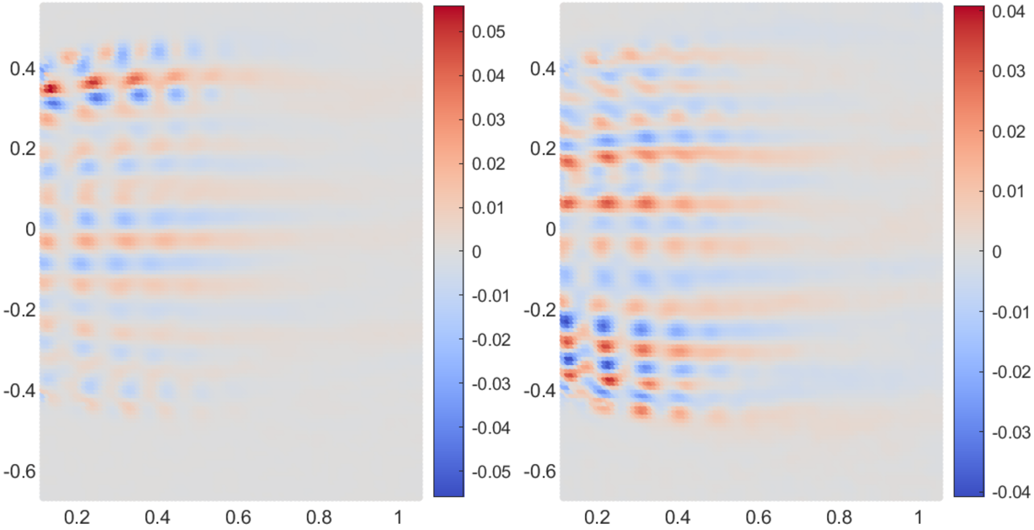

(e) Mode 5 **(f)** Mode 6

Figura 6.19: First six POD modes from the vertical displacement field for the RSS reference case

6.4 Frequency analysis

A spectral analysis was conducted directly on the raw displacement fields $\Delta x, \Delta y$ from the HRBOS dataset. Analyzing both a single point and an $n \times n$ window, no particular behavior or information was found, see Appendix B. Due to this absence of a global, low-frequency signal in the raw data, the POD technique was used not solely as a tool for dimensional reduction, but also as an optimal spatial filter. This filtering is essential because it allows us not only to discuss the spatial content of the flow but also to exanimate the frequency content of the dominant coherent structures.

The spectral analysis of the temporal POD coefficients of the first 10 modes for the Free Shock Separation case is reported in Figure 6.20. An additional detailed view of the first two modes only is also provided in Figure 6.21. In the FSS regime, the first mode exhibits a first, distinct and well-defined spectral peak at approximately 480 Hz, followed by four other peaks that represent the harmonics, at integer multiples, of this fundamental frequency ($\approx$ 960, 1440, and 1920 Hz). This harmonic structure strongly suggests the presence of a periodic and coherent oscillation, associated with the large-scale, low-frequency phenomenon. This is consistent with the global "flapping" motion previously identified in the spatial modes. The second mode shows a very similar spectral signature, with peaks occurring at the same frequencies as in the first mode. Although POD modes are orthogonal by mathematical construction, this coincidence indicates that both modes are driven by the same physical mechanism, representing different spatial manifestations of the same unsteady process. In addition to the harmonic series, the first mode displays a secondary isolated peak near 700 Hz, which does not align with the main harmonic structure and is not observed in the second mode. This component may result from nonlinear coupling between the primary flapping motion and smaller-scale turbulent activity.

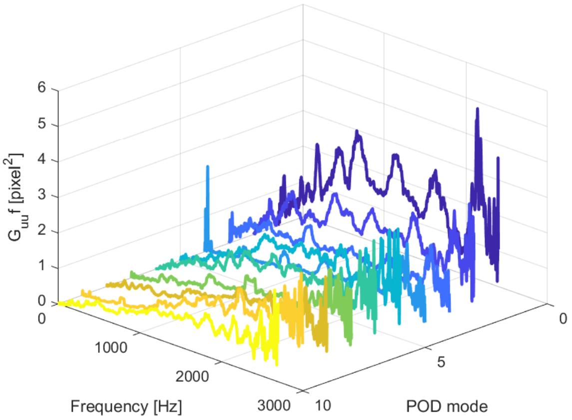

Figura 6.20: Premultiplied power spectra of the first 10 POD temporal coefficients FSS regime

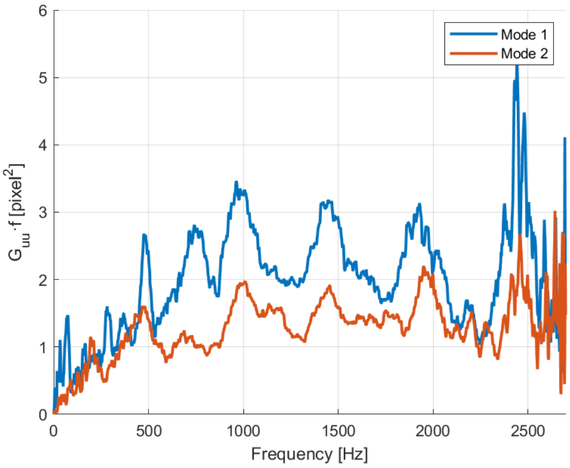

Figura 6.21: Premultiplied power spectra of the first 2 POD temporal coefficients for FSS regime

The premultiplied spectra of the first 10 POD temporal coefficients for Restricted Shock Separation case are reported in Figure 6.22. A view of the first two modes only is also provided in Figure 6.23. As with the FSS regime, the spectra exhibit a dominant peaks at approximately 480 Hz and also its harmonics, indicating that the same fundamental frequency content is present also after the transition. This observation suggests that, while the flow configuration has changed, the instability mechanism driving the unsteadiness has the same spectral content. The persistence of identical spectral peaks in both FSS and RSS, despite the orthogonality of the POD modes, indicates that the main difference lies not in the frequency itself, but in how the energy is spatially distributed. The system's unsteadiness originates from a single coherent instability of the shock–separation system but what changes through the transition is the mode of expression of that instability. The comparable amplitude of the spectral peaks between the two regimes also suggests that the energy of the instability has been redistributed: the global oscillation has lost its spatial coherence, and its energy becomes concentrated near the wall. This reflects the transformation from a global to a localized instability.

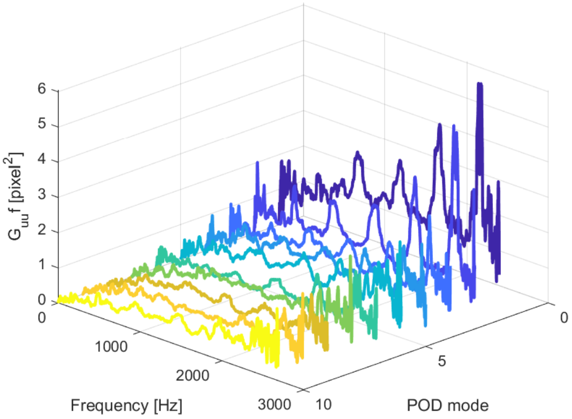

Figura 6.22: Premultiplied power spectra of the first 10 POD temporal coefficients for RSS regime

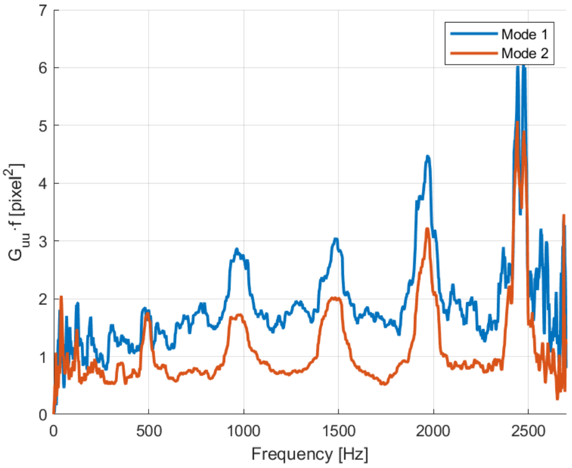

Figura 6.23: Premultiplied power spectra of the first 2 POD temporal coefficients for RSS regime

Finally, for both regimes, the spectral peaks at the lower and upper edges of the frequency domain are likely numerical artifacts related to the finite sampling window and the discrete Fourier transform, rather than true physical oscillations.

6.5 Asymmetries and transient regime

This section examines the evolution of the reconstructed mean horizontal dx and vertical dy displacement fields as the NPR is increased from 16 to 20, approaching the critical transition point to RSS, which previous studies defined happening at NPR$\approx$ 22 [29]. The analysis of these mean fields provides crucial insight into the reconfiguration of the shock structure and the progressive asymmetry that appears during the transition. As the NPR increases from 16 up to 20 the mean fields undergo significant changes, gradually obtaining characteristics previously identified only in the RSS regime. A key observation that one can make is that the flow dynamics on the upper and lower walls diverge: The structures on the upper side of the nozzle suggest that the flow is becoming attached or highly confined near the wall. On the contrary, the lower side of the jet continues to show characteristics of a separated, unattached flow, maintaining the initial FSS configuration. Literature [3] suggest that the mechanism driving the transition and subsequent is dictated by the axial position of the normal shock within the evolving shock system. When the normal shock is downstream of the separation point, the momentum balance is dominated by the flow passing the separation shock itself, leading to a global, free separation. As the NPR increases towards the transition threshold, the entire shock system moves upstream. When the normal shock moves upstream of the separation point, the flow passing the reflected shock from the triple point begins to dominate the momentum balance. This condition leads to the RSS regime.

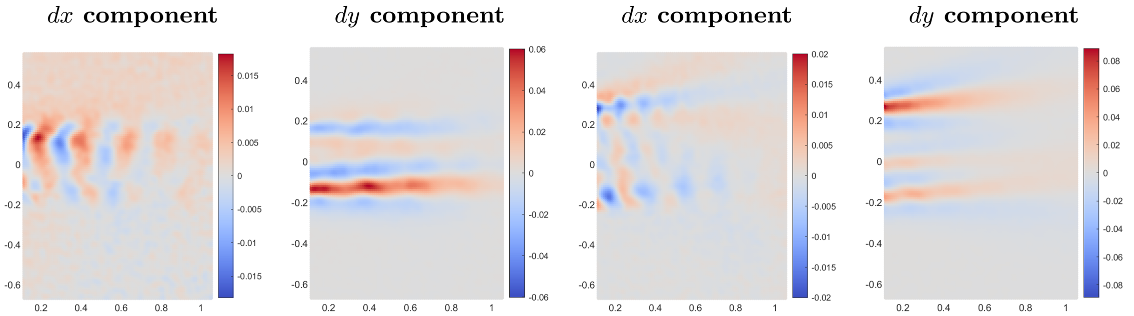

(a) FSS 16 NPR **(b)** FSS 16 NPR **(c)** FSS 18 NPR **(d)** FSS 18 NPR

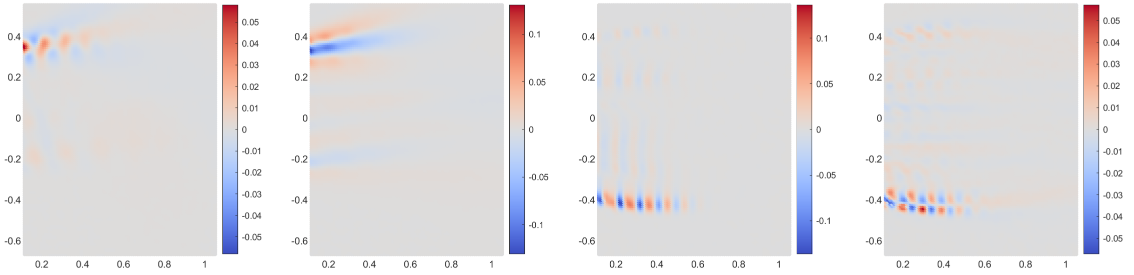

(e) FSS 20 NPR **(f)** FSS 20 NPR **(g)** RSS 24 NPR **(h)** RSS 24 NPR

Figura 6.24: Evolution of the first POD mode structure across different NPR conditions.

In Figure 6.24 we now examine the evolution of the first and most energetic POD mode across the different NPR's providing a qualitative evidence of the shift from FSS to RSS. Looking at the vertical component, as the NPR increases the structure begins to lose this vertical coherence. The energy, rather than being distributed across the jet's width, becomes more concentrated towards the shear layers. At 20 NPR, the dominant structure is highly compressed and localized near the upper part of the nozzle. The increase in magnitude also suggests that the vertical fluctuations of the shear layers are becoming more intense. The most clear evidence of the configuration transition can be seen in the *dx* component. As the NPR increases to 20 the pattern becomes highly localized and concentrated near the nozzle walls and the magnitude increases significantly becoming a major component of the flow unsteadiness.

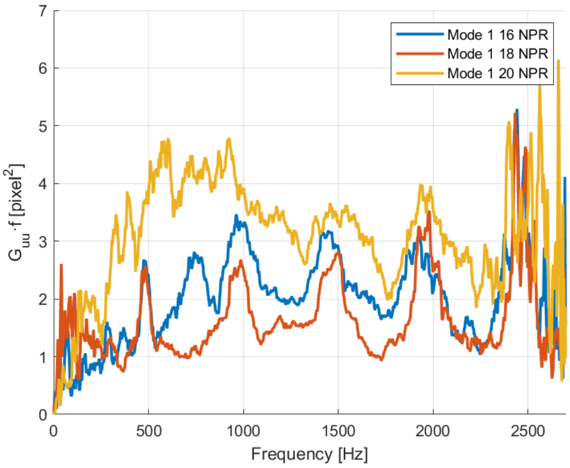

Figura 6.25: Comparison of the most energetic mode at different NPRs

The evolution of the flow dynamics during the approach to the FSS-RSS transition is further quantified by examining the frequency content of the time coefficients in figure 6.25. Moving from NPR 16 to NPR 20, there is a significant increase in the overall energy, which is represented by the area under the curve, particularly in the low-frequency band. At 16 NPR the main peak in frequency, thus most of the energy, is located in the fundamental frequency. As we move closer to the transition the highest peak moves to higher frequency. The increase in broadband energy directly indicates the intensification of the Shock Wave - Boundary Layer Interaction. As the NPR increases, the separation shock moves further downstream. This movement increase the amplitude of the inherent, stochastic motion back and forth of the shock, which feeds energy back into the larger turbulent structures, a mechanism well-documented in the context of turbulent SWBLI [1]. Also as the interaction becomes more severe, the physical movement of the separation shock becomes more impulsive. This may be linked to the measured peak shift to higher frequency.

The progressive flow asymmetry observed in the mean displacement fields exhibit the tendency for the flow to reattach on the upper wall while remaining separated on the lower side. Theoretical models for shock separation in nozzles with perfectly axisymmetric geometry suggest that the initial reattachment should occur at an arbitrary position [4] and tends to move within the nozzle until finally the flow reattaches around the complete perimeter. However, this persistent behavior suggests that the symmetry of the flow is consistently being broken by a non-ideal factor. This fixed asymmetry can be attributed to two primary factors: either a subtle but imperfection in the nozzle geometry or the presence of a persistent, external flow disturbance. Given the manufacturing method, the geometric imperfection is highly probable, potentially due to the inherent layer discontinuities or the build seam present in the 3D-printed nozzle body. In either case, the result is the consistent creation of an adverse pressure gradient along the upper wall that favors the observed asymmetric behavior. Further investigations are necessary to definitively identify the nature of this phenomenon. A straightforward yet effective method would be to rotate the nozzle 180° around its axis. If the reattachment remains on the upper side of the nozzle, the cause is external. In contrast, if it remains fixed relative to the nozzle body, it is evidence of a geometric imperfection.

Capitolo 7

Conclusions

The unsteady flow separation phenomena in over-expanded rocket nozzles pose a critical challenge to engine integrity due to the generation of severe side-loads. The purpose of this research was to experimentally investigate the flow unsteadiness in a Thrust Optimized Parabolic (TOP) contour nozzle across the Free Shock Separation (FSS) and Restricted Shock Separation (RSS) regimes, utilizing high-speed Background Oriented Schlieren (BOS) imaging combined with Proper Orthogonal Decomposition (POD)). The results presented in Chapter 6 provide a comprehensive experimental answer to the defined research objective and research questions in Chapter 1.

1. **Technique validation** – The high-speed BOS imaging was successfully applied for the experimental investigation of the supersonic nozzle exhaust plume. The technique offered an effective method for the visual characterization and topological mapping of unsteady flow fields dominated by strong density gradients.

2. **Modal analysis** – The POD analysis acted as a powerful spatial filter and spectral analysis tool, identifying and separating the most energetic coherent structures within the complex, turbulent flow field.

The aim is now to answer these questions:

- **RQ1**: How well is Background Oriented Schlieren (BOS) able to capture the relevant flow features of the nozzle?
    - What are the main strengths and limitations of BOS?

        The BOS technique was successfully implemented as a valid alternative to conventional Schlieren. Its operational performance is governed by a fundamental trade-off between flexibility and spatial resolution. The technique's main strength lies in:

  - · Simplicity and Cost Efficiency: BOS is structurally simpler and more accessible than a Toepler's system. It does not require high-quality, large-diameter optics nor a precise alignment with respect to the knife-edge cut-off. This translates directly to reduced cost and space requirements in the test section.
  - · Complete Topological Mapping: The ability to simultaneously acquire both the horizontal and vertical displacement fields eliminates the fundamental directional ambiguity of conventional Schlieren which only visualizes the gradient component perpendicular to the knife-edge.

  However, this strengths are counterbalanced by two key limitations:

  - · Spatial Resolution Loss (Geometric Blur): Since the camera must be focused on the background pattern rather than the flow itself, a geometric blur is unavoidable. This limitation the main experimental constraint. However, the issue was successfully addressed through optical optimization: the object-to-background distance Z_D was minimized $70mm \rightarrow 25mm$ and the aperture was reduced $f/8 \rightarrow f/16$.
  - · The accuracy and noise level of the reconstructed displacement field depend directly on the chosen cross-correlation algorithm and the specific window size used. However, the use of the BOSproc Tool allowed for a real-time parametric analysis of the correlation peak shape as a function of IW size, guaranteeing that the final parameter selection provided a clear and stable correlation peak while resolving the essential flow features.

- – To what extent do the reconstructed displacement fields (dx, dy) and density maps describe the nozzle flow topology?

  The reconstructed fields clearly captured the main flow features. The horizontal displacement field effectively visualized the streamwise pressure variations, showing alternating positive and negative regions that correspond to the sequence of compression and expansion waves inside the jet core. The vertical displacement field highlighted the upper and lower shear layers, where the strongest vertical density gradients are located. Finally, the derived density-related fields offered a complete picture of the flow topology, making a clear distinction between the pattern of the FSS regime and the more axial shock-cell structure that develops in RSS.

- – How does the simultaneous acquisition of dx and dy allow detecting wave orientation and flow structures?

While it is true that the vector formed by dx and dy could have provide a quantitative measure of the true, potentially three-dimensional wave orientation, the dual acquisition was used in this study to supply the necessary information for the reconstruction of the density field. In addition, the ability to separate the displacement allowed for a clear functional decomposition of the flow field: The streamwise compression and expansion wave sequences propagating along the jet axis become the distinctive traits of horizontal field, the shear layers location and behavior become the one for the the vertical field, defining the interface between the jet core and the ambient air. Furthermore, the observed shift in kinetic energy from the dy modes to the dx modes would have been entirely invisible to a single-component technique.

- **RQ2**: What are the dominant instability structures and mechanisms associated with FSS and RSS configurations?
  - What spectral features distinguish FSS and RSS regimes?

    The determination of distinct spectral features was not immediate. An initial spectral analysis performed directly on the HRBOS displacement fields was inconclusive. By inspecting single-point or small window-averaged regions, the analysis failed to reveal any distinct, low-frequency peaks. Consequently, the power spectra of the temporal coefficients obtained with POD were analyzed. The most significant result is the persistence of a fundamental frequency peak at approximately 480 Hz (and its integer harmonics) in the first few POD modes for both FSS and RSS. This demonstrates that the instability is driven by a common mechanism that is common before and after the transition.
  - Is it possible to describe the main unsteadiness with reduced-order reconstructions (low-rank approximation)?

    The analysis confirmed that the main unsteadiness is coherent and can be efficiently described by a low-rank approximation. The rapid decay of the POD eigenvalue spectrum demonstrated that the flow is mainly represented by the lowest-order modes. The first 200 modes collectively accounted for approximately 80% of the total energy.
  - To what extent can modal decomposition techniques connect the spectral content of the flow to its spatial topology?

    The modal decomposition techniques was also successfully used to establish a link between the spectral content and the spatial topology of the two regimes. The 480 Hz frequency can be defined as the common drive but while in FSS is primarily channeled into spatial modes that are energetically dominated by the vertical displacement component, during RSS this driver is redirected into the spatial modes that are energetically dominated by the axial displacement component.

Limitations and recommendations for future work

Building upon the successful validation of the methodology, the final conclusions must also address the unresolved mechanisms and translate them into future research agendas.

Limitations

The two main limitations of this study were:

- **Fixed flow asymmetry.** The most critical uncertainty in the flow physics concerns the fixed asymmetry observed at NPR values close to the transition, where the flow consistently reattached on the upper nozzle wall. This persistent behavior breaks the assumption of axisymmetry and introduces uncertainty in the general validity of the results. The cause of this asymmetry could not be conclusively determined within the present experimental setup, as it may arise from either a small geometric imperfection in the nozzle or an external facility-induced bias. Considering the nozzle was manufactured via 3D printing, it is highly probable that the geometric imperfection stems from the inherent layer discontinuities or the build seam, which act as fixed non-axisymmetric roughness elements on the wall.
- **Indirect frequency validation.** The POD analysis successfully isolated a fundamental frequency near 480 Hz, which appears to govern the dominant unsteadiness of the flow. However, the validation of this result remains indirect. A preliminary estimation of the corresponding Strouhal number was performed using jet core velocities derived from available CFD data and boundary-layer scaling from canonical flat-plate configurations. The resulting non-dimensional frequency fell within the range reported in the literature for similar SWBLI phenomena, suggesting physical consistency. Nevertheless, without direct velocity measurements, this validation cannot be considered rigorous.

Future recommendations

To address the above limitations and further advance the understanding of overexpanded nozzle dynamics, future research should consider:

- **Verification of flow asymmetry.** The next experimental campaign should include a nozzle rotation test of 180° around its axis. If the reattachment remains fixed on the upper wall (relative to the facility), the source of asymmetry is likely external; conversely, if it rotates with the nozzle, a geometric imperfection can be confirmed. Complementary flow visualization or surface pressure measurements along the wall could also help quantify the asymmetry and its influence on the transition process.

- **Velocity-field acquisition and Strouhal validation.** To strengthen the frequency analysis, future work should integrate Particle Image Velocimetry (PIV) or other velocity-resolved techniques alongside Schlieren imaging. This would enable direct calculation of the jet-core velocity and characteristic length scales, allowing the Strouhal number to be evaluated on a firmer physical basis. In addition, coupling velocity and density-gradient data would provide a richer, multi-field view of the flow unsteadiness.

- **Advanced modal decompositions.** Future analyses could benefit from applying advanced data-driven techniques such as Dynamic Mode Decomposition (DMD) and Spectral Proper Orthogonal Decomposition (SPOD) to the acquired displacement or velocity data. While POD efficiently identifies the most energetic flow structures, DMD provides a more explicit connection between spatial modes and their characteristic frequencies and growth rates, allowing a clearer interpretation of the dominant dynamical mechanisms. Similarly, SPOD offers a statistically consistent, frequency-resolved extension of POD, capable of separating coherent, frequency-specific structures from stochastic background fluctuations.

Appendice A

Appendix A: BOS uncertainty and limitation management

The analysis of unsteady flow requires rigorous characterization of noise and spatial bias introduced by the measurement technique. In this Appendix the steps taken to minimize the operational uncertainties and to address the inherent limitations of the line-of-sight technique are discussed.

A.1 Uncertainties mitigation

As detailed in Section 6.1, the minimization of BOS uncertainty began with the optimization of spatial resolution and the SNR. To make sure that the analyzed spectral content results only from the flow dynamics and not from external sources, a correction for was applied to every instantaneous displacement field. The correction involves removing the mean displacement of the entire optical system, calculated from a fixed Region of Interest (ROI) outside the flow domain, from every instantaneous displacement field. A fixed region of the background image was selected, the mean displacement vector within this region was calculated for each snapshot, the calculated vector was then subtracted from the entire displacement field of the corresponding frame.

The corrected pixel displacement vector, $\Delta\mathbf{r}'_k(x,y)$, for a given snapshot k at a point (x,y), is defined by the following equation:

$$\Delta\mathbf{r}'_k(x,y) = \Delta\mathbf{r}_k(x,y) - \overline{\Delta\mathbf{r}_k}_{\mathrm{ROI}} \tag{A.1}$$

where:

- $\Delta\mathbf{r}_k(x,y) = (\Delta x_k, \Delta y_k)$ is the original measured displacement vector for snapshot k.

- $\overline{\Delta \mathbf{r}_k}_{\text{ROI}}$ is the mean drift vector calculated within the pre-defined ROI (defined by coordinates $x_{\min}, x_{\max}, y_{\min}, y_{\max}$). This vector is computed by averaging the displacements within the ROI:

$$\overline{\Delta \mathbf{r}_k}_{\text{ROI}} = \left(\frac{1}{N_{\text{ROI}}} \sum_{(x,y)\in\text{ROI}} \Delta x_k(x,y), \frac{1}{N_{\text{ROI}}} \sum_{(x,y)\in\text{ROI}} \Delta y_k(x,y) \right)$$

- N_{ROI} is the number of valid measurement points within the ROI.

A.2 Inherent Methodological Limitations

A.2.1 Line-of-Sight Integration

As mentioned through out the study, the BOS technique is fundamentally a **line-of-sight** measurement. It does not measure the density field (ρ) directly, but rather the deflection angle (ϵ) of light rays integrated along the path of light. The primary output measured, the displacement field $\Delta\mathbf{r}(x, y)$, is directly proportional to this deflection angle and therefore the projected integral of the three-dimensional refractive index gradient field (∇n) along the depth of the measurement volume.

$$\Delta\mathbf{r}(x, y) \propto \int \epsilon(x, y, z)\, dz \propto \int \nabla_\perp n \, dz \tag{A.2}$$

Where $\nabla_\perp n$ represents the refractive index gradient components perpendicular to the light ray path. This integral nature establishes the systematic bias present on the primary measured quantity. This is something that has to be taken into account every time a discussion about the displacement or density fields is done throughout the entire document.

A.2.2 Density Field Reconstruction via Poisson Equation and $2D$ Assumption

In the Results chapter, the measured displacement fields are used to reconstruct two-dimensional $2D$ fields. This process is typically achieved by solving the **Poisson equation**:

$$\nabla^2 \rho_{\text{proj}} = \nabla \cdot (\Delta\mathbf{r}) \tag{A.3}$$

The output obtained from solving the Poisson equation, ρ_{proj} in Equation A.3, is the line-of-sight integrated density $\rho^*(x, y)$, and consequently carries units of mass per area [kg/m^2]. This integrated quantity must be converted back to the volumetric density $\rho(x, y)$ (in [kg/m^3]) for physical interpretation.

The general relationship between the measured integrated density $\rho^*(x, y)$ and the true three-dimensional volumetric density $\rho(x, y, z)$ is given by:

$$\rho^*(x, y) = \int_{\text{ray}} \rho(x, y, z) \, dz$$

A simplified approach to approximate the true density $\rho(x, y, z)$ is to assume the density field is constant along the line-of-sight (i.e., $\rho(x, y, z) \approx \rho(x, y)$) and then divide the integrated density by the effective thickness of the flow, L_{flow}: $\rho(x, y) \approx \rho^*(x, y)/L_{\text{flow}}$. This method, however, is mathematically valid only under the critical implicit assumption that the flow field is uniform or known along the line-of-sight ($\partial/\partial z \approx 0$)—i.e., that the $3D$ flow can be accurately approximated as $2D$. Without this strict assumption, the simple division by flow thickness leads to significant errors.

To achieve a true, rigorous quantitative insight into the density field,the effects of the depth (z-dependence) must be mathematically removed from the two-dimensional integrated measurement. Possible solutions that could eliminate this systematic error include:

1. Tomographic BOS: Using multiple cameras from different viewing angles to solve the full $3D$ refractive index field ($\nabla n(x, y, z)$).
2. Abel Inversion: The Abel-Poisson combination is a two-step hybrid inversion process for reconstructing an axisymmetric density field, $\rho(r, z)$, from its gravitational potential, $\Psi(z)$, measured along the symmetry axis.

Since these advanced techniques were beyond the scope of this work, the analysis focuses on a qualitative description of the flow and on the spectral evolution of the data.

Appendice B

Appendix B

The premultiplied PSD of the *dx* and *dy* fields, in the location of highest standard deviation (shear layers) from the mean flow, at 20 and 24 NPR are shown:

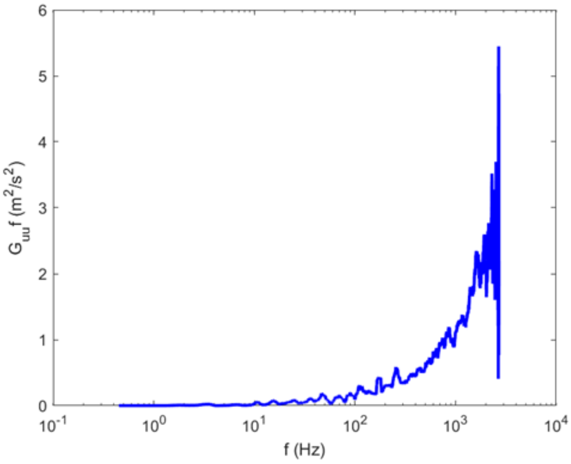

Figura B.1: Premultiplied PSD of the *dy* fields at 20 NPR

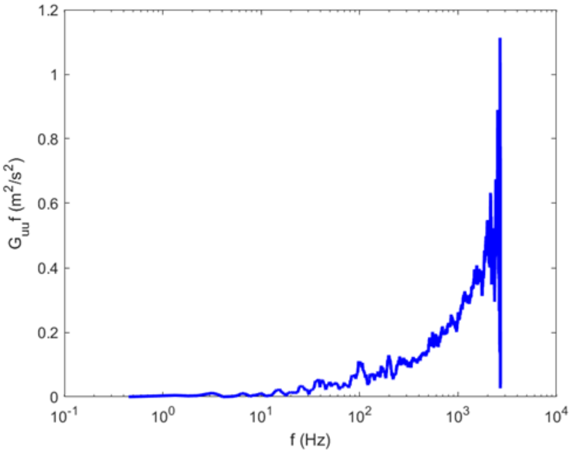

Figura B.2: Premultiplied PSD of the *dx* fields at 20 NPR

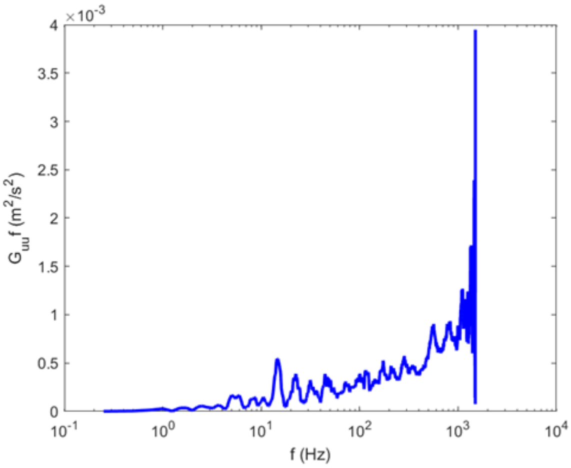

Figura B.3: Premultiplied PSD of the *dy* fields at 24 NPR

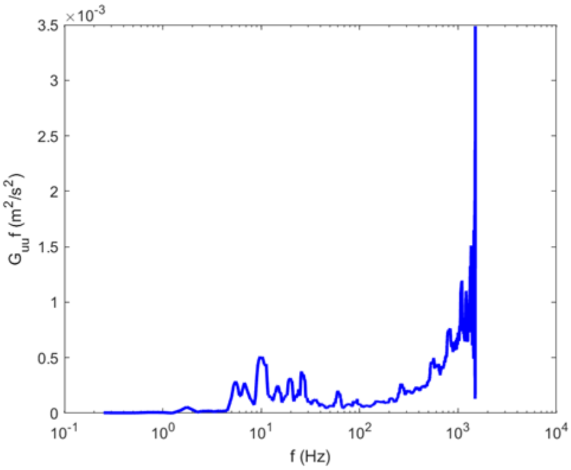

Figura B.4: Premultiplied PSD of the *dx* fields at 20 NPR

The reconstructed horizontal and vertical displacement fields for the 18 NPR case are shown in Figure B.5.

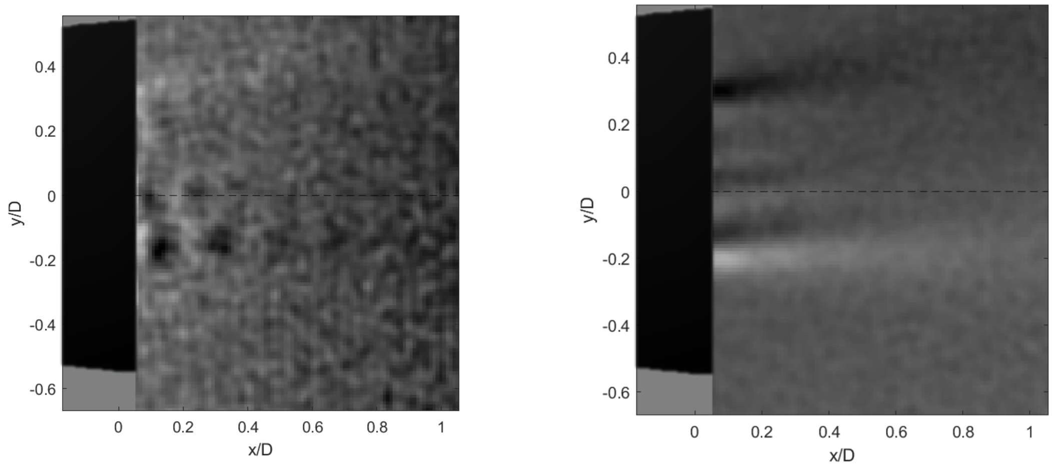

(a) Horizontal displacement field (dx)

(b) Vertical displacement field (dy)

Figura B.5: Reconstructed horizontal and vertical displacement for FSS at 18 NPR.

The reconstructed flow density structures for the 18 NPR case are shown in Figure B.6.

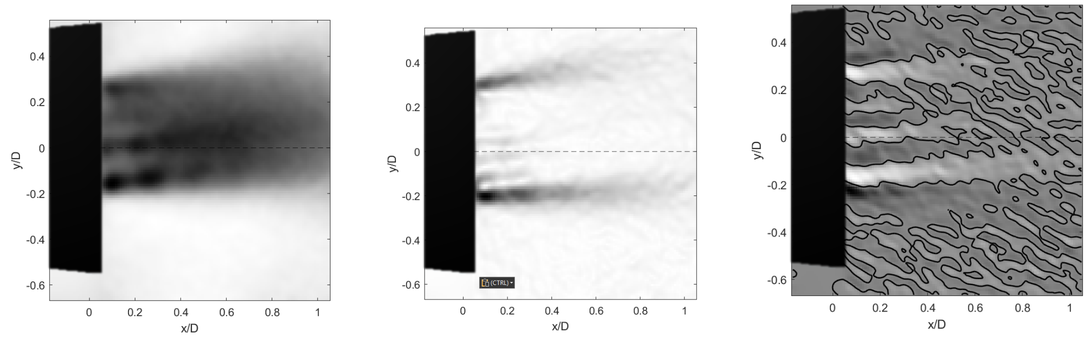

(a) Reconstructed projected density field

(b) Magnitude of the density gradient

(c) Laplacian of the density gradient

Figura B.6: Reconstructed flow density structures for the FSS 18 NPR

The reconstructed horizontal and vertical displacement fields for the 20 NPR case are shown in Figure B.7.

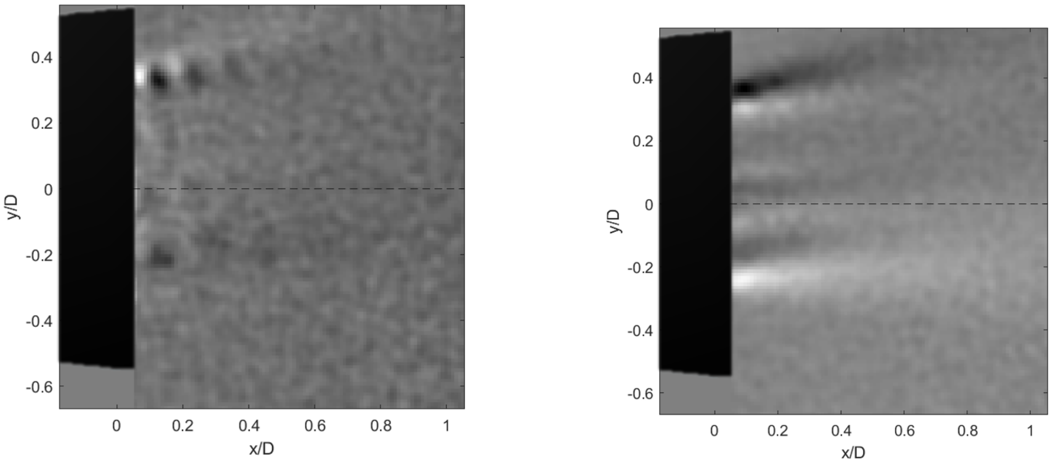

(a) Horizontal displacement field (dx)

(b) Vertical displacement field (dy)

Figura B.7: Reconstructed horizontal and vertical displacement for FSS at 20 NPR.

The reconstructed flow density structures for the 20 NPR case are shown in Figure B.8.

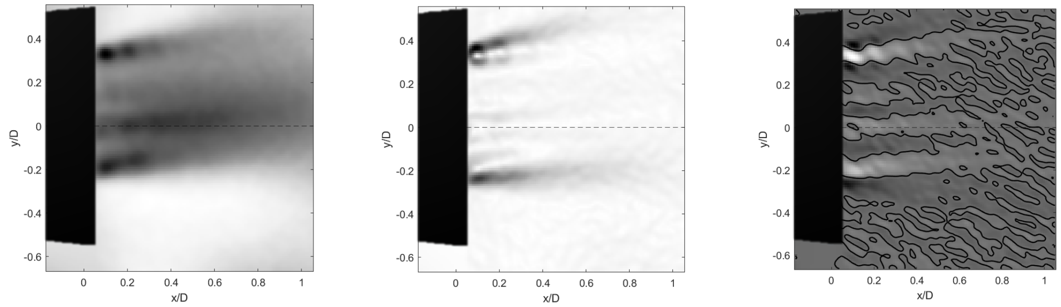

(a) Reconstructed projected density field

(b) Magnitude of the density gradient

(c) Laplacian of the density gradient

Figura B.8: Reconstructed flow density structures for the FSS 20 NPR

Bibliografia

[1] S. B. Verma. «Shock unsteadiness in a thrust optimized parabolic nozzle». en. In: *Shock Waves* 19.3 (lug. 2009), pp. 193–212. ISSN: 0938-1287, 1432-2153. DOI: `10.1007/s00193-008-0180-8`. URL: `https://link.springer.com/10.1007/s00193-008-0180-8` (visitato il giorno 07/11/2025) (cit. alle pp. 2, 17, 48, 52, 56, 63).

[2] Manuel Frey e Gerald Hagemann. «Restricted Shock Separation in Rocket Nozzles». en. In: *Journal of Propulsion and Power* 16.3 (mag. 2000), pp. 478–484. ISSN: 0748-4658, 1533-3876. DOI: `10.2514/2.5593`. URL: `https://arc.aiaa.org/doi/10.2514/2.5593` (visitato il giorno 07/11/2025) (cit. alle pp. 2, 10, 13).

[3] G. Hagemann, M. Frey e W. Koschel. «Appearance of Restricted Shock Separation in Rocket Nozzles». en. In: *Journal of Propulsion and Power* 18.3 (mag. 2002), pp. 577–584. ISSN: 0748-4658, 1533-3876. DOI: `10.2514/2.5971`. URL: `https://arc.aiaa.org/doi/10.2514/2.5971` (visitato il giorno 07/11/2025) (cit. alle pp. 2, 62).

[4] Jan Östlund. «FLOW PROCESSES IN ROCKET ENGINE NOZZLES WITH FOCUS ON FLOW SEPARATION ANDSIDE-LOADS». en. Licentiate Thesis. Royal Institute of Technology, 2002 (cit. alle pp. 2, 6–9, 14, 20, 21, 63).

[5] Anh Thi Nguyen, H. Deniau, S. Girard e T. Alziary De Roquefort. «Unsteadiness of Flow Separation and End-Effects Regime in a Thrust-Optimized Contour Rocket Nozzle». en. In: *Flow, Turbulence and Combustion* 71.1-4 (mar. 2003), pp. 161–181. ISSN: 1386-6184, 1573-1987. DOI: `10.1023/B:APPL.0000014927.61427.ad`. URL: `https://link.springer.com/10.1023/B:APPL.0000014927.61427.ad` (visitato il giorno 07/11/2025) (cit. alle pp. 2, 16).

[6] Sébastien Deck e Anh Thi Nguyen. «Unsteady Side Loads in a Thrust-Optimized Contour Nozzle at Hysteresis Regime». en. In: *AIAA Journal* 42.9 (set. 2004), pp. 1878–1888. ISSN: 0001-1452, 1533-385X. DOI: `10.2514/1.2425`. URL: `https://arc.aiaa.org/doi/10.2514/1.2425` (visitato il giorno 07/11/2025) (cit. alle pp. 2, 16).

[7] R. Benay, B. Chanetz, B. Mangin, L. Vandomme e J. Perraud. «Shock Wave/Transitional Boundary-Layer Interactions in Hypersonic Flow». en. In: *AIAA Journal* 44.6 (giu. 2006), pp. 1243–1254. ISSN: 0001-1452, 1533-385X. DOI: `10.2514/1.10512`. URL: `https://arc.aiaa.org/doi/10.2514/1.10512` (visitato il giorno 07/11/2025) (cit. a p. 2).

[8] Yi Yang, Qiancheng Wang, Yuxin Zhao, Gang He e Yilong Zhao. «Unsteady shock wave behaviors in supersonic nozzle exit under varying over-expanded conditions». en. In: *Physics of Fluids* 37.8 (ago. 2025), p. 086160. ISSN: 1070-6631, 1089-7666. DOI: `10.1063/5.0283192`. URL: `https://pubs.aip.org/pof/article/37/8/086160/3359946/Unsteady-shock-wave-behaviors-in-supersonic-nozzle` (visitato il giorno 07/11/2025) (cit. alle pp. 2, 37, 38).

[9] Anindya Chatterjee. «An introduction to the proper orthogonal decomposition». en. In: () (cit. alle pp. 2, 37, 50).

[10] Oliver T. Schmidt e Tim Colonius. «Guide to Spectral Proper Orthogonal Decomposition». en. In: *AIAA Journal* 58.3 (mar. 2020), pp. 1023–1033. ISSN: 0001-1452, 1533-385X. DOI: `10.2514/1.J058809`. URL: `https://arc.aiaa.org/doi/10.2514/1.J058809` (visitato il giorno 07/11/2025) (cit. alle pp. 2, 38).

[11] Markus Raffel. «Background-oriented schlieren (BOS) techniques». en. In: *Experiments in Fluids* 56.3 (mar. 2015), p. 60. ISSN: 0723-4864, 1432-1114. DOI: `10.1007/s00348-015-1927-5`. URL: `http://link.springer.com/10.1007/s00348-015-1927-5` (visitato il giorno 07/11/2025) (cit. alle pp. 3, 39).

[12] Joachim A Bron, Woutijn J Baars e Ferdinand F J Schrijer. «Density Field Reconstruction of an Overexpanded Supersonic Jet using Tomographic Background-Oriented Schlieren». en. In: () (cit. alle pp. 3, 46).

[13] João Cristovão Silva e Francisco Brójo. *A Review on Supersonic Nozzle Design and Analysis with Traditional Methods.* 20 Mar. 2025. DOI: `10.20944/preprints202503.1464.v1`. URL: `https://www.preprints.org/manuscript/202503.1464/v1` (visitato il giorno 11/11/2025) (cit. a p. 5).

[14] G. V. R. RAO. «Exhaust Nozzle Contour for Optimum Thrust». In: *Journal of Jet Propulsion* 28.6 (giu. 1958), pp. 377–382. ISSN: 1936-9980. DOI: `10.2514/8.7324`. URL: `http://dx.doi.org/10.2514/8.7324` (cit. a p. 7).

[15] Akhtar Khan e Sanjay Kumar Sardiwal. «Design of a Supersonic Nozzle using Method of Characteristics». In: *International Journal of Engineering Research* 2.11 (2013) (cit. a p. 8).

[16] Afaque Shams e Pierre Comte. «FORMATION OF CAP-SHOCK PATTERN». In: () (cit. a p. 8).

[17] Jr. John D. Anderson. *Fundamentals of Aerodynamics*. 6th. (cit. a p. XX). New York: McGraw-Hill Education, 2017. ISBN: 978-1-259-12991-9 (cit. alle pp. 9, 11, 13).

[18] Tamara Smith. «Boundary layer development as a function of chamber pressure in the NASA Lewis 1030:1 area ratio rocket nozzle». In: *24th Joint Propulsion Conference*. 24th Joint Propulsion Conference. Boston,MA,U.S.A.: American Institute of Aeronautics e Astronautics, 11 lug. 1988. DOI: `10.2514/6.1988-3301`. URL: `https://arc.aiaa.org/doi/10.2514/6.1988-3301` (visitato il giorno 11/11/2025) (cit. a p. 12).

[19] A. Shams, G. Lehnasch, P. Comte, H. Deniau e T. Alziary de Roquefort. «Unsteadiness in shock-induced separated flow with subsequent reattachment of supersonic annular jet». In: *Computers and Fluids* 78 (apr. 2013), pp. 63–74. ISSN: 0045-7930. DOI: `10.1016/j.compfluid.2012.11.016`. URL: `http://dx.doi.org/10.1016/j.compfluid.2012.11.016` (cit. a p. 14).

[20] Shashi B. Verma e O. Haidn. «Surface flow studies of restricted shock separation in a thrust optimized parabolic nozzle». en. In: *Shock Waves* 19.5 (ott. 2009), pp. 371–376. ISSN: 0938-1287, 1432-2153. DOI: `10.1007/s00193-009-0211-0`. URL: `http://link.springer.com/10.1007/s00193-009-0211-0` (visitato il giorno 07/11/2025) (cit. a p. 15).

[21] W. J. Baars e C. E. Tinney. «Transient wall pressures in an overexpanded and large area ratio nozzle». en. In: *Experiments in Fluids* 54.2 (feb. 2013), p. 1468. ISSN: 0723-4864, 1432-1114. DOI: `10.1007/s00348-013-1468-8`. URL: `http://link.springer.com/10.1007/s00348-013-1468-8` (visitato il giorno 07/11/2025) (cit. a p. 16).

[22] S. B. Verma e O. Haidn. «Study of Restricted Shock Separation Phenomena in a Thrust Optimized Parabolic Nozzle». en. In: *Journal of Propulsion and Power* 25.5 (set. 2009), pp. 1046–1057. ISSN: 0748-4658, 1533-3876. DOI: `10.2514/1.42351`. URL: `https://arc.aiaa.org/doi/10.2514/1.42351` (visitato il giorno 07/11/2025) (cit. alle pp. 16, 48).

[23] Shashi Verma e Oskar Haidn. «Goertler Vortex Formation During Shut Down Sequence Inside a Thrust Optimized Parabolic (TOP) Rocket Nozzle». en. In: *43rd AIAA Aerospace Sciences Meeting and Exhibit*. Reno, Nevada: American Institute of Aeronautics e Astronautics, gen. 2005. ISBN: 978-1-62410-064-2. DOI: `10.2514/6.2005-518`. URL: `https://arc.aiaa.org/doi/10.2514/6.2005-518` (visitato il giorno 07/11/2025) (cit. a p. 16).

[24] E. Martelli, P. P. Ciottoli, L. Saccoccio, F. Nasuti, M. Valorani e M. Bernardini. «Characterization of Unsteadiness in an Overexpanded Planar Nozzle». en. In: *AIAA Journal* 57.1 (gen. 2019), pp. 239–251. ISSN: 0001-1452, 1533-385X. DOI: `10.2514/1.`

`J057162`. URL: `https://arc.aiaa.org/doi/10.2514/1.J057162` (visitato il giorno 07/11/2025) (cit. a p. 17).

[25] Weibo Hu, Stefan Hickel e Bas W. Van Oudheusden. «Low-frequency unsteadiness mechanisms in shock wave/turbulent boundary layer interactions over a backward-facing step». en. In: *Journal of Fluid Mechanics* 915 (mag. 2021), A107. ISSN: 0022-1120, 1469-7645. DOI: `10.1017/jfm.2021.95`. URL: `https://www.cambridge.org/core/product/identifier/S0022112021000951/type/journal_article` (visitato il giorno 07/11/2025) (cit. a p. 17).

[26] D.S. Dolling. «Fluctuating Loads in Shock Wave/Turbulent Boundary Layer Interaction: Tutorial and Update». In: *31st Aerospace Sciences Meeting*. 31st Aerospace Sciences Meeting. Reno,NV,U.S.A.: American Institute of Aeronautics e Astronautics, 11 gen. 1993. DOI: `10.2514/6.1993-284`. URL: `https://arc.aiaa.org/doi/10.2514/6.1993-284` (visitato il giorno 11/11/2025) (cit. a p. 17).

[27] E. Martelli, L. Saccoccio, P. P. Ciottoli, C. E. Tinney, W. J. Baars e M. Bernardini. «Flow dynamics and wall-pressure signatures in a high-Reynolds-number overexpanded nozzle with free shock separation». In: *Journal of Fluid Mechanics* 895 (mag. 2020). ISSN: 1469-7645. DOI: `10.1017/jfm.2020.280`. URL: `http://dx.doi.org/10.1017/jfm.2020.280` (cit. alle pp. 17, 45).

[28] Bryan E. Schmidt, Brett F. Bathel, Samuel J. Grauer, Michael J. Hargather, James T. Heineck e Markus Raffel. «Twenty-Five Years of Background-Oriented Schlieren: Advances and Novel Applications». en. In: *AIAA SCITECH 2025 Forum*. Orlando, FL: American Institute of Aeronautics e Astronautics, gen. 2025. ISBN: 978-1-62410-723-8. DOI: `10.2514/6.2025-1627`. URL: `https://arc.aiaa.org/doi/10.2514/6.2025-1627` (visitato il giorno 07/11/2025) (cit. alle pp. 18, 19, 39).

[29] Gloria Nallo. «Experimental assessment of nozzle flow unsteadiness through optical techniques». en. Licentiate Thesis. Politecnico di Torino, 2024 (cit. alle pp. 24, 28, 61).

[30] Krijn de Kievit. «Development of a Rocket Nozzle Test Facility for Measurements of Fluid-Structure Interaction Phe- nomena». en. Licentiate Thesis (cit. a p. 26).

[31] G. S. Settles. *Schlieren and Shadowgraph Techniques*. en. Berlin, Heidelberg: Springer Berlin Heidelberg, 2001. ISBN: 978-3-642-63034-7 978-3-642-56640-0. DOI: `10.1007/978-3-642-56640-0`. URL: `http://link.springer.com/10.1007/978-3-642-56640-0` (visitato il giorno 07/11/2025) (cit. a p. 39).

[32] Julia Dobrosotskaya, Abdulaziz Alrefaie e Bryan E. Schmidt. «A Quantitative Comparison of Background Oriented and Conventional Schlieren Visualization». en. In: *AIAA SCITECH 2023 Forum*. National Harbor, MD & Online: American

Institute of Aeronautics e Astronautics, gen. 2023. ISBN: 978-1-62410-699-6. DOI: 10.2514/6.2023-2439. URL: https://arc.aiaa.org/doi/10.2514/6.2023-2439 (visitato il giorno 07/11/2025) (cit. a p. 40).

[33] Clemens Schwarz e Johannes N. Braukmann. «Practical aspects of designing background-oriented schlieren (BOS) experiments for vortex measurements». en. In: *Experiments in Fluids* 64.4 (apr. 2023), p. 67. ISSN: 0723-4864, 1432-1114. DOI: 10.1007/s00348-023-03602-1. URL: https://link.springer.com/10.1007/s00348-023-03602-1 (visitato il giorno 07/11/2025) (cit. a p. 41).

[34] Shashi Bhushan Verma, Ralf Stark e Oskar Haidn. «Relation between shock unsteadiness and the origin of side-loads inside a thrust optimized parabolic rocket nozzle». In: *Aerospace Science and Technology* 10.6 (set. 2006), pp. 474–483. ISSN: 1270-9638. DOI: 10.1016/j.ast.2006.06.004. URL: http://dx.doi.org/10.1016/j.ast.2006.06.004 (cit. a p. 52).

[35] G. Hagemann, M. Frey, W. Koschel, M. Terhardt e D. Haeseler. «Status of Flow Separation Prediction in Rocket Nozzles». In: *34th AIAA/ASME/SAE/ASEE Joint Propulsion Conference and Exhibit.* AIAA 98-3619. (cit. a p. XX). Cleveland, OH, USA: American Institute of Aeronautics e Astronautics, 1998. DOI: 10.2514/6.1998-3619.

[36] S.B. Verma e O. Haidn. «Unsteady shock motions in an over-expanded parabolic rocket nozzle». en. In: *Aerospace Science and Technology* 39 (dic. 2014), pp. 48–71. ISSN: 12709638. DOI: 10.1016/j.ast.2014.08.003. URL: https://linkinghub.elsevier.com/retrieve/pii/S1270963814001539 (visitato il giorno 07/11/2025).

[37] Wiehan Kwan e Ralf Stark. «Flow Separation Phenomena in Subscale Rocket Nozzles». en. In: *38th AIAA/ASME/SAE/ASEE Joint Propulsion Conference & Exhibit.* Indianapolis, Indiana: American Institute of Aeronautics e Astronautics, lug. 2002. ISBN: 978-1-62410-115-1. DOI: 10.2514/6.2002-4229. URL: http://arc.aiaa.org/doi/abs/10.2514/6.2002-4229 (visitato il giorno 07/11/2025).

[38] Shashi Verma e H.K. Ciezki. «Unsteady Nature of Flow Separation Inside a Thrust Optimised Parabolic Nozzle». en. In: *41st Aerospace Sciences Meeting and Exhibit.* Reno, Nevada: American Institute of Aeronautics e Astronautics, gen. 2003. ISBN: 978-1-62410-099-4. DOI: 10.2514/6.2003-1139. URL: https://arc.aiaa.org/doi/10.2514/6.2003-1139 (visitato il giorno 07/11/2025).

[39] Bo Sun e Zhuo Chang-Fei. «A Review on Asymmetry Characteristics of Confined Shock Wave/Boundary Layer Interactions». en. In: 23.2 (giu. 2020). DOI: 10.6180/jase.202006_23(2).0010.

[40] S. B. Verma e C. Manisankar. «Origin of flow asymmetry in planar nozzles with separation». en. In: *Shock Waves* 24.2 (mar. 2014), pp. 191–209. ISSN: 0938-1287, 1432-2153. DOI: `10.1007/s00193-013-0492-1`. URL: `http://link.springer.com/10.1007/s00193-013-0492-1` (visitato il giorno 07/11/2025).

[41] L. Venkatakrishnan. «Density Measurements in an Axisymmetric Underexpanded Jet by Background-Oriented Schlieren Technique». en. In: *AIAA Journal* 43.7 (lug. 2005), pp. 1574–1579. ISSN: 0001-1452, 1533-385X. DOI: `10.2514/1.12647`. URL: `https://arc.aiaa.org/doi/10.2514/1.12647` (visitato il giorno 07/11/2025).